Swirl-Stabilised Hydrogen Combustor with Axial Air Injection

Numerical Simulations and Cold Flow Experiments

S.P. Vermeijlen

Master of Science - Thesis
Delft University of Technology
Faculty of Aerospace Engineering

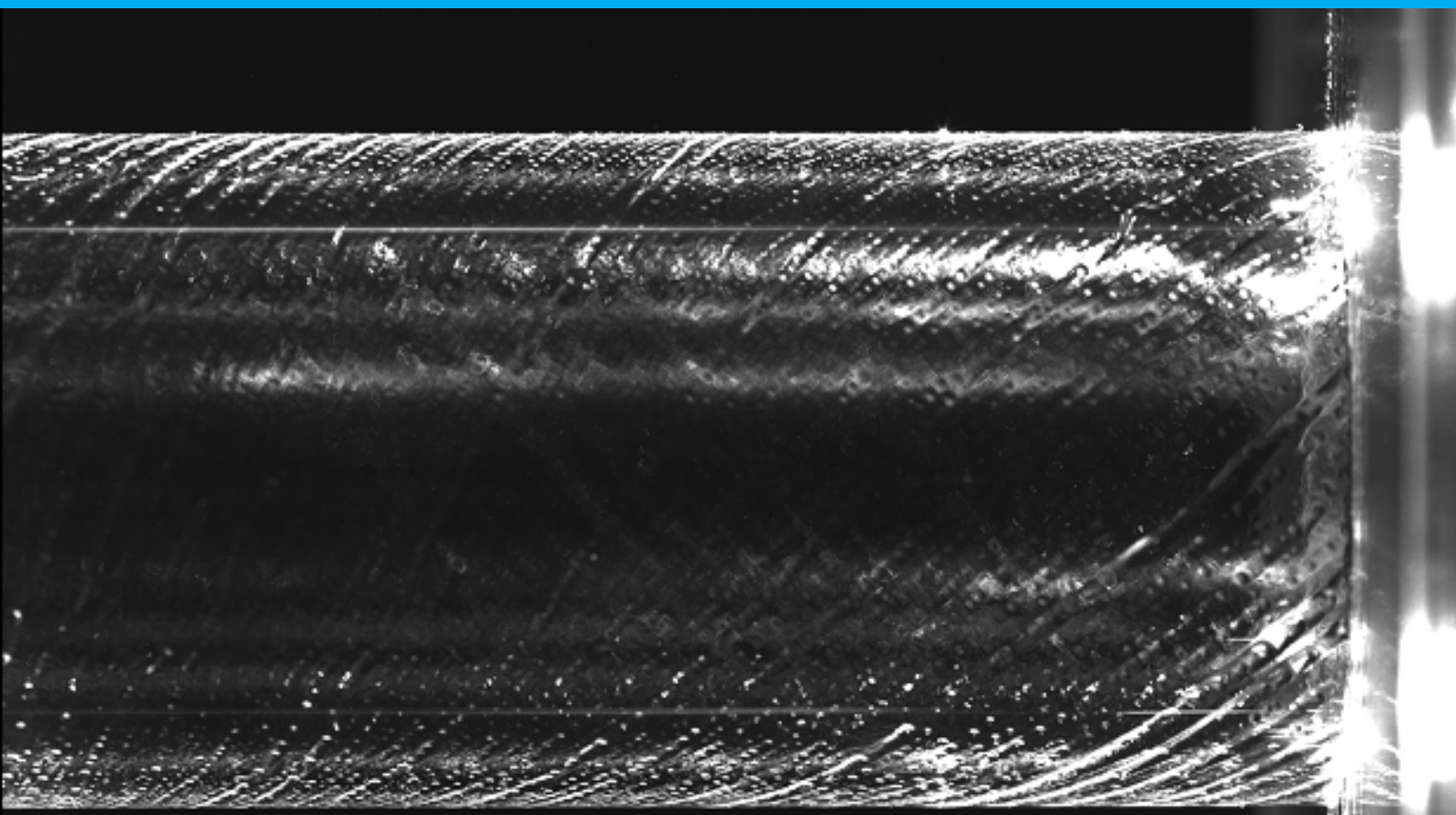

TU Delft

Swirl-Stabilised Hydrogen Combustor with Axial Air Injection

Numerical Simulations and Cold Flow Experiments

by

S.P. Vermeijlen

to obtain the degree of Master of Science
at the Delft University of Technology,
to be defended publicly on Friday July 2, 2021 at 13:00.

Student number:	4344707	
Project duration:	February 2, 2020 – July 2, 2021	
Thesis committee:	Dr. A. Gangoli Rao,	TU Delft, supervisor
	Prof.dr.ing. G. Eitelberg	TU Delft, chairman
	Dr.ir. F.F.J. Schrijer,	TU Delft

TU Delft

Preface

With this Master's thesis report my time as a student at the TU Delft is coming to an end. I thoroughly enjoyed the good times I have had here during lectures and outside of them. The thesis was a unique opportunity to apply the knowledge I have gathered over the academic years as well as to learn so much more.

Over the years I have learnt how much I like hands-on engineering. I am thus very grateful to have been able to do experimental work with high-tech equipment for my thesis. Definitely during a pandemic, it is an absolute delight to get out of the house to work in a laboratory. I feel privileged to have had this opportunity and to have worked with so many fun people along the way.

I would like to express my gratitude to all who have helped me during my thesis. Obviously, a huge shout-out to Dr. Arvind Gangoli Rao, who supervised my thesis. Thank you again for giving me the opportunity to work on this inspiring project! Your positive attitude made it a pleasure to work on this thesis. I also wish to thank Rishikesh Sampat and Kaushal Dave for your assistance with setting up and conducting the experiments as well as your advice and support whenever I needed it. I could not have done it without you. It had an absolutely great time with you, working the long hours in the lab. All staff members at the High Speed Lab are also massively appreciated for their assistance with acquiring and producing the components required for this thesis.

Furthermore, I wish to thank my girlfriend and all of my friends for always being there for me and for the wonderful times we've had so far. Without you studying would have been a drag. Thank you for the days and nights full of laughter and celebration! Finally, I massively appreciate my parents for providing me with the opportunity to have studied here in Delft. Your support throughout my entire life cannot be exaggerated. Thank you for everything!

S. P. Vermeijlen
Delft, June 2021

Contents

List of Figures

List of Tables

Nomenclature

Acronyms

AAI	Axial air injection
ACARE	Advisory Council for Aviation Research and innovation in Europe
AHEAD	Advanced Hybrid Engines for Aircraft Development
AR	Aspect ratio
CFD	Computational Fluid Dynamics
CIVB	Combustion Induced Vortex Breakdown
DOF	Depth of focus
GGI	General Grid Interface
ICAO	International Civil Aviation Organization
IW	Interrogation window
LSV	Laser Speckle Velocimetry
MT	Mixing tube
NOx	Nitrogen Oxides
PIV	Particle Image Velocimetry
PLIF	Planar Laser-Induced Fluorescence
PTU	Programmable Timing Unit
PTV	Particle Tracking Velocimetry
PVC	Precessing vortex core
RANS	Reynolds Averaged Navier Stokes
RMS	Root mean square
sst	Shear stress transport
TE	Trailing edge
UHC	Unburned hydrocarbons
VB	Vortex breakdown

Greek Symbols

α	Radial swirler vane inlet angle	rad
ϵ	Turbulence dissipation rate	$J/(kgs)$
λ	Light wavelength	m
μ	Dynamic viscosity	Ns/m^2
Ω	Angular velocity	rad/s
ω	Specific turbulence dissipation rate	$1/s$
ϕ	(Effective) equivalence ratio	–
ϕ	Axial swirler vane angle	rad
Ψ	Axial air injection volume flow fraction	–
ψ	Blockage factor	–
ρ	Density	kg/m^3
σ	dimensionless geometric parameter of swirler	–
σ^2	Variance	–
θ	Polar angle	rad
ξ	Angle of adjustment of movable block swirler	rad
ξ_m	Maximum angle of adjustment of movable block swirler	rad

Roman Symbols

$\dot{m}$	Mass flow rate	kg/s
$\dot{V}$	Volume flow rate	$nlpm$
$\overline{C^*(i)}$	Temporally averaged concentration	$1/m^3$
A	Cross sectional area	m^2
A_{fp}	Fuel port cross sectional area	m^2

AFR_{stoich}	Stoichiometric air-to-fuel ratio	–
$C^*(i,t)$	Measured concentration	$1/m^3$
C^*_∞	Homogenized Concentration	$1/m^3$
D	Diameter	m
d_τ	Apparent particle size on sensor	m
d_{diff}	Diffraction size	m
d_{geom}	Actual particle size on sensor	m
d_{im}	Image diameter	m
d_{obj}	Object diameter	m
dt	Laser pulse interval	s
f	Focal length	mm
$f_\#$	F-stop	–
G_θ	Axial flux of angular momentum	Nm
G_x	Axial flux of axial momentum (Axial thrust)	N
J	Momentum flux ratio	–
k	Turbulence kinetic Energy	J/kg
L	Angular Momentum	$kg\,m^2/s$
L_{slot}	Slot length	m
M	Magnification	–
M_w	Molar weight	g/mol
n	Number of vanes	–
N_i	Number of pixels	–
N_t	Number of timestamps	–
N_{pix}	Number of pixels	–
p	Static pressure	Pa
R	Radius	m
r_0	Vortex core radius	m
R_h	Axial swirler hub radius	m
R_n	Axial swirler tube radius	m
r_p	Particle radius	m
Re	Reynolds number	–
Res	Resolution	pix/mm
s	Optic spacing	mm
SE	Standard Error	–
Sw	Swirl number	–
t	Vane thickness	m
U	Axial velocity	m/s
U_t	Temporal unmixedness	–
U_x	Spatial unmixedness	–
v	Velocity	m/s
v_f	Fluid velocity	m/s
v_p	Particle velocity	m/s
v_r	Radial velocity	m/s
v_x	Velocity in x-direction	m/s
v_y	Velocity in y-direction	m/s
v_{ax}	Axial velocity	m/s
v_{tan}	Tangential velocity	m/s
W	Tangential velocity	m/s
x	x-position (axial)	m
y	y-position	m

1

Introduction

As emission regulations on civil aviation rapidly become stricter new forms of propulsion will have to arise. As a consequence, research into lower-emission alternatives to currently employed aircraft engines is growing. A particularly interesting trend is the research into lean premixed hydrogen combustion in gas turbines. Such a combustor consists of a swirl generator and fuel injection upstream of a mixing tube. As the name suggest, this is where the injected fuel and air mix to form a near homogeneous mixture. Downstream of the mixing tube is a larger-diameter combustion chamber, where the mixture ignites to ultimately generate power. Due to the high mixing quality achieved with these combustors their potential for producing low NOx emissions is great, but they have a major drawback. Their operating conditions make them prone to flame flashback, especially when a fast burning gas like hydrogen is used as fuel. This is a consequence of the relatively low axial velocity on the centre-line of the mixing tube. A low axial velocity here provides limited resistance for a flame to travel upstream into the mixing tube. This should be avoided at all times as this has a negative impact on the combustion stability and could even damage the engine. Therefore the concept of axial air injection was recently introduced. In this concept a non-swirling jet of air is injected on the centre-line of the mixing tube. From first results, the solution appears promising in its ability to reduce the flashback propensity.

The purpose of this thesis is to further investigate the concept of axial air injection in a lean-premixed gas turbine combustor. More specifically the research objective is formulated as follows:

"**To determine the effects of axial air injection and swirl intensity on the flashback resistance of a lean-premixed swirl-stabilised hydrogen combustor for axial- and radial swirl generators by conducting Computational Fluid Dynamics and Particle Image Velocimetry.**"

Before this objective was formulated, a literature study was performed into the relevant topics related to the subject. The results of this literature study and the full research definition are presented in chapter 2. Next, the design methodology of the experimental model (and CFD domain) are presented in chapter 3. This is followed by the presentation of the adopted methodology for the CFD campaign in chapter 4. The setup for the PIV experiments and related processes are then discussed in chapter 5. Subsequently, the results from both the numerical simulations and experiments are presented and analysed in chapter 6. Finally, conclusions are drawn and recommendations for future research are made in chapter 7 and chapter 8 respectively.

2

Theoretical Background

This chapter will provide relevant background information regarding the literature review. More specifically, aircraft emissions and regulations, the AHEAD project, and NOx formation are discussed. A review of the literature on the topics of hydrogen combustors, swirl-stabilised combustion, mixing quality, particle image velocimetry, and flashback is presented in this chapter. Recent studies that combine these topics are discussed at the end of the chapter.

2.1. Aircraft Emissions

Over the last decades the demand for civil aviation has steadily increased. Between 1995 and 2015 the amount of passenger kilometres flown with civil aircraft has nearly tripled, averaging a compound annual growth rate of 5.4%. The International Civil Aviation Organization (ICAO) has forecasted this annual growth to stay above 4% up to 2045 [41]. Unfortunately, this increase in aviation demand also contributes to climate change. Currently about 2% of the global carbon dioxide (CO2) emissions are caused by the aviation sector [26]. However CO2 is not the only emission responsible for anthropogenic climate change. Modern aircraft engines also produce water vapor (H2O), nitrogen oxides (NOx), unburned hydrocarbons (UHC), carbon monoxide (CO) and other substances that directly or indirectly contribute to anthropogenic global warming. It is estimated that the total contribution of air traffic to man-made climate change is about 5% [64].

This figure is forecasted to remain at 5% or increase up to 15% by 2050 dependent on the scenario [3] & [57]. To avoid this worst case scenario technological advancements will have to be made in aviation, especially in their propulsion systems. This is also recognized by Advisory Council for Aviation Research and innovation in Europe (ACARE), who provide a network of strategic research with the goal of making the air transport vision in Europe a reality. Therefore ACARE has set up specific goals to be met in 2050, called 'Flightpath 2050' [4]. The first and most repeated goal of ACARE is the following:

"In 2050 technologies and procedures available allow a 75% reduction in CO2 emissions per passenger kilometre and a 90% reduction in NOx emissions. The perceived noise emission of flying aircraft is reduced by 65%. These are relative to the capabilities of typical new aircraft in 2000." [22].

Fortunately technological developments have been made throughout the history of aviation. Between 1968 and 2014 the compound annual reduction rate in fuel consumption per passenger kilometre is 1.3% [1]. If this trend continues from 2000 to 2050, which is a course assumption, that would come down to a near halvation of the fuel consumption per passenger kilometre. As CO2 is not a pollutant but a mere end product of complete combustion of hydrocarbon fuels, it is fair to say the CO2 emissions are directly related to fuel consumption. So CO2 emissions could be halved between 2000 and 2050, but a 75% reduction seems like a very steep challenge. Drastic new concepts will have to emerge to meet this target. The current reduction in fuel consumption is mainly possible due to improved aircraft engine efficiencies by increasing the engine pressure ratio and turbine inlet temperature. However it is precisely these improvements that tend to increase NOx emissions [23]. Through other technological advancements it may be possible to mitigate that drawback.

2.2. AHEAD: Advanced Hybrid Engines for Aircraft Development

The AHEAD project aims to accelerate the technological advancements by investigating the feasibility of an unconventional aircraft powered by innovative engines [5]. AHEAD is short for Advanced Hybrid Engines for Aircraft Development and is a partly EU-funded group of technical institutions and universities. A large part of its research is aimed towards the development of a hybrid fuel aircraft engine. This contra-rotating turbofan engine will be powered by both liquid hydrogen and biofuel. The cryogenic hydrogen will be combusted in the first combustion chamber. The hot exhaust gasses of this combustion chamber then allow for flameless combustion of biofuel in the second combustor. As a large amount of the produced power originated from the combustion of hydrogen, the only CO2 emissions come from the flameless combustion of the biofuel. NOx emissions also have the potential to be very low because the combustors are staged.

The current study is also part of the AHEAD research and will focus on the hydrogen combustion chamber of the engine. It is obvious that significant CO2 reduction is possible with this engine configuration. The potential NOx reduction on the other hand is less evident. To understand this potential a closer look must be taken at the formation of nitrogen oxides.

2.3. NOx Formation

In exhaust gasses nitric oxide (NO) is by far the most abundant species of nitrogen oxides. NO is mainly formed through a mechanism referred to as the Zeldovich mechanism [87]. This mechanism is highly sensitive to temperature of the exhaust gas and is therefore also referred to as thermal NOx. The chemical reactions of the Zeldovich mechanism are presented in eq. (2.1).

$$\begin{aligned} N_2 + O &\rightarrow NO + N \\ N + O_2 &\rightarrow NO + O \\ N + OH &\rightarrow NO + H \end{aligned} \tag{2.1}$$

The first reaction is the NO formation rate governing reaction as its activation energy is relatively high. Therefore the reaction rate increases rapidly at high temperatures, typically 1800 K [84] [51]. This temperature dependence is visualised using fig. 2.1.

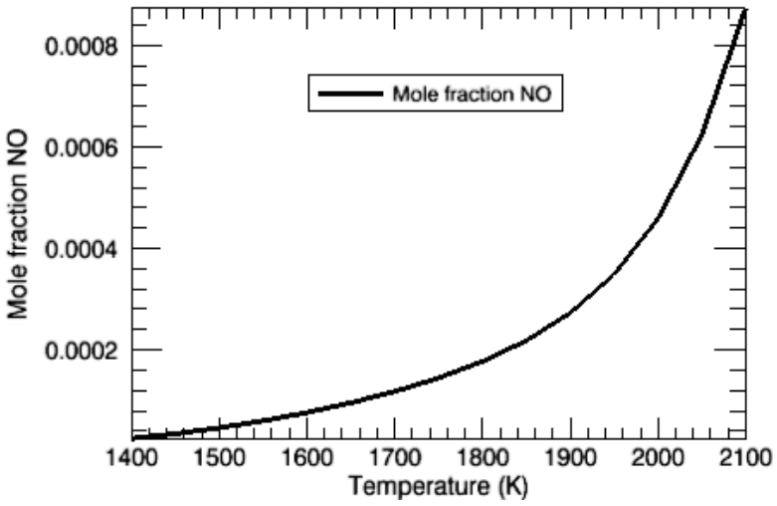

Figure 2.1: NO concentration vs Temperature
Source: *Zajemska et al.*[51]

The formation of nitrogen dioxide (NO2), the second most abundant NOx species is governed by the concentration of NO. So a similar temperature dependence as presented in fig. 2.1 exists for NO2. It can thus be concluded that NOx formation is greatly affected by temperature. In fact the reaction rates of the NOx forma-

tion reactions increase exponentially with temperature.

At equal equivalence ratio the flame temperature caused by hydrogen combustion is higher than that from kerosene combustion. This would provide for higher NOx emissions from hydrogen combustion compared to kerosene combustion. However, hydrogen has much broader flammability limits than kerosene as illustrated in fig. 2.2.

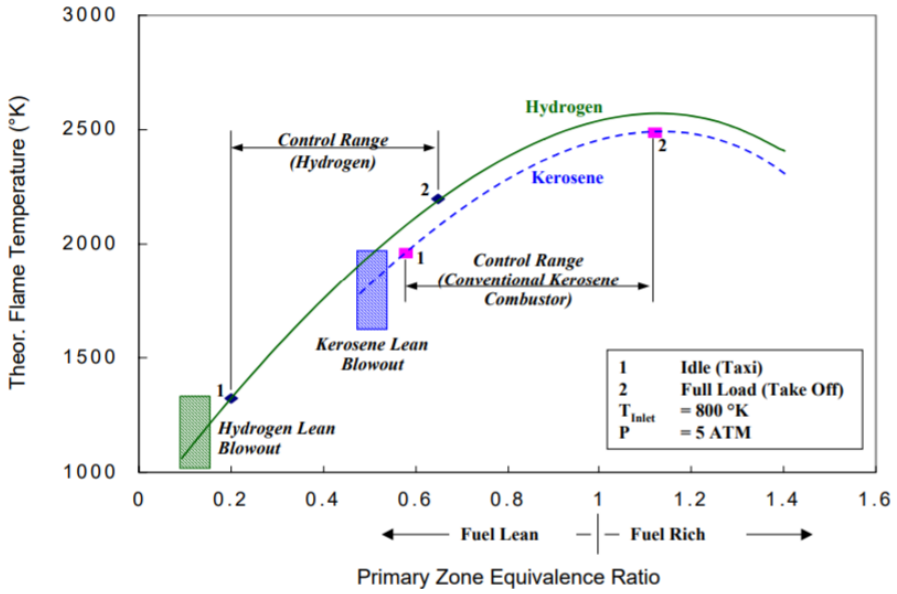

Figure 2.2: Flame temperature vs Equivalence ratio for hydrogen and kerosene under flight conditions
Source: *Brand et al.*[13]

From this figure it can be observed that hydrogen has a significantly lower lean blowout limit. This is the point where the ratio of fuel to air becomes too low to be combustable. Thus hydrogen can burn significantly leaner and therefore at lower temperatures. This gives hydrogen combustion the potential to produce less NOx emissions than kerosene combustion. This is only possible when the equivalence ratio of the combustion can be controlled. Therefore lean premixed combustors are becoming more popular in research and development. It should be noted that achieving perfectly premixed fuel and air is nearly impossible. In actual premixed combustors there will always be spatial and temporal fluctuations in the equivalence ratio and therefore in temperature. For lean mixtures the local mixtures that burn closer to the stoichiometric conditions (richer than the mean) will produce more NOx, while the leaner burning mixtures will produce less NOx. Since the reaction rates of NOx formation increase exponentially with temperature, the richer mixtures outweigh the leaner mixtures in terms of NOx production. To minimize NOx production it is therefore desirable to always burn at the overall equivalence ratio and thus to minimize any spatial or temporal unmixedness [30], Besides the NOx aspect, it is also desirable to have a good mixing quality of fuel and air as this provides for a more stable combustion [2].

Even though hydrogen has an extended lean blowout limit, there is a disadvantage that comes along with its high reactivity. As hydrogen has a much higher burning velocity than hydrocarbon flames, hydrogen flames are more prone to flashback than hydrocarbon flames. This increased flashback risk has to be taken into account when designing hydrogen combustion chambers.

2.4. Developments in Hydrogen Combustor Design

Over the past decades hydrogen combustion research has become increasingly popular in the field of power- and propulsion engineering. Figure 2.3 shows the amount of published documents related to the search term: *"hydrogen AND combust* AND ((aero engine) OR (gas turbine))"* as found on Scopus.
As mentioned before. This increased popularity is likely driven by the stricter emission regulations on aviation and power generation. From the relevant research performed there are two major design trends for

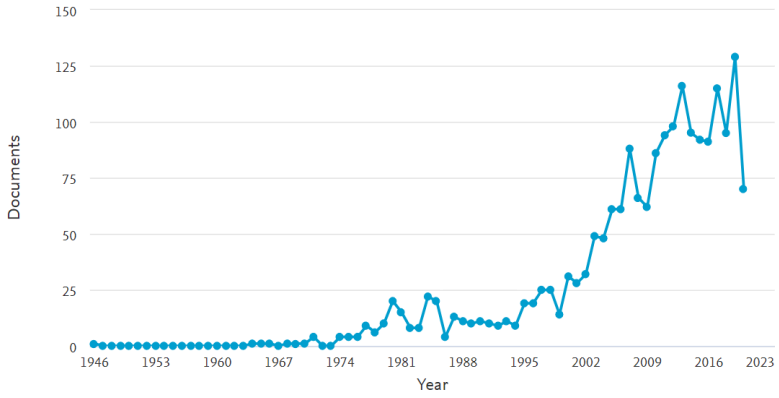

Figure 2.3: Annual published hydrogen combustion related documents on Scopus as of August 2020

hydrogen combustion that are able to achieve low NOx emissions and therefore appear to be viable alternatives to fossil fuel combustion. First is micromix combustion and second is lean premixed combustion.

2.4.1. Micromix combustion

Micromix combustion is quite different from most modern gas turbine combustion concepts in the sense that there is not a single large flame in the combustion chamber, but there are many small 'micro' flamelets distributed over the combustion chamber. In contrast to lean premixed combustion, micromix uses diffusion flamelets, providing an inherent resistance to flashback. Air is injected axially through air guiding planes. Perpendicular to these planes, hydrogen fuel is injected through distributed small ports (as a jet in cross-flow) and immediately combusted, forming flamelets of approximately 10mm. The flow pattern develops into an inner recirculation zone in the direction of the hydrogen jet and an outer recirculation zone on the other side. This flow pattern is illustrated in fig. 2.4. A closeup of the fuel and air injection of one flamelet is presented in fig. 2.5 [33][34].

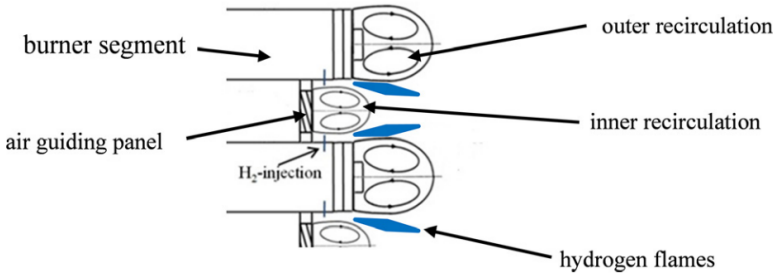

Figure 2.4: Micromix flamelets and recirculation zones
Source: *H. Funke* [34]

A shear layer forms between the inner recirculation zone and the free exhaust jet at the level indicated by y_{crit}. The hydrogen jet must not penetrate this shear layer to ensure a very short residence time of the mixture, ultimately leading to lower NOx emissions. If hydrogen would penetrate into the inner recirculation vortex, the hydrogen-air mixture would react and recirculate, increasing the residence time, temperature, and NOx emissions. Thus the recirculation zones do not partake in mixing, but merely assist to anchor the flame. The major challenges for the micromix technology are a sensitivity to fuel contamination, manufacturing complexity, and therefore cost.

2.4.2. Lean premixed combustion

Lean premixed combustion uses the large flammability limits of hydrogen to its benefit as discussed in chapter 2. The air and fuel mix to a mixture with equivalence ratio near the lean blowout limit before combustion to minimize NOx. A schematic image of this type of combustor is shown in fig. 2.6. In the schematic the air

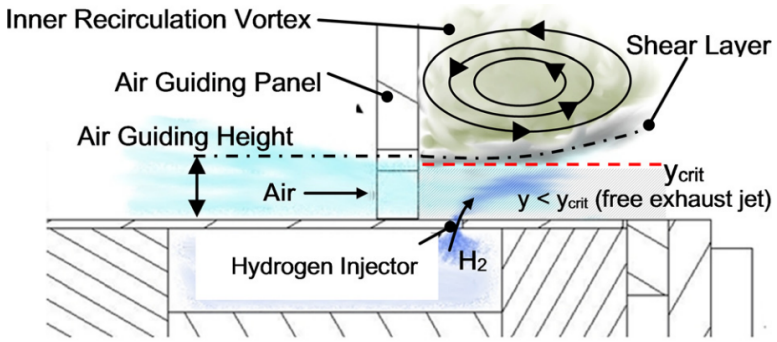

Figure 2.5: Micromix fuel and air injection
Source: *H. Funke* [34]

is injected axially and fuel is injected radially after the air has passed through a swirler. The gasses then mix inside the premixer to a more homogeneous state. Finally the mixture passes through another swirler before it is dumped in the combustion chamber, where it ignites. It should be noted that this is just one of many possible configurations of lean premixed combustors.

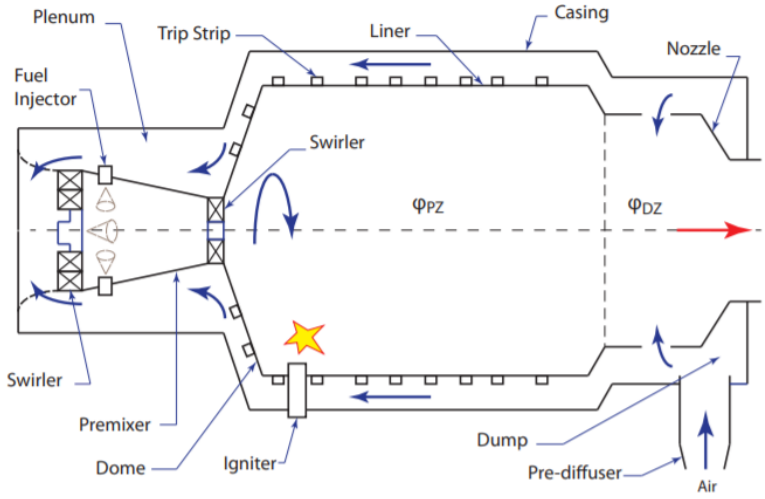

Figure 2.6: Schematic of lean premixed combustor
Source: *D. Dewanji* [20]

Staged lean premixed combustion
Another common configuration of lean premixed combustors is the staged lean premixed combustor. This concepts provides a solution for problems that may occur in lean premixed combustion. As the equivalence ratio during lean premixed operation is close to the lean blowout limit the stability margins are small. A relatively small oscillation can cause the flame to extinct. For premixed flames light-off and relighting is unreliably compared to diffusion flames. Therefore the staged lean premixed combustor concepts uses a primary zone that can be operated with a diffusion flame upstream of the secondary premixed zone. In fact this configuration allows for four modes of operation as is shown in fig. 2.7 [52] [31] [85].

- **Primary** - In the primary operation mode all fuel is supplied to the primary zone where it is immediately combusted in a diffusion flame with the incoming air. This mode is used for ignition and low loads.
- **Lean-Lean** - In this mode the fuel is supplied to both the primary and secondary nozzles. This ignites the partially premixed flame of the secondary zone and is used for intermediate loads.

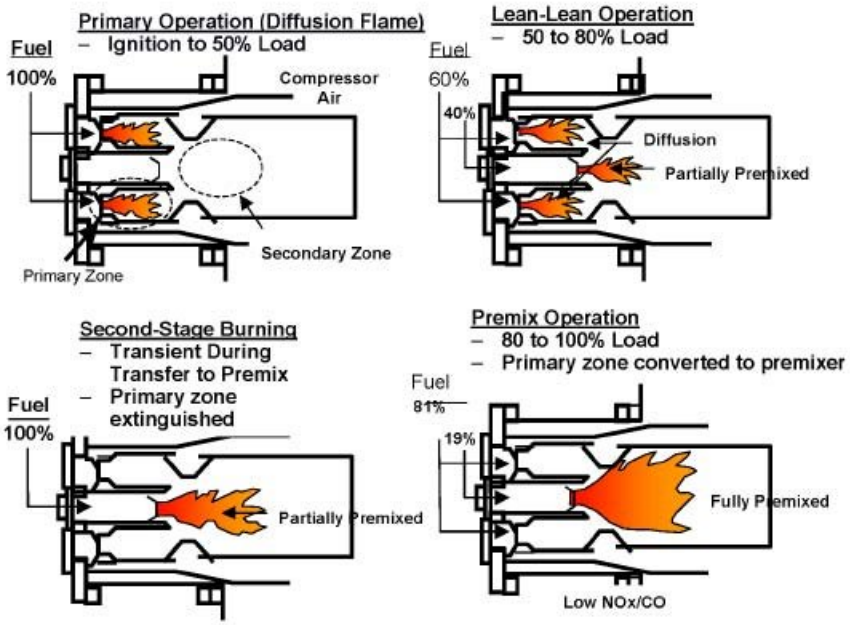

Figure 2.7: Modes of operation on staged lean premixed combustor
Source: *Meher-Homji et al.* [52]

- **Second-Stage Burning** - For this third mode of operation the fuel supply to the primary zone is cut off. The diffusion flame thus extincts in this zone and only a partially premixed flame in the secondary zone remains. This flame is not fully premixed for this mode as the fuel-to-air-ratio is very high in the secondary injector. This 'second-stage burning' is used as a transient stage from lean-lean operation to the final fully premixed operation.

- **Premixed** - In this final mode of operation the fuel supply is distributed mainly to the primary injectors. The flame is now extinct in this zone so the fuel and air can form a homogeneous mixture. The primary zone thus acts as a premixing chamber. The remaining fuel and air are also premixed in the secondary injector and combust in the secondary stage together with the mixture from the primary zone.

2.5. Swirl-stabilised Combustion

To reach their desired power output gas turbines require high flow rates. Therefore the flow velocity inside the combustion chamber is generally much larger than the flame speed. To still be able to maintain stable combustion a flame stabilization mechanism must be adopted. A commonly used mechanism is recirculation. A swirl generator can create a central (toroidal) recirculation zone where the local velocity is much lower. This provides for a larger residence time, ensuring stable and complete combustion with relatively low emissions. This section will look into swirl and its effect on the flow field inside a lean premixed combustor.

2.5.1. Swirl Generators

A swirler generates a tangential velocity component in the otherwise purely axial flow in the premixing tube. There are three main types of swirl generators. The first type is referred to as a axial swirler. In an axial swirler the axial flow can be deflected in tangential direction by guide vanes. The angle of the guide vanes affects the degree of swirl. Figure 2.10 illustrates this type of swirler. The second type is by radial/tangential injection of fluid in the axial flow. This type is referred to as a radial swirler and is presented in fig. 2.8. The final type of swirler is one where a rotating mechanical device initiates a swirling motion to the flow. [78] This final type is not very common in industrial application because of its complexity, but provides the benefit of adjustable degrees of swirl and is therefore attractive for some experimental investigations [8].

2.5.2. Central Recirculation Zone

The swirl creates a centrifugal force, forcing the flow outwards. This causes an outward radial pressure gradient to arise. The core of the swirling flow is thus at relatively low pressure, while the flow near the wall is at relatively high pressure. Once the flow reaches the combustion chamber the expansion causes the velocity to decrease and the pressure to recover, causing a positive axial pressure gradient downstream. If the axial pressure gradient, and thus the swirl, is large enough, a central toroidal recirculation zone forms with flow reversal near the centerline.

Another way of understanding this phenomenon is by looking at the simple radial equilibrium and the conservation of angular momentum. A swirling flow in a cylindrical tube can be described by the simple radial equilibrium, eq. (2.2). This means that tangential velocity component, axial velocity component, and pressure are all only functions of radius. The swirling flow in the premixing tube essentially behaves as a solid body rotation and is also known as a forced vortex flow. This means that the angular velocity (Ω) is constant along the radius and that tangential velocity (W) is expressed by equation eq. (2.3) [40].

$$p(r_o, x) - p(0, x) = \frac{\rho \Omega^2 r_o^2}{2} \tag{2.2}$$

$$W = \Omega r \tag{2.3}$$

Equation (2.2) gives the pressure difference between the outside edge of the vortex core $p(r_o)$ and the centerline $p(0)$ at axial position x. Imagine the flow reaches the sudden expansion of the entrance to the combustion chamber at x_1. When it reaches x_2 downstream of x_1, the vortex has expanded radially. As its angular momentum is conserved the angular velocity decreases quadratically with increasing radius. The left hand side of eq. (2.2) thus becomes smaller downstream of the sudden expansion, meaning that the pressure difference between outer edge and centerline decreases. As the average pressure increases with increasing area in subsonic flows, the pressure along the centerline must increase more that on the outside edge of the vortex core. This leads to a greater axial velocity reduction on the centerline than on the outside, which can ultimately cause a central toroidal recirculation zone if the effect is strong enough [35].

2.5.3. Swirl number

The Swirl number is a dimensionless number which helps to quantify the intensity of the swirl and can thus give an indication whether a recirculation zone will be formed. The general definition of the Swirl number is the ratio of axial flux of angular momentum (G_θ) to the outer radius of the annulus (r_o) times the axial flux of axial momentum (G_x) and is given by eq. (2.4) [8] [79]. The equations for axial flux of angular momentum and axial flux of axial momentum are given by eq. (2.5) and eq. (2.6) respectively. It should be noted that G_x is also known as axial thrust and has the unit of N.

$$Sw_0 = \frac{G_\theta}{r_o G_x} \tag{2.4}$$

$$G_\theta = \int_0^R (Wr)\rho U 2\pi r dr \tag{2.5}$$

$$G_x = \int_0^R 2\pi r \rho U^2 dr + \int_0^R 2\pi r p dr \tag{2.6}$$

In these equations U is the axial velocity component, W is the tangential velocity component, ρ is the fluid density, and p is the static pressure in any cross section of the swirling flow. It is however difficult to obtain the pressure distribution and exact velocity components of the flow. Therefore Beér and Chigier [8] suggested the pressure term in G_x can be omitted once the flow inlet conditions of the swirler are used to obtain the Swirl number. Equation (2.6) then reduces to eq. (2.7) and is only dependent on the axial velocity distribution at the swirler inlet.

$$G_x = 2\pi \int_0^R \left(\rho U^2 r\right) dr \tag{2.7}$$

For different types of swirl generators they were able to approximate the Swirl number based on the swirl generator geometry. For radial type swirlers the axial momentum flux of angular momentum can be expressed using eq. (2.8). In this equation $\dot{m}$ is the mass flow rate, σ is the ratio of the average tangential velocity component to the average axial velocity component, and L_{slot} is the axial length of the slots through which the fluid is radially/tangentially injected. The dimensionless number σ can be assumed fully dependent on the swirler geometry and is approximated by eq. (2.9).

$$G_\theta^{'} = \sigma \frac{\dot{m}^2}{\rho 2\pi L_{slot}} \tag{2.8}$$

$$\sigma(\psi) = \frac{1}{1-\psi}\left(\frac{\tan\psi}{1+\tan\psi\tan(\pi/n)}\right) \tag{2.9}$$

Here, ψ represents the blockage factor caused by the thickness of the vanes (t) (eq. (2.10)), n is the total number of radial vanes, and α is the inlet angle of the vanes w.r.t. the radial direction. So α equal to zero would indicate a purely radial inlet. A schematic of the radial swirler and its relevant dimensions is presented in fig. 2.8.

$$\psi = \frac{nt}{2\pi R_1 \cos\alpha} \tag{2.10}$$

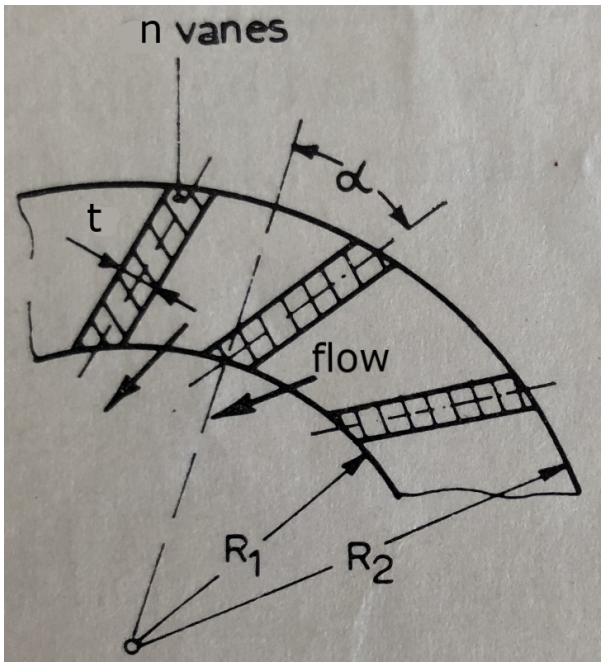

Figure 2.8: Schematic section of radial swirl generator
Source: Adapted from *J. M. Beér* [8]

If axial momentum is assumed constant over the radius ($\rho u^2 = const$) the axial thrust reduces to eq. (2.11). The Swirl number then finally reduces to eq. (2.12) where A is the cross sectional area of the swirler exhaust.

$$G_x^{'} = \pi R^2 \rho U^2 \tag{2.11}$$

$$Sw = \frac{\sigma \dot{m}^2}{2\pi^2 R^3 \rho^2 U^2 L_{slot}} = \frac{\sigma A^2}{2\pi^2 R^3 L_{slot}} = \frac{\sigma R}{2L_{slot}} \tag{2.12}$$

A variation on the radial swirl generator is the movable block swirl generator. This swirler allows for adjustment of the Swirl number without replacing any parts. A schematic of the movable block swirler is presented

in fig. 2.9. The 'lower' blocks are all connected and can be rotated about the centerline. In this example, if they are fully rotated in clockwise direction they block the tangential air inlet slots. The air is then only injected radially and no swirl is generated. Rotating the blocks towards the opposite side opens up tangential air injection slots and closes the purely radial slots at the same time. This angle of adjustment (ξ) is thus proportional to the Swirl number. It is defined by eq. (2.12) in which σ is now given by eq. (2.13).

$$\sigma = \frac{2\pi}{n\xi_m} \sin\alpha \frac{\cos\alpha[1+\tan\alpha\tan(\xi/2)]\,(\xi/\xi_m)}{\{1-[1-\cos\alpha(1+\tan\alpha\tan(\xi/2))]\xi/\xi_m\}} \tag{2.13}$$

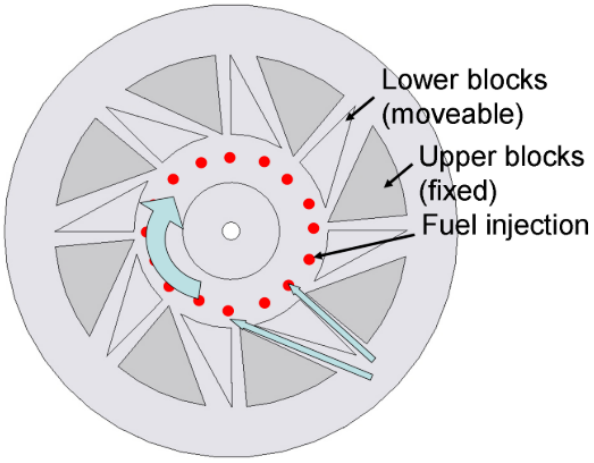

Figure 2.9: Schematic of movable block swirl generator
Source: *S. Terhaar* [83]

For axial swirl generators the Swirl number can also be reduced under a few assumptions. If the vanes are assumed thin and the axial velocity distribution is assumed constant over the radius eq. (2.5) and eq. (2.6) reduces to eq. (2.14) and eq. (2.15) respectively.

$$G_\theta^{'} = 2\pi\rho U^2 \tan(\phi) \frac{R_n^3 - R_h^3}{3} \tag{2.14}$$

$$G_x^{'} = \pi\rho U^2 (R_n^2 - R_h^2) \tag{2.15}$$

In these equations ϕ is the vane angle w.r.t. the axial direction, R_n and R_h are the full tube radius and the hub radius of the swirl generator respectively. These dimensions are also indicated in fig. 2.10. In the end, the Swirl number for an axial type swirl generator can be approximated by eq. (2.16).

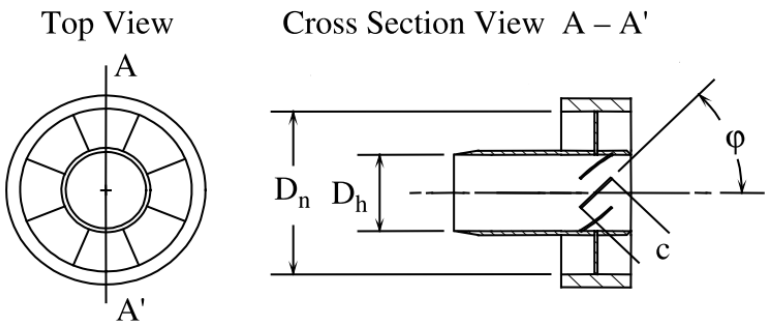

Figure 2.10: Schematic of axial swirl generator
Source: Adapted from *Y. Huang* [40]

$$Sw = \frac{2}{3}\left[\frac{1-(R_h/R_n)^3}{1-(R_h/R_n)^2}\right]\tan(\varphi) \tag{2.16}$$

An alternative configuration of the axial vane swirler is one with helical vanes in stead of straight vanes. This helical vane shape is defined by eq. (2.17).

$$\tan\phi = \frac{r}{R_n}\tan(\varphi_0) \tag{2.17}$$

The vane angle at the trailing edge is thus greatest at the tip (ϕ_0) and reduces towards the hub. This changes the angular momentum flux and ultimately the Swirl number to the theoretical expression given by eq. (2.18), in which the blockage factor ψ is defined by eq. (2.19).

$$Sw_{hel} = \frac{G_\theta^{'}}{G_x^{'}R_n} = \frac{1}{1-\psi}\left(\frac{1}{2}\right)\frac{1-(R_h/R_n)^4}{1-(R_h/R_n)^2}\tan(\varphi_0) \tag{2.18}$$

$$\psi_{hel} = \frac{n\int_{R_h}^{R_n}\frac{t}{cos(\varphi)}\mathrm{d}r}{(R_n^2-R_h^2)\pi} \tag{2.19}$$

2.5.4. Vortex breakdown

When a confined swirling flow encounters a diffuser the axial velocity on the centerline is reduced. This deceleration increases with increasing Swirl number. Increasing the swirl further beyond a critical value gives rise to sudden vortex breakdown (VB) [10], which causes a central recirculation zone to form [35] [40]. Beran and Culick [10] used numerical simulations to show the hysteresis loop (fig. 2.11) in VB and consequent formation of the recirculation zone. Vortex breakdown is thus not a gradual, but an abrupt phenomenon for an increasing swirl intensity.

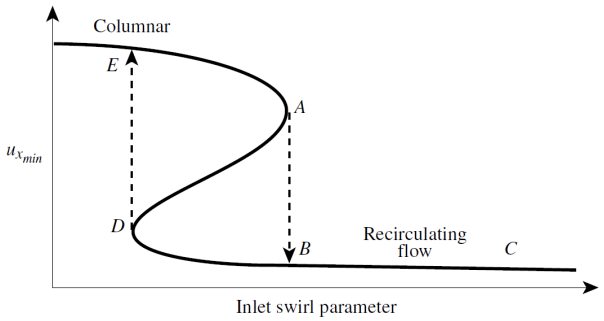

Figure 2.11: Hysteresis in minimum axial velocity in vortex core for variation in swirl parameter
Source: *E.M. Greitzer et al.* [35]

There have been many types of VB classified. Some authors have identified up to seven different types [29] [40]. At high Reynolds numbers ($Re > 10^4$), Novak and Sarpkaya [59] found two types of VB prevailed: the bubble type and the cone type. A schematic of the these VB types are presented in fig. 2.12 and fig. 2.13 respectively. For bubble type VB the vortex core rapidly expands after reaching a stagnation point. Then, at a larger radius, the flow collapses and gives rise to axial flow reversal. The axial velocity then turns positive again close to the initial stagnation point and has the potential to continue as a new vortex core with a larger radius. This final stage is not always observed though. Novak and Sarpkaya suggested that the cone type originates from a rapidly precessing spiral type VB, which is commonly found at lower Re.

Billant et al. [11] investigated swirling jets being dumped into a larger reservoir. They observed the same two distinct types of VB: cone and bubble VB. In contrast to Novak and Serpkaya it was hypothesized that the cone type VB originates from the bubble type VB at very high Re, where the wake of the bubble is highly turbulent

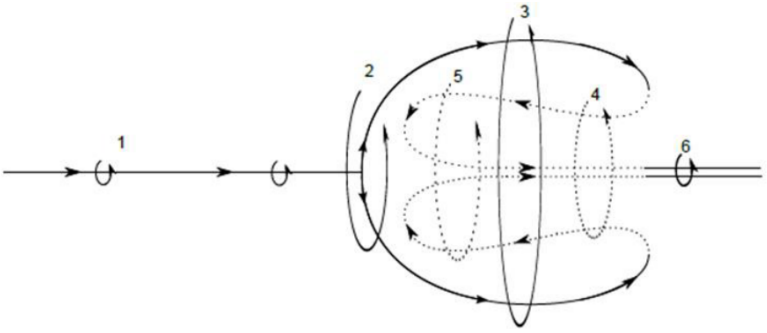

Figure 2.12: Schematic of bubble type vortex breakdown
Source: *T. Jindelt et al.* [42]

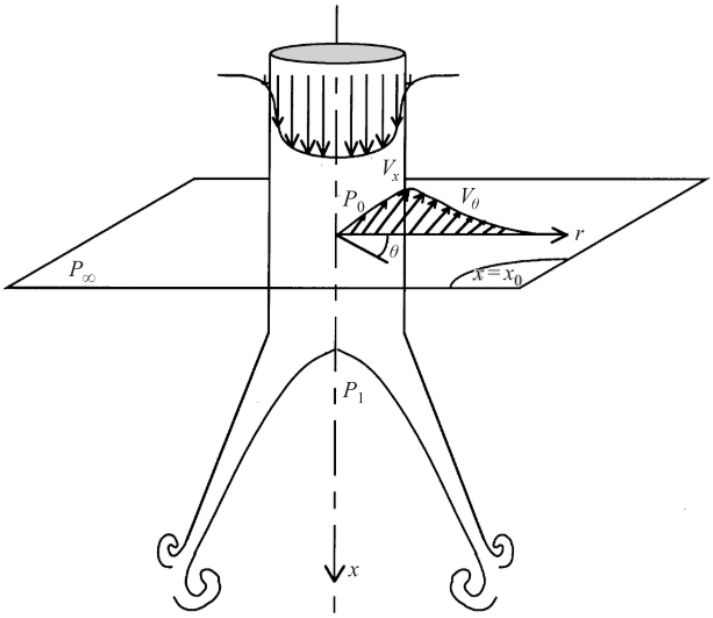

Figure 2.13: Schematic of cone type vortex breakdown
Source: *P. Billant et al.* [11]

and starts very close to the stagnation point. However this was not confirmed as both VB types were found to occur seemingly at random occasion. Both types were also found to have axisymmetric and asymmetric forms. The axisymmetric forms were observed at lower Re and the asymmetric ones at higher Re. The cause between the distinction of the cone and bubble type was not explicitly found, but small instabilities in temperature were suggested. Later, Terhaar [83] found that the inflow velocity profile caused the distinction. By injecting a non swirling jet axially on the centerline of a swirling flow the author was able to influence the vortex breakdown type. In fig. 2.14 the observed VB type is presented for a range of investigated primary swirl numbers and amount of axial air injection (volume rate of non swirling jet to total volume rate (χ)). Injecting a non swirling jet decreases the effective Swirl number. This phenomenon is shown by the resulting Swirl number lines. It was concluded that a cone type VB is promoted at high primary Swirl numbers with relatively large amounts of axial injection.

2.6. Flashback

Flashback is the process of an upstream propagating flame. This phenomenon occurs when the burning velocity exceeds the flow velocity. Flashback must be avoided as it can cause significant damage to components that are not intended to withstand the high temperature of flames; premixing tube and swirl generator for

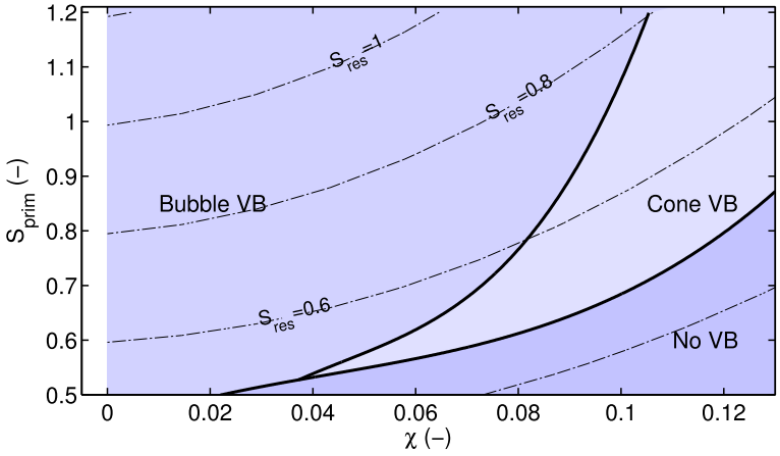

Figure 2.14: Observed vortex breakdown type for variation in primary Swirl number and axial injection
Source: *S. Terhaar* [83]

instance. Lieuwen [50] summarized the four distinct types of flashback: "turbulent flame propagation in the core flow, flashback due to combustion instabilities, flashback in the boundary layer, and flashback in the core flow due to alteration of vortex breakdown dynamics also known as combustion induced vortex breakdown (CIVB)" [38]. This final form is of particular interest for this study and is depicted in fig. 2.15. Oberleithner [60] found that for swirling lean premixed combustors this is the mechanism leading to flashback as instabilities are suppressed by density stratification caused by heat release of the flame. It should be noted that for correct operation of a gas turbine combustor flashback should be avoided, but not the VB as this also provides for the recirculation stabilized combustion.

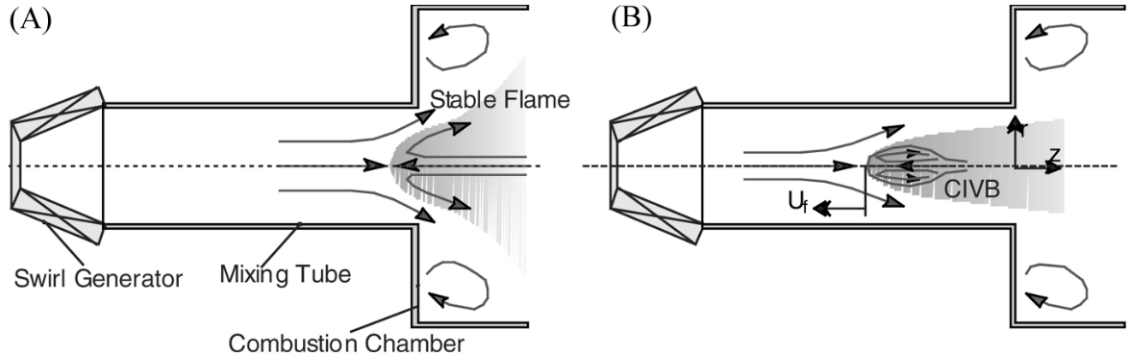

Figure 2.15: Flashback due to combustion induced vortex breakdown (CIVB): stable flame (A), flame moving upstream with the vortex breakdown bubble (B)
Source: *T. Lieuwen et al.* [50]

Taamallah et al. [82] combined an experimental and numerical study to investigate the flow field in a swirling combustor. The author found that the vortex breakdown at non-reacting conditions was of the cone type. This vortex breakdown was preceded by a precessing vortex core (PVC) which originates at the swirler centerbody. At reacting conditions this PVC starts rotating closer to the centerline with decreasing vorticity and follows a solid body rotation. The axial velocity deficit on the centerline increases and ultimately causes CIVB flashback as the vortex breakdown type changes from cone to bubble.

Burmberger and Sattelmayer [15] first proposed the concept of increasing the axial velocity on the centerline by a non-swirling jet to reduce the flashback propensity. Later, Terhaar [83] proved the potential of this concept by axially injecting air in the center of the swirling flow core. The combustion remained stable and flashback was avoided. This was numerically replicated by Veiga López [27] with RANS CFD with fairly good accuracy for non-reactive tests, but no reasonable predictability for the reactive tests. More recently, a LES numerical study was performed by Mira [56] with good agreement to the experimental investigation.

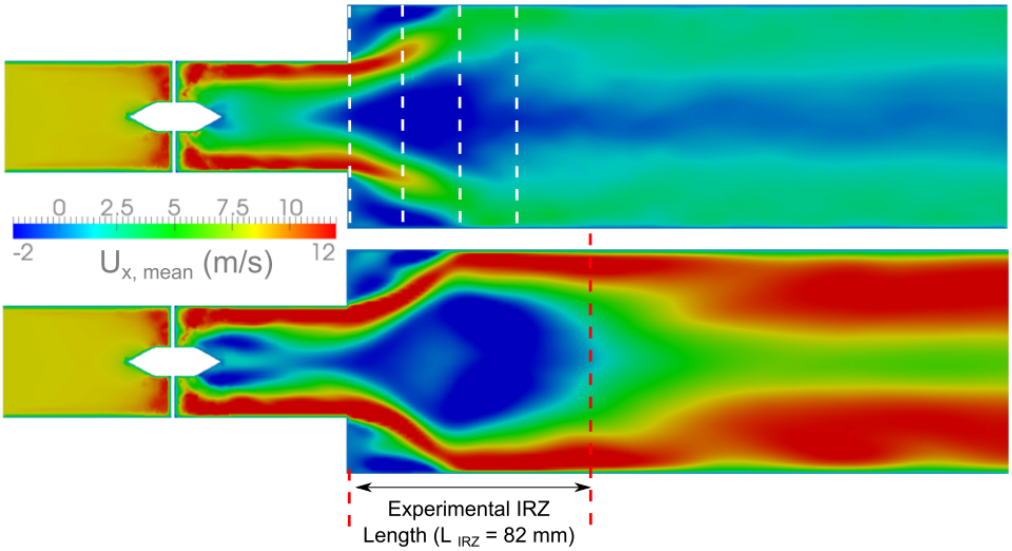

Figure 2.16: Axial velocity contours from LES simulation of a swirling lean premixed combustor: non-reacting (top), reacting (bottom) Source: *S. Taamallah et al.* [82]

2.7. Mixing

Another important aspect of desired performance besides flashback safety is a high degree of mixing. As mentioned in chapter 2 it is desirable to have a uniform temperature profile as this provides for minimum NOx production and higher stability of the combustion. This can be realised by thorough mixing of fuel and oxidant before combustion. Danckwerts [21] first introduced a parameter by which the mixing quality can be assessed of a binary mixture. It is usually referred to as unmixedness and is based on the variance (σ^2) of the measured concentration of one specie in the mixture. This variance and therefore the unmixedness can be evaluated both spatially (fluctuations in concentration in the area or volume of the temporally averaged field) or temporally (fluctuations in concentration in time of every measured point) [2] [74]. The spatial- and temporal unmixedness parameters are given in eq. (2.20) and eq. (2.21) respectively.

$$U_x = \frac{\sigma_x^2}{\sigma_0^2} = \frac{\frac{1}{N_i - 1}\sum_{i=1}^{N_i}\left(\overline{C^*}(i) - C_\infty^*\right)^2}{C_\infty^*\left(1 - C_\infty^*\right)} \tag{2.20}$$

$$U_t = \frac{\sigma_t^2}{\sigma_0^2} = \frac{\frac{1}{N_i N_t - 1}\sum_{i=1}^{N_i}\sum_{t=1}^{N_t}\left(C^*(i,t) - C_\infty^*\right)^2}{C_\infty^*\left(1 - C_\infty^*\right)} \tag{2.21}$$

In these equations σ_0^2 is the spatial variance of the concentration in the field just before the mixing process has commenced. C_∞^* is the perfectly mixed (homogenized) concentration. The concentration at location i at time t is represented by $C^*(i,t)$. The temporally averaged concentration at location i is represented by $\overline{C^*}(i)$. N_i and N_t represent the number of pixels (number of measured points in the field) and the number of timestamps recorded of the mixing process respectively.

2.8. Particle Image Velocimetry

Particle Image Velocimetry (PIV) is a non-intrusive quantitative flow measurement technique that has its roots in Laser Speckle Velocimetry (LSV) [24] and has known much development since [12]. The technique is based on tracking the displacement of particles in the flow between short time intervals. These small particles are added to the flow and are known as seeding particles or tracing particles. Their displacement can be tracked as they are briefly illuminated by two consecutive planar laser pulses and their scattered light is

recorded by a digital imaging device (usually a CCD or CMOS camera) positioned perpendicular to the illuminated plane. A schematic of a PIV measurement system is presented in fig. 2.17 [32].

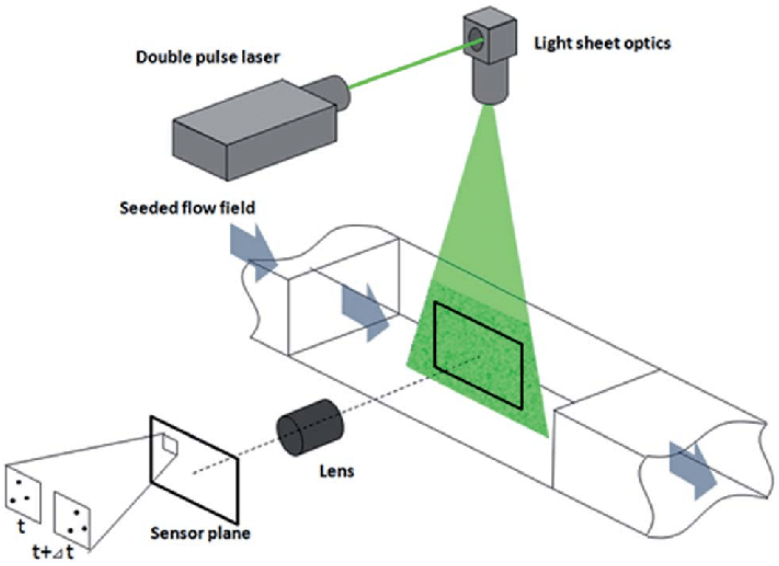

Figure 2.17: Schematic diagram of PIV system
Source: *Z. Sun et al.* [81]

When a seeding particle is carefully selected to accurately follow the flow, in the simplest sense, the velocity and in plane direction of the flow can be determined by dividing the displacement by the time interval between two laser pulses.This form of individual particle tracking is actually a similar but different measurement technique called Particle Tracking Velocimetry (PTV). In PIV, the velocity vector is not determined by tracking a single particle, but rather by cross-correlation analysis of particle patterns in a smaller sub-domain or interrogation window. The average particle displacement in such a window is determined by the correlation peak found in the analysis. Knowing the image magnification and time interval between two consecutive laser pulses, the average displacement can ultimately be converted to a velocity vector for that window. A schematic of the processing of PIV images is given in fig. 2.18.

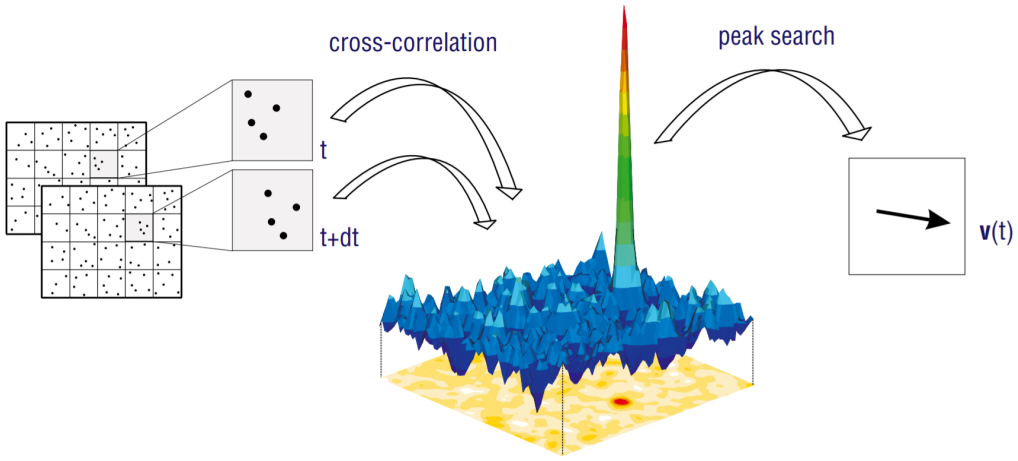

Figure 2.18: Schematic of processing PIV images
Source: *LaVision* [46]

Cross-correlation analysis requires an appropriate seeding particle density (number of seeding particles per observation volume). If this figure is low PTV is more appropriate. For intermediate values, PIV can be employed [68]. If the seeding density is too high, individual particles overlap on the images and no accurate

correlations will be found. Such high seeding densities are more applicable to LSV [66]. The effect of seeding density on the image is presented in fig. 2.19.

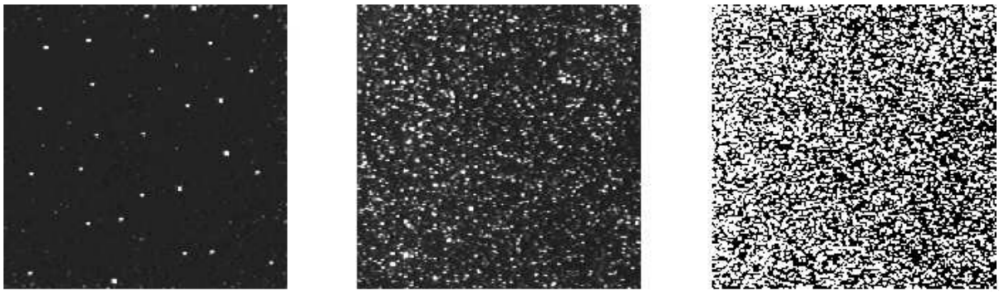

Figure 2.19: Low seeding density (PTV) (a), medium seeding density (PIV) (b), and high seeding density (LSV) (c)
Source: *M. Raffel et al.* [68]

Besides a suitable seeding density, the type of seeding particle must also be carefully selected. One must take into account the velocity offset between particle and flow and also the scattering effectiveness of the particle. Ideally the particle velocity is identical to the flow velocity, but in reality there is a slip velocity that must be minimized. That velocity can be estimated by equation eq. (2.22) where v_p and v_f are the particle and flow velocity respectively. The particle radius is represented by r_p, μ is the fluid dynamic viscosity, and ρ is the density.

$$v_p - v_f = \frac{2}{9}\frac{r_p^2\left(\rho_p - \rho_f\right)}{\mu}\frac{dv_p}{dt} \tag{2.22}$$

So if the particle and flow have identical density the particle follows the flow perfectly. This is achievable for liquid flows, but not for gaseous flows. Therefore the seeding particles in gaseous flows often have a very small diameter. Oil droplets of 1-3 μm diameter and TiO_2 are common examples while liquid flows generally equip silver coated hollow glass spheres or something similar as tracers.

Table 2.1: Diameter and density of common PIV seeding particles

Particle	Diameter	Density
Vegetable oil	1-3 μm	0.9 g/cm^3
TiO_2	0.2-0.5 μm [32]	3.9-4.2 g/cm^3 [45]
Glass hollow spheres	1-100 μm [45]	0.06-0.8 g/cm^3 [18]

The scattering efficiency of a seeding particle is proportional to the (particle-to-fluid) ratio of refractive indices, the particle diameter, and inversely proportional to the light wavelength. A larger particle thus increases the scattering efficiency, but also increases the slip velocity. Therefore a trade-off must be made when selecting a seeding particle. The image resolution must then be adjusted for the particle diameter. A pixel size of the recorded images should ideally be in the range of half a particle diameter [32]. If a particle is much smaller than a pixel a systematic error known as peak locking occurs, which translates to a maximum positioning error of 0.5 pixel as particle positions then tend to be rounded to integer pixel values [7]. An example of under-resolved and well-resolved imaging is presented in fig. 2.20. If a particle is much larger than a pixel the contrast of the image would suffer as individual particles may start overlapping.

Other considerations to be made for a successful PIV experiment are the laser pulse duration, the interrogation window size, and the laser sheet thickness. The pulse duration or pulse width must be as short as possible in order for the scattering particles to be captured as dots rather than streaks. This can generally be achieved if the diameter of the particle is much less than the time it takes for a particle to move by one diameter. For modern lasers this generally is not a problem as the pulse width is smaller than 10 ns [67].

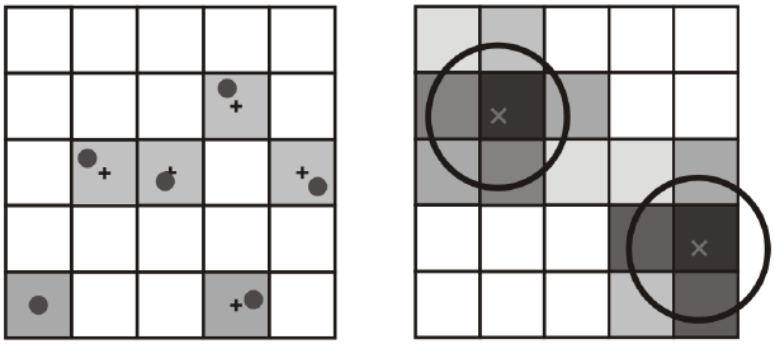

Figure 2.20: Digital imaging of small particles: under-resolved, leading to peak locking (left), well-resolved (right)
Source: *F. Scarano* [32]

For an optimal PIV experiment the in-plane movement of particles should be smaller than a quarter of the window size to ensure enough particles stay within the frame during the two laser pulses and can be used for cross-correlation analysis. On the other hand the interrogation window should not be so large that the particles in that window have vastly different velocities as this causes multiple cross-correlation peaks to arise [32].

As a design rule particles should not have more out-of-plane displacement than one quarter of the sheet thickness [32]. Increasing the sheet thickness will increase the observation volume. This will ensure fewer particles move through the sheet in between laser pulses, making it easier to cross-correlate the images. On the other hand, it will also cause a worse resolution and increase the perspective projection error on the in plane velocity caused by the out of plane velocity component. For highly 3-dimensional velocity fields this systematic perspective projection error can be up over 15% [68]. The sheet thickness is generally set in the order of 2 mm with the help of lenses for 2-dimensional (standard) PIV [49] [36]. The only way to completely cancel the perspective projection error is to include the measurement of the third velocity component by a more advanced method such as stereoscopic [86][25] or tomographic PIV (tomo PIV) [77][25].

2.8.1. PIV Optics

A dual-pulsed laser suited for PIV generally emits two near-circular laser beams with a diameter in the order of 5-10 mm. This diameter depends on the pulse energy. The emitted beams need to be deformed to form two thin overlapping laser sheets in the area of interest. This can be achieved by inserting specific lenses in the laser light. Positive (convex) lenses (lenses that have positive focal length can be used to converge the light, whereas negative (concave) lenses can be used to diverge the light. This is illustrated in fig. 2.21.

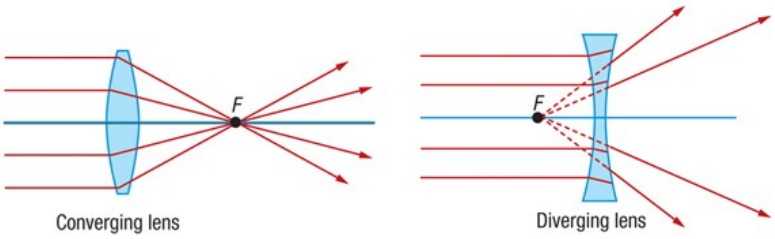

Figure 2.21: Converging vs diverging lens [28]

The beams emitted from the laser head are generally slightly diverging. To create a focal point near the area of interest, effectively an extremely weak positive lens (convex lens with very far focal point) must be introduced in the beam. A more practical solution is to use a combination of a concave and convex lens. Their spacing and individual focal lengths govern the effective resulting focal point. When a focal point is created at the desired location, the beam must be opened up to form sheet. This can be done with a cylindrical concave lens. Cylindrical lenses only change the direction of light over a single axis compared to both axes for spherical lenses.

2.9. TU Berlin Experiments

Reichel combined the topics discussed above in his research. The author experimentally investigated the flow field, mixing quality and emissions of a hydrogen fueled, lean premixed, swirl-stabilised combustor with axial air injection (AAI) in a fourfold publication [71–74] as part of the author's PhD thesis [70] within the framework of the AHEAD project at the TU Berlin. The investigated combustor was equipped with circumferentially distributed axial fuel injection ports, tangential/radial air injection for swirl generation, centerline AAI, straight premixing tube, and a sudden expansion to the cylindrical combustion chamber. This combustor is presented below in fig. 2.22.

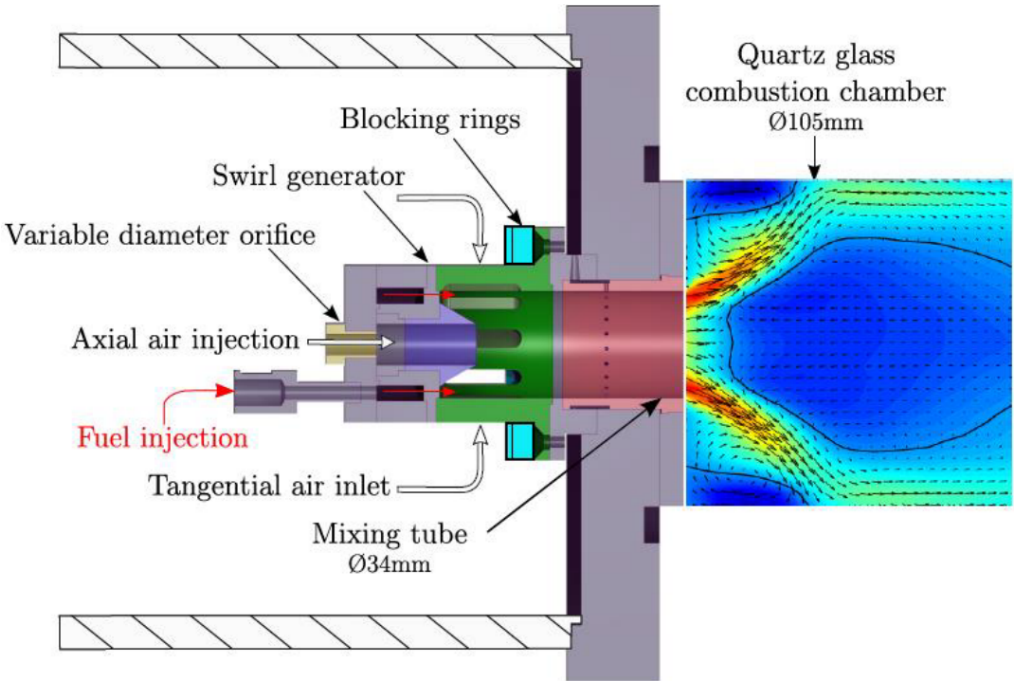

Figure 2.22: Schematic of the lean premixed combustor with axial air injection used by Reichel et al.
Source: *T. Reichel et al.* [70]

Reichel performed both isothermal and reacting experiments at two different Swirl numbers and two quantities of AAI. The variation in swirl intensity were achieved by installing different blocking rings on the radial swirler inlet, effectively changing the slot length (see eq. (2.12)). The quantity of axial air injection was controlled by a variable diameter orifice on the centerline inlet. For the isothermal experiment, a plexiglass model of the combustor was used and the hydrogen and air were both exchanged for water. For the flow field analysis a 2D Particle Image Velocimetry (PIV) was performed with seeding in all streams. This experimental setup is presented in fig. 2.23. The PIV results of the axial velocity component for a Swirl number of 0.9 are presented in fig. 2.25. It can be observed that increasing the axial air injection quantity to a medium amount has a significant effect on the axial velocity in the mixing tube, but not on the flow field in the combustion chamber. Only with a 'high' axial air injection quantity does the flow field in the combustion chamber change towards a plug velocity profile.

For the mixing quality experiment a fluorescent rhodamine 6G dye was added to the water representing the fuel and Planar Laser-Induced Fluorescence (PLIF) was performed with the same Nd:YAG 532 nm laser as was used in the PIV experiment. In such an experiment a higher concentration of the fluorescent stream (in this case fuel) in an illuminated cross-sectional plane emits more light and thus appears brighter on the recording camera sensor. The PLIF setup is presented in fig. 2.24.

The reacting experiments employed the same PIV setup for the flow field and used OH- Chemiluminescence

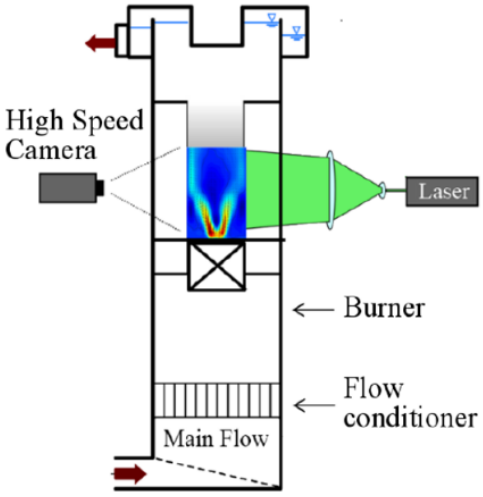

Figure 2.23: PIV setup of TU Berlin Experiment
Source: *T. Reichel*[74]

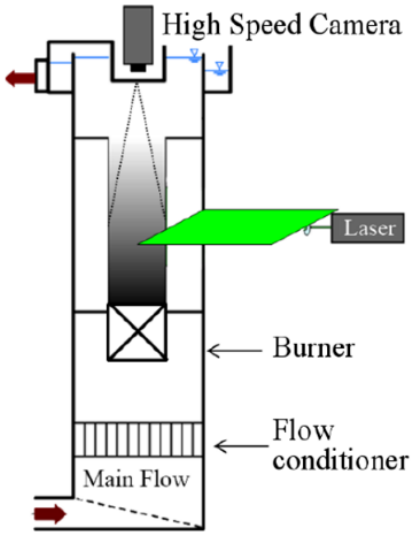

Figure 2.24: PLIF setup of TU Berlin
Source: *T. Reichel*[74]

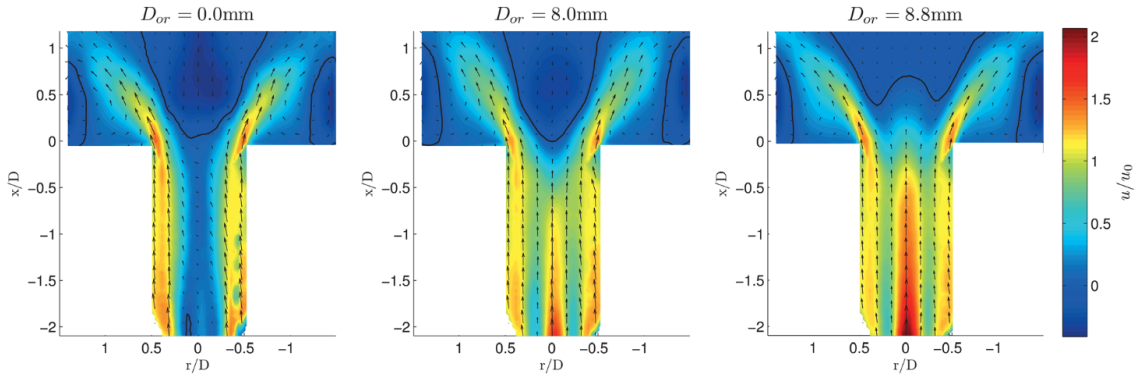

Figure 2.25: PIV results of axial velocity component at Swirl number of 0.9 with varying axial air injection quantity: 0% (left), 7.5% (middle), 12.5% (right)
Source: *T. Reichel et al.* [73]

to capture the flame location [72]. The reacting flow fields were quite different from the isothermal flow field as the heat release significantly influences the flow. In fact, the axial location of the stagnation point leading vortex breakdown moved upstream for all conditions when changing from non-reacting to reacting experiments. Despite this, the axial location of VB (the upstream stagnation point) in the isothermal conditions was found to be a good indicator of flashback resistance. This was determined because a downstream shift in stagnation point in cold-flow conditions also lead to a downstream shift in reacting conditions. This metric of flashback propensity in cold flow experiments is thus best evaluated qualitatively. Furthermore, it was concluded that a high initial Swirl number was beneficial for both stability and mixing quality. Additionally, from the reacting tests it was determined that increasing fuel momentum can cause the type of vortex breakdown to change from bubble to cone. This cone type is found to be less prone to flashback. It was also found that at high initial swirl intensity and high amount of AAI the mixing quality improved compared to low AAI. Finally, it was concluded that axial air injection suppressed flashback over the entire investigated operating range [70].

2.10. Literature Assessment

The current study recognizes the great potential of the suggested combustor configuration by the AHEAD project and wishes to elaborate on the research by Reichel. Three main points of improvement were identified in the concluded studies, which could be improved upon in future studies.

The first remark with the concluded work is in the isothermal mixing part. It is implied that using water in both streams resembles the mixing of gaseous hydrogen and air. At high *Re* flow this may generally be true as the mixing is then governed by turbulence [55]. However in the boundary layer, where locally the *Re* is low, mixing is governed by molecular diffusion [44]. The mass diffusivity of hydrogen in air is four orders of magnitude larger than the self diffusivity of water [39], which could cause a significantly different mixing quality. Therefore it is suggested that a combination of fluids is used with similar mass diffusivity as that of hydrogen in air. For instance air could be dissolved into CO2 to simulate the mixing process with relatively safe and cheap gasses while still achieving a similar interdiffusion coefficient [19]. Table 2.2 presents some relevant diffusion coefficients and Schmidt numbers of gasses and liquids at approximately 10°*C*. The Schmidt number is the ratio of momentum diffusivity (kinematic viscosity) to mass diffusivity. It thus gives an indication of how large the effect of mass diffusion is on the mixing process, a smaller value indicating a larger effect. So for the mixing of liquids, molecular diffusion has a much smaller effect than for the mixing of a highly diffusive gas, like hydrogen, into air [44].

Table 2.2: Diffusion coefficients and Schmidt numbers of some gasses and liquids

Fuel stream	Air stream	Mass diffusivity [m^2/s]	Schmidt number [-]
Hydrogen (g)	**Air (g)**	**7.10E-05** [19]	**0.21**
Helium (g)	Air (g)	6.58E-05 [19]	0.22
Air (g)	Air (g)	2.20E-05 [19]	0.67
Air (g)	CO2 (g)	1.48E-05 [19]	0.54
Water (l)	Water (l)	2.30E-09 [39]	388
Ethanol (l)	Water (l)	8.40E-10 [19]	1062

A second point of improvement would be the field of view. The flow field measurement was performed on a single plane coinciding with the centerline of the combustion chamber. The flow field inside the mixing tube is only investigated for a single Swirl number and in a single plane (see fig. 2.25). The flow field inside the mixing tube is just as relevant as that inside the combustion chamber and ideally the three dimensional flow field could be captured to learn even more. Capturing the tangential velocity component as well, would allow for the effective Swirl number to be obtained from the experimental results. The mixing quality was also investigated at only one cross-section downstream of the mixing tube perpendicular to the centerline. More axial positions of the measurement plane, also inside the mixing tube, could give insight into the required length of the mixing tube.

A final remark is that, both the swirl and AAI were set to only two different setpoints as the goal was to improve an existing design and not to study the effects of the two phenomena. Evaluating more setpoints would give more insight in the individual and combined effects of swirl and AAI. Additionally, the swirl intensity could be varied by different swirl generator types. This could have a significant effect on the flowfield as the swirler efficiency is heavily dependent on the type [8].

2.11. Research Definition

These three suggested points of improvement were deemed too sizable to be rigorously implemented in a single MSc thesis. It was therefore decided to focus on the flow field analysis regarding flashback resistance. Therefore, the research objective of this study is:

"**To determine the effect of axial air injection and swirl intensity on the flashback resistance of a lean premixed gas turbine combustor for axial- and radial vane swirl generators by conducting Computational Fluid Dynamics and Particle Image Velocimetry.**"

To remain feasible, these relationships are investigated through isothermal (non-reacting) simulations and experiments only. It should also be noted that the focus of this study is on the experimental work. The numerical simulations in the form of CFD are mainly intended to support the results obtained from the PIV experiments. The CFD simulations are thus of relatively low fidelity. Another limitation of this study is that

it is not possible to perform this experiment with hydrogen because as of yet the permits and certifications necessary to work with hydrogen are not in place at the relevant TU Delft facilities. For PIV experiments this is not really a problem because many fluids including liquids can be used to simulate the hydrogen-air flow field with good accuracy as long as the Reynolds- and Swirl number are similar. In fact multiple aerodynamic PIV investigations have exchanged the gasses for liquids in isothermal experiments [80] [74]. The design of the experimental setup is further discussed in chapter 3.

A number of research questions were also formulated to guide the study. These are listed below.

- **What is the effect of the axial air injection on the flashback propensity?**
- **What is the effect of the Swirl number on the flashback propensity?**
- **What is the difference in flashback propensity between axial vane swirl generators and radial vane swirl generators?**
- **How much does the Swirl number decrease along the mixing tube?**
- **What is the difference between the geometric Swirl number and the effective Swirl number for axial- and radial swirlers?**
- **What is the effect of fuel momentum on the Swirl number?**
- **What is the effect of fuel momentum on the flashback propensity?**

3

Methodology: Design

In this chapter, the methodology regarding the design of the experimental model is discussed. First the goals of the study and the design requirements are stated and explained in section 3.1. Following this, the design procedure of the individual components is discussed in section 3.2. Finally, the adopted mass flow rates are presented in section 3.3.

3.1. Design Goals and Requirements

The goal of the study is to determine the effect of the quantity of axial air injection (AAI) and Swirl number on the flashback propensity of the swirl-stabilised combustor. From literature the best indicator for this flashback propensity in cold flow conditions was found to be the axial location of the stagnation point, leading the vortex breakdown. If vortex breakdown is present, this stagnation point is expected to be located near the central axis of the mixing tube and on an axial position close to the sudden expansion from the mixing tube to the combustion chamber or 'dump' as seen in previous experiments [62] and simulations [27]. To obtain this location of the stagnation point, at least the axial velocity component must be measured on the central axis (or centerline).

The two investigated variables influencing this propensity of flashback are the AAI fraction of volume flow (Ψ) and the Swirl number. The AAI fraction can simply be obtained by logging the input flow rates of the different streams. The Swirl number requires considerably more effort. As the experimental model will be designed to custom specifications, it is deemed too course of an assumption to accept the calculated geometric Swirl number as the effective Swirl number. Therefore this Swirl number must be derived from the velocity components of the flow field. More specifically, the radial profiles of the axial- and tangential velocity components for at least one axial location inside the mixing tube must be obtained.

So an experiment is required from which the axial velocity component can be obtained for a range of axial locations and the tangential velocity component can be obtained for at least one of these axial locations inside the mixing tube. A non-intrusive experiment is preferred for this measurement as such an experiment would not change the flow field by inserting a probe in the enclosed flow. Delft University of Technology is well equipped with the knowledge, equipment, and experience of Particle Image Velocimetry (PIV). Besides its availability, PIV is an excellent technique to capture a velocity field as discussed in section 2.8 and is therefore adopted as the experimental technique of choice. It will be applied twice: once on a plane coinciding with the central axis through both the mixing tube and combustion chamber and once on a plane perpendicular to the central axis inside the mixing tube. The first plane will be further referred to as 'centre-plane' while the second plane will be further referred to as the 'cross-plane'. The velocity components that can be obtained from the centre-plane are the axial- and radial component. The velocity components obtained from the cross-plane are the tangential- and radial component. It was decided that the Swirl number should be measured just upstream of the dump as this rules out the influence of the mixing tube length in the measurements. Upstream of this location the swirl intensity will be higher as the flow has encountered less friction, but taking the measurement further upstream would neglect that fact.

The study performed by T. Reichel et al.[70] is the only other significant study that deals with axial air injection in swirl-stabilised combustor flows. That study adopted a radial vane swirler in the design. This study also wishes to investigate what differences arise when adopting an axial vane swirl generator in combination with axial air injection compared to a radial swirler. There could potentially be four main advantages associated with this implementation of an axial swirl generator. Firstly, the design can likely become more compact. Second, the effect of axial air injection on the flow field could be rather different as there is no significant velocity component that impinges on the axial air jet. Therefore the effect of AAI on the flow field could be stronger for a combustor with an axial swirl generator compared to a radial swirler. Thirdly, the pressure drop generated over an axial swirler could be smaller compared to a radial swirler. Finally, the mixing quality could potentially be improved with the use of an axial swirler. Therefore this study will make use of both radial- and axial swirl generators.

Reichel's study was also carried out in the framework of the AHEAD project at the TU Berlin. Therefore it is desirable to stay close to the dimensions and parameters that were used in that study. It was decided to keep the following parameters equal or similar to the TU Berlin experiments.

- **Reynolds number** - The Reynolds number (Re) is a dimensionless number indicating the level of turbulence. For the isothermal and some of the reacting experiments this was set to 40,000 in Berlin. As the cold flow experiments conducted in this study should simulate a flow field as close as possible to the reacting hydrogen case, it is sensible to adopt this same Reynolds number. While Re definitely has an influence on the velocity field, the effect on the mixing quality is even greater. As the mixing quality will be investigated in a future study, it makes sense to design the model for the current study with this in mind.
- **Power** - Similarly, the power level generated in the reacting case by T. Reichel at al. is a good indicator of what power the experimental model in this study would generate, were it reacting. The power range investigated at the TU Berlin was from 20 to 220 kW. Even though this is a wide range, it provides a ballpark for the effective power that the combustor model should produce in case of reacting flow.
- **Expansion ratio** - The pressure gradient on the centerline over the sudden expansion ultimately gives rise to the vortex breakdown. This pressure gradient is a function of the area ratio between the combustion chamber and mixing tube. At the TU Berlin the diameter of mixing tube and combustion chamber was 34 and 105 mm respectively. This gives an expansion ratio of just over 3 (w.r.t. the radii).
- **Mixing tube diameter** - Although not crucial, using a similar mixing tube diameter as in the previously conducted experiments, provides for a good initial design condition. With a known mixing tube diameter and Re the air mass flow ($\dot{m}_{air}$) can be obtained. For a given equivalence ratio (ϕ) or air-to-fuel ratio, the fuel flow ($\dot{m}_{fuel}$) can be obtained. This fuel flow is directly related to the power output through the specific heat of the fuel. With a similar mixing tube diameter and expansion ratio the combustion chamber diameter is naturally also given.

Besides these requirements that force the design to be similar to experiments conducted by T. Reichel et al. there is still considerable design freedom. To come to a suitable design that will allow to reach the goals of the experiments, the following requirements were specified.

- **Fluids** - The fluids used for the experiments should be non-hazardous, and easily accessible. Moreover, the mass flow rates of all streams should be controllable with the available mass flow controllers and supply lines of the TU Delft facilities. As the experiments in this study are non-reacting cold flow only, the fluid in the fuel stream does not have to be flammable. Using air in this fuel stream simplifies the experimental setup considerably as it is readily available on supply lines. Furthermore, using air yields far less issues considering health, safety and environment. The swirling air and axial air streams can naturally remain air flows. Another benefit of using air is that the scattering efficiency of particles in gas relative to water is much higher as the refractive index of water is considerably higher. It should be noted that using air in these streams is different to the isothermal experiments conducted in Berlin as water was used in all streams for those experiments. When the same dimensionless numbers and parameters are used, the flow fields are similar in theory. However as mentioned before, a secondary

goal of this setup is also to be applicable to mixing quality investigations. The accuracy of the mixing experiments is higher for gaseous mixing than it is for liquid mixing [44]. Designing the experimental model for gasses instead of water (or another liquid) will allow future research on the mixing quality to easily re-use the model.

- **Momentum flux ratio** - The momentum flux ratio (J) of fuel jets into the air should be kept constant w.r.t. hydrogen fuel jets into air. When air is sent through the fuel injection ports in stead of hydrogen its mass flow has to be adjusted to resemble a hydrogen jet into air. The appropriate metric to keep constant for exchanging fluids is the momentum flux ratio of the fuel jet into the air stream eq. (3.1). Air has a much higher density than hydrogen, so for a constant momentum flux ratio the velocity of the air in the fuel stream should be reduced w.r.t. the velocity that hydrogen would have. When the same geometry fuel ports are used, the velocity can only be reduced by reducing the mass flow of the fuel stream.

$$J = \frac{\rho_{fuel} {u_{fuel}}^2}{\rho_{ox} {u_{ox}}^2} \qquad J_{fuel=air} = J_{fuel=h2} \tag{3.1}$$

- **Mass Flows** - All of the flows should not choke anywhere in the setup downstream of the seeding pots. Choking will cause unwanted pressure gradients and instabilities that should be avoided.

- **Equivalence ratio** - The equivalence ratio should be variable from 0 to 1. This will allow to investigate any equivalence ratio that is relevant for a lean premixed hydrogen burner.

- **Axial Air Injection** - The axial air injection quantity (Ψ) should be variable from 0 to 30% of the total air mass flow. This range is considerably larger than the range that was previously investigated in Berlin ($\Psi = 0\%$, $\Psi = 7.5\%$ and $\Psi = 12.5\%$).

- **Swirl Generator** - The Swirl number (Sw) should be variable and should cover a range of 0.5 to 1.5. It should also be measurable to verify that this swirl intensity is actually reached. This range is considerably larger than the range that was previously investigated in Berlin ($Sw = 0.7$ & $Sw = 0.9$), which was not verified. Furthermore this desired range should be generated by both a radial- and axial swirl generator.

- **Mixing tube length** - The mixing tube should be at least 60 mm long and short enough to avoid auto-ignition in a reacting case. Reichel et al. used mixing tubes of 40 and 60 mm and concluded the longer was better w.r.t. mixing. A longer tube is preferred as this allows for even better mixing and gives the possibility to investigate the flow development inside the mixing tube with greater resolution. On the other hand, a mixing tube that is too long poses the risk of auto-ignition of the mixing gasses. This risk is especially large when the mixing gasses are preheated [9].

- **Combustion chamber length** - The combustion chamber length should be long enough to enclose the vortex breakdown. The bubble vortex breakdown typically extends up to approximately 3 mixing tube diameters [82]. A combustion chamber of this length will introduce another pressure gradient at the exhaust that will likely influence the flow field upstream, inside the combustion chamber. To avoid this, the minimum combustion chamber length should be in the order of approximately 6 mixing tube diameters.

- **Materials** - The mixing tube and combustion chamber should be optically accessible for the laser to illuminate planes inside the tubes and for the cameras to capture the light reflected of seeding particles. Furthermore, all materials used for the production of the combustor model should be durable for indoors use at room temperature and should not be damaged by the seeding particles.

- **Modular design** - The design should be as modular as possible. This is convenient in case a component is damaged or has to be replaced for another reason. As two types of swirl generators are designed, modularity is necessary to quickly interchange the components. Furthermore, a modular design will allow for future studies to be conducted on parts of the design with ease.

3.2. Component Design

This section covers the designs of the individual components, keeping in mind the formulated requirements. The design of the mixing tube and combustion chamber is addressed in section 3.2.1. Section 3.2.2 and section 3.2.3 discuss the designs of the radial- and axial swirl generators respectively. Finally, section 3.2.4 presents the design of the manifolds or flow distributors. Computer-aided design (CAD) models and technical drawings were created for all components using Dassault Systèmes CATIA V5.

3.2.1. Mixing Tube and Combustion Chamber

The mixing tube (MT) and combustion chamber require optic accessibility from multiple angles. Plexiglass or acrylic was determined to be the most suitable material for these components. An off-the-shelve solution was preferred. An external supplier had tubes available with an inside diameters of 36 mm and 104 mm with a wall thickness of 2 mm and 3 mm respectively. These dimensions were used for the design as they meet the requirements. The length of the mixing tube was chosen to be 100 mm. This relatively long tube provides thorough mixing and allows for the investigation of the swirl intensity degradation over the axial distance of the mixing tube. The combustion chamber length was set to 200 mm. The decision was made to keep the combustion chamber relatively short so that a high magnification of the cross-plane inside mixing tube remains relatively simple. A 150 mm extension tube was also designed to elongate the combustion chamber for the centre-plane measurements. This extension ensures that there is no unwanted backflow or other upstream effects that influence the vortex breakdown.

Acrylic flanges of thickness 2 mm were added on both sides of the mixing tube and on the upstream side of the combustion chamber. The flanges were glued to their respective tubes. The two flanges on the interface between MT and combustor can be connected with M5 bolts. This ensures the modularity of the design. The flange on the upstream side of the mixing tube is designed such that it can be connected to both the radial swirler and axial swirler module. This allows the MT-combustor module to be used for all configurations of the setup. Technical drawings of the tubes are presented in fig. 3.1 and fig. 3.2.

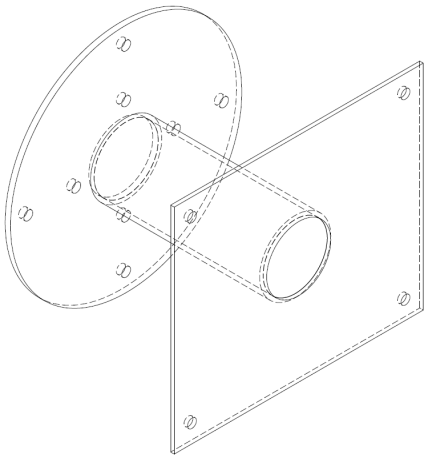

Figure 3.1: Technical isometric drawing of the mixing tube

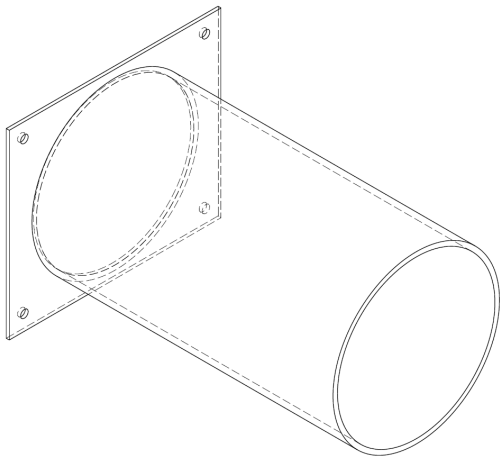

Figure 3.2: Technical isometric drawing of the combustion chamber

3.2.2. Radial Swirl Generators

Radial swirl generators deflect radially injected air, giving it a tangential component section 2.5.3. For the design of the radial swirlers two concepts were possible: the fixed vane swirler fig. 2.8 and the movable block swirler fig. 2.9. As a range of swirl numbers should be generated the movable block swirl number seems like the preferred option. However this configuration was disregarded because the uncertainty of the experiment is larger. The movable block has to be manually rotated and set to the desired swirl intensity. The accuracy and repeatability of this setting are both compromised. Furthermore the movable block-configuration is much more prone too leaks than a fixed vane swirler. Therefore the swirl range has to be covered by exchanging multiple fixed van radial swirlers.

It was decided that six different swirlers were to be designed and produced to cover the geometric Swirl number range of 0.5 to 1.5 with an increment of 0.2 per swirler. From eq. (2.12) it can be observed that the geometric Swirl number is inversely proportional to the length of the vanes (L_{slot}); shorter vanes generate a higher swirl intensity. The other variables affecting the Swirl number are the exit radius, which is governed by the mixing tube (R_{MT} = 18 mm), and the dimensionless geometric parameter σ. This parameter is dependent on the vane angle, vane thickness and the number of vanes. It was decided to keep sigma constant and to thus to make the vane length the sole variable responsible for the change in swirl number. A total number of 16 vanes was chosen to have a well distributed swirl air inlet while the exit plane geometry is axisymmetric. A reasonable vane thickness of 3 mm was chosen to provide some structural integrity. The vane angle was set to 47.05°. This results in a nicely rounded vane length from 30.0 mm for Sw = 0.5 and 10.0 mm for Sw = 1.5. The relevant dimensions of the six swirlers are presented in table 3.1.

Table 3.1: Relevant dimensions of the radial swirl generators

Swirler ID	Sw_{Geo} [-]	No. vanes [-]	Vane thickness [mm]	TE vane angle [deg]	Vane length [mm]
R_SW15	1.5	16	3.0	47.05	10.00
R_SW13	1.3	16	3.0	47.05	11.54
R_SW11	1.1	16	3.0	47.05	13.64
R_SW09	0.9	16	3.0	47.05	16.67
R_SW07	0.7	16	3.0	47.05	21.43
R_SW05	0.5	16	3.0	47.05	30.00

Upstream of the swirler is the fuel distribution chamber. Four M4 holes are tapped into the upstream edge of swirler to be able to connect to the fuel chamber. Fuel is injected through 16 1.6 mm holes evenly distributed at 14 mm from the centreline. The axial air injector is also integrated into the swirler design. A 100 mm long tube with inner diameter 10 mm runs along the centreline and exits at the plane with the fuel port exhausts and the upstream edges of the radial vanes. The AAI tube inlet is tapered off slightly to make it easier to connect the supply line of the AAI. The tube is 10 diameters long and the flow through it is turbulent. Therefore it is a valid assumption that the flow exiting the AAI tube is fully developed [17]. A flange is connected to the downstream end of the swirler. The holes in this flange align with the outer holes of the upstream flange of the mixing tube and fit M5 bolts. All six swirlers are printed with an Ultimaker S5 using PLA filament. Technical drawings of the radial swirl generator design are presented in fig. 3.3. The isometric views of the two extreme cases are compared in fig. 3.4.

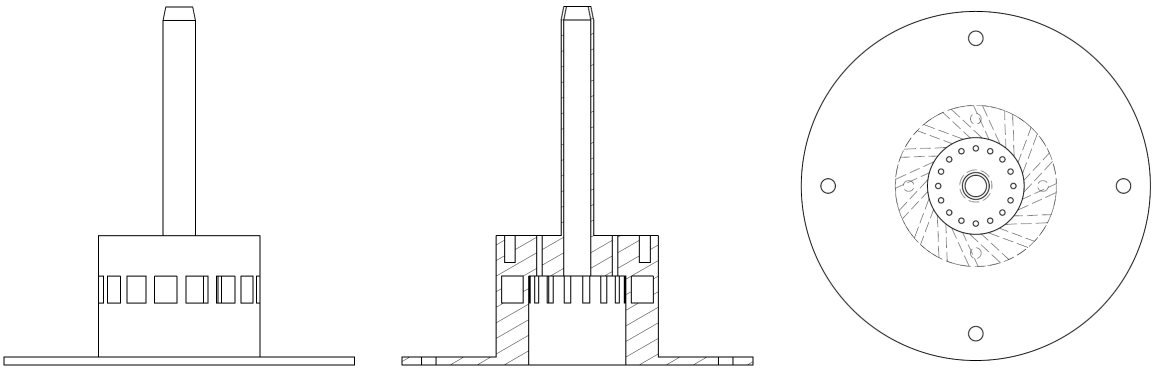

(a) Side view (b) Section view (c) Bottom view

Figure 3.3: Technical drawings of radial swirl generator Sw=1.5

It should be noted that in previous experiments by T.Reichel et al. fig. 2.22 the vane length itself was not varied for the cases with a geometric swirl number 0.7 and 0.9. An effective reduction in vane length was attempted by installing a blocking ring of specified dimension over the radial slot inlets. While this obstruction does effectively decrease the length of the vanes (and thus the slots) at the inlets, the flow is free to expand to the full slot length downstream of the inlet. The length of the slots at the exit is thus not reduced. Therefore this method likely has a smaller effect on changing the Swirl number than intended. For this reason,

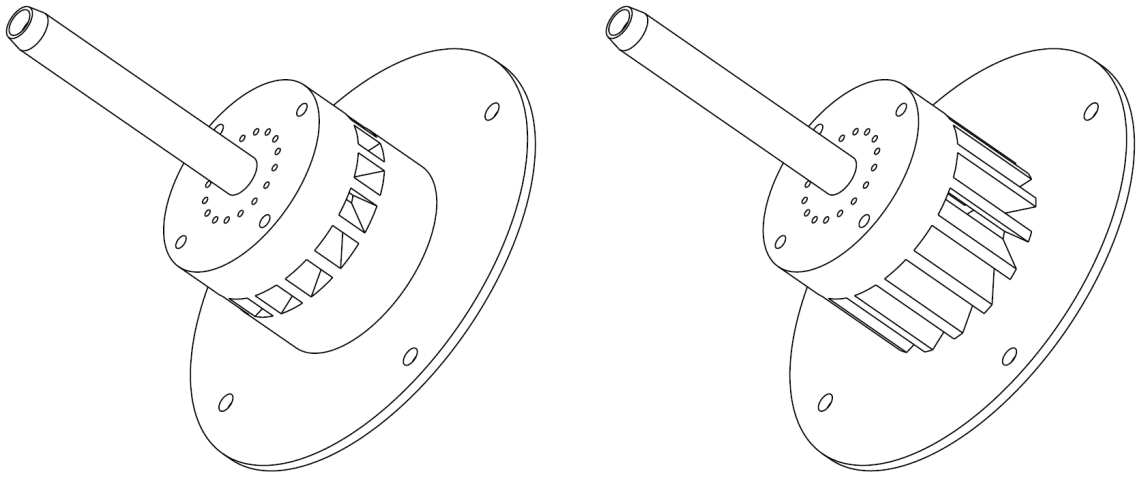

(a) Geometric Swirl number = 1.5 (R_SW15) (b) Geometric Swirl number = 0.5 (R_SW05)

Figure 3.4: Technical isometric drawings of radial swirl generators R_SW15 (a) and R_SW05 (b)

interchanging swirlers with physically different vane lengths is the preferred design method.

3.2.3. Axial Swirl Generators

Different to radial swirl generators, axial swirlers deflect air in tangential direction from an initially predominant axial velocity component. The decision was made to adopt helical vanes with increasing vane angle φ along the axial and radial direction in stead of straight vanes. This curved blade design is a better aerodynamic design as it reduces the risk of wall separation [65] and reduces vane passage wall wake effects [6].

The outer radius R_n was set to 18 mm to ensure a flush transition from the swirler to the mixing tube. The hub radius R_h was governed by the axial air injection tube, which runs along the centreline with outer radius 6 mm. The number of vanes was set to 8 and the vane thickness was set to 2 mm. The tip angle at the trailing edge (TE) of the vane (φ_0) was the only variable changed to obtain different geometric swirl numbers. This geometric Swirl number for the helical vane swirler was calculated using eq. (2.18). The dimensions of the resulting six geometries are presented in table 3.2.

Table 3.2: Relevant dimensions of the axial swirl generators

Swirler ID	Sw_{Geo} [-]	No. vanes [-]	Vane thickness [mm]	TE tip vane angle [deg]
A_SW15	1.5	8	2	60.90
A_SW13	1.3	8	2	58.07
A_SW11	1.1	8	2	54.45
A_SW09	0.9	8	2	49.68
A_SW07	0.7	8	2	43.28
A_SW05	0.5	8	2	34.55

On the downstream side of the swirler (on the same plane as the TE of the vanes) is a flange connecting to the fuel injector via four sets of M5 bolts and nuts. The swirlers including the AAI tube and downstream flange are 3D printed using the same PLA filament as the radial swirlers. Six identical flanges were printed separately and mounted on the planes coinciding with the upstream edge of the vanes with adhesive. This upstream flange connects to the swirl air distribution chamber. The holes of the upstream flanges were aligned with the downstream flange holes. This allowed the swirl air distribution chamber, swirl generator, fuel injector, and mixing tube to be connected with four long M5 bolts, running the entire length of the components. This configuration ensured the bending load of the horizontally mounted setup was carried by the bolts and not the PLA. Technical isometric drawings of the the axial swirler excluding and including upstream flange are presented in fig. 3.5a and fig. 3.5b respectively.

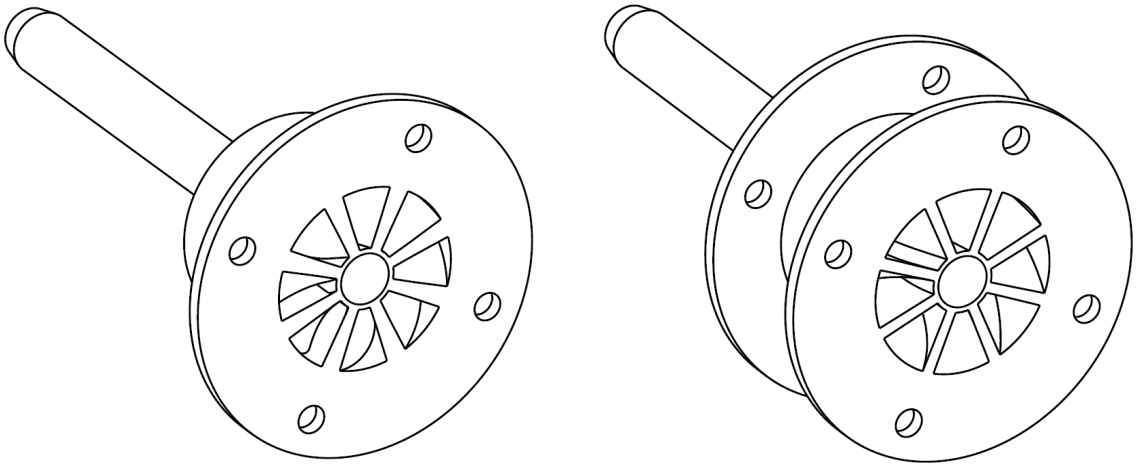

(a) Geometric Swirl number = 1.5 (A_SW15) (without upstream flange)

(b) Geometric Swirl number = 0.5 (A_SW05) (with upstream flange)

Figure 3.5: Technical isometric drawings of axial swirl generators A_SW15 (a) and A_SW05 (b)

3.2.4. Manifolds

Four different manifolds were designed in total: a fuel injector and swirl air injector for both axial and radial swirl generators. As mentioned in section 3.2.3 the axial swirler configuration is equipped with a fuel injector downstream of the swirler. This was designed as a 36 mm inner diameter and 70 mm outer diameter pipe. Four equidistant chamfered edges were introduced on the pipe's outer wall. A threaded hole was added on each edge. Fuel is injected radially inwards into these holes through hose pillars, which can connect to four air supply hoses. The length of the manifold is 30 mm to ensure equal length of the exit of the AAI tube to the entrance of the mixing tube for both configurations. Four holes were drilled through the thick walls in axial direction and align with the holes of the axial swirler and the swirl air injector.

The swirl air injector has a very similar configuration with only two differences compared to the fuel injector. A wall was added on the upstream side, which has a hole just large enough for the AAI tube to fit through. In assembled formation this hole was sealed with sealing tape. The manifold was also elongated to 60 mm to give the injected air more space to settle before reaching the swirl generator vanes. Technical isometric drawings of the two manifolds for the axial swirler configuration are presented in fig. 3.6.

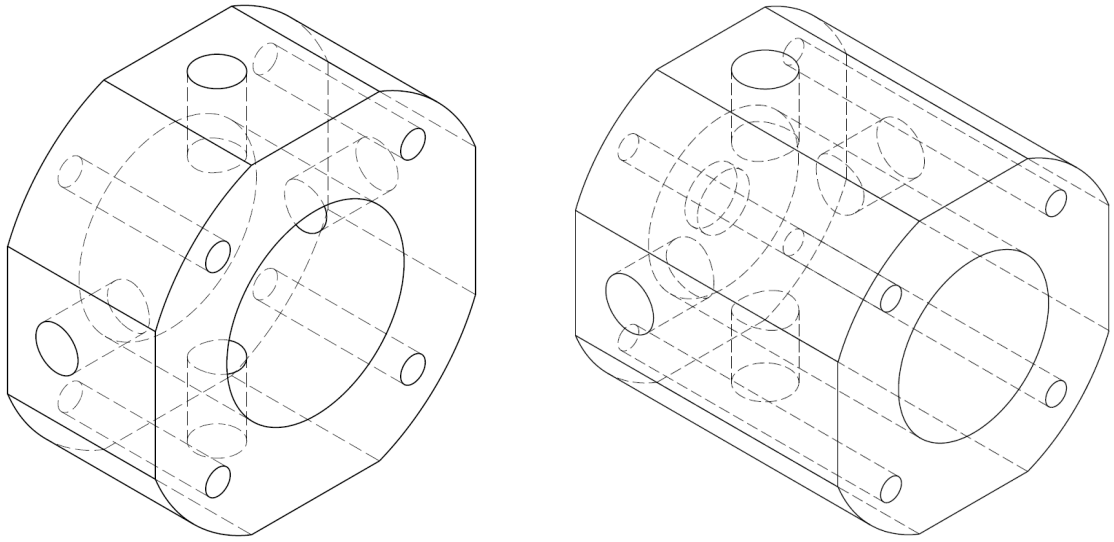

(a) Fuel injector

(b) Swirl air injector

Figure 3.6: Technical isometric drawings of the axial swirler module manifolds: fuel injector (a) and swirl air injector (b) (not to scale)

The fuel injector for the radial swirler configuration is likewise very similar to the two manifolds for the axial swirler configuration. The fuel injector is upstream of the radial swirl generator. Just like the swirl air injector for the axial swirler module. an end wall was fitted on the upstream edge with a smaller hole for the AAI tube to fit through. The for holes in axial direction were relocated and reduced to M4 size to fit onto the radial swirl generators.

The swirl air injector for the radial swirl generator was designed to fit over the radial swirler. The swirl generator has 16 vanes. To ensure a decently uniform distribution, an air injection hole was positioned in line with every second vane. This was realised through a large ring with an octagonal outer wall and cylindrical inner wall. Four axial holes are introduced through the wall to connect to the swirler flange and mixing tube downstream and an adapter ring upstream. This adapter ring functions as a flange, connecting the upstream face of the swirler to the swirl air injector. Technical isometric drawings of the two manifolds for the radial swirler configuration are presented in fig. 3.7. All manifolds and the adapter ring were machined out of aluminium by staff members from TU Delft's DEMO and the High Speed Laboratory of the aerospace faculty.

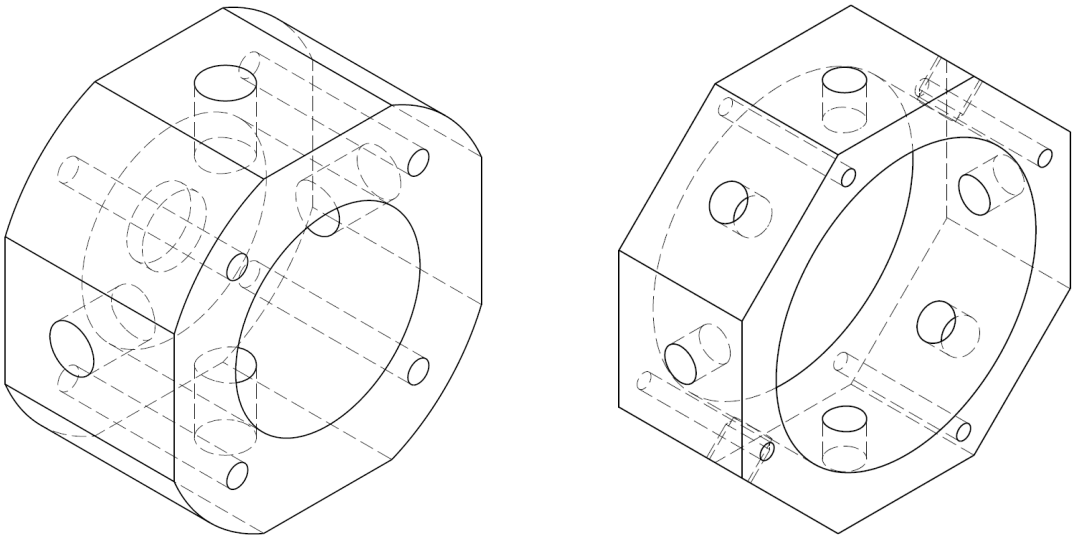

(a) Fuel injector (b) Swirl air injector

Figure 3.7: Technical isometric drawings of the radial swirler module manifolds: fuel injector (a) and swirl air injector (b) (not to scale)

Technical isometric drawings of the two swirler modules including manifolds are presented in fig. 3.8 and fig. 3.9. A side profile and section view of the two configurations including mixing tube and combustion chamber are presented in fig. 3.10 and fig. 3.11. Technical drawings of all plexiglass and aluminum components are presented in appendix A.

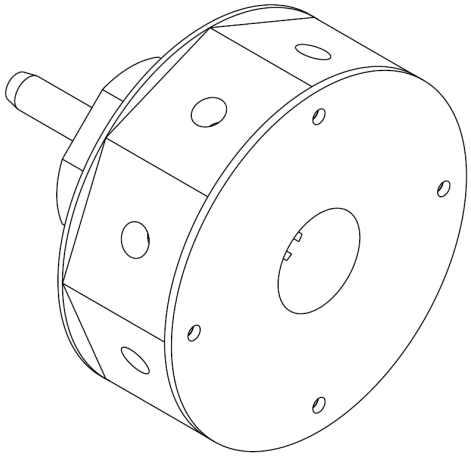

Figure 3.8: Technical isometric drawing of the radial swirler module

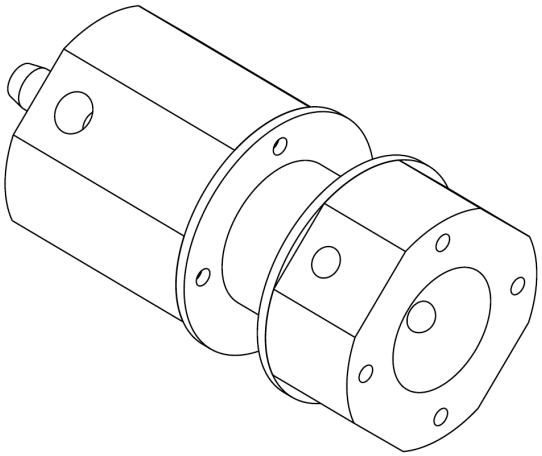

Figure 3.9: Technical isometric drawing of the axial swirler module

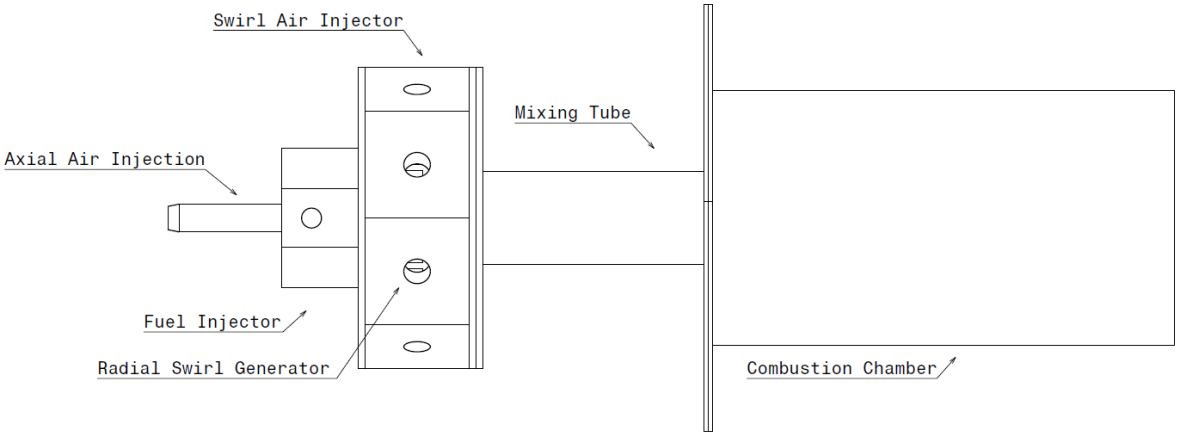

(a) Side view

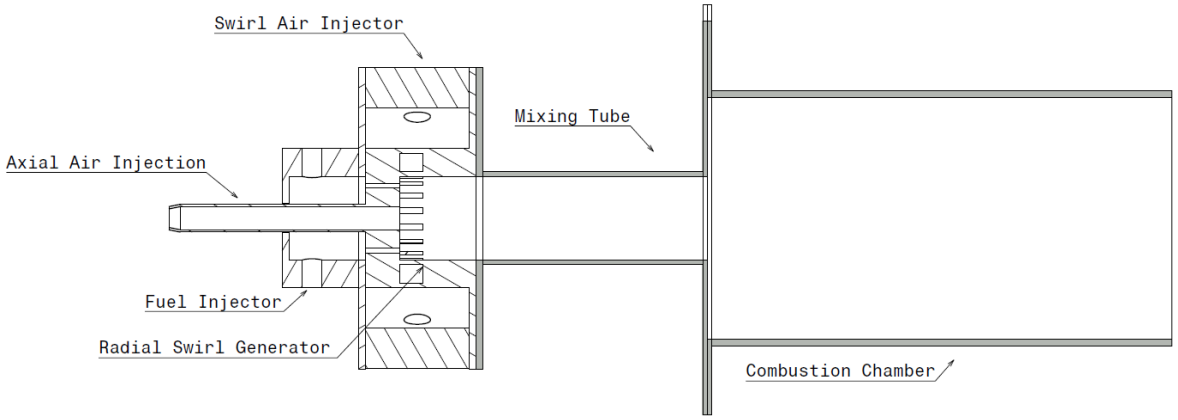

(b) Section view

Figure 3.10: Technical drawings of the radial swirler combustor model with axial air injection

3.3. Mass Flows Rates

With the dimensions of the components fixed the mass flows rates of the three streams can be set. To achieve a Reynolds number of 40,000 in the mixing tube, an air mass flow rate of 0.020 kg/s or 994 $nlpm$ is required, following eq. (3.2) and eq. (3.3). This total air mass flow excludes the fuel flow. The AAI fraction (Ψ) thus gives the mass fraction (or volume fraction since densities are equal) of the AAI to the total air mass flow. The mass- and volume flow rates for the different Ψ settings is given in table 3.3. Note that originally, the plan for the

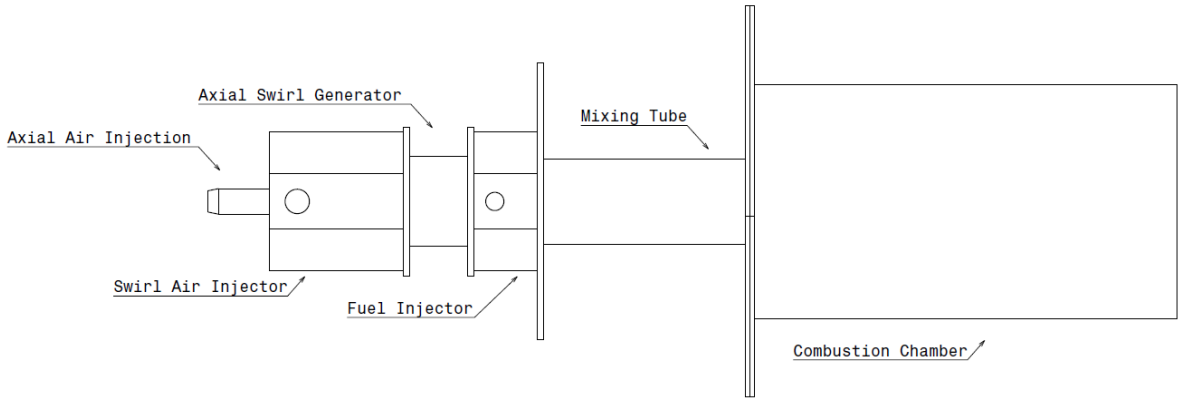

(a) Side view

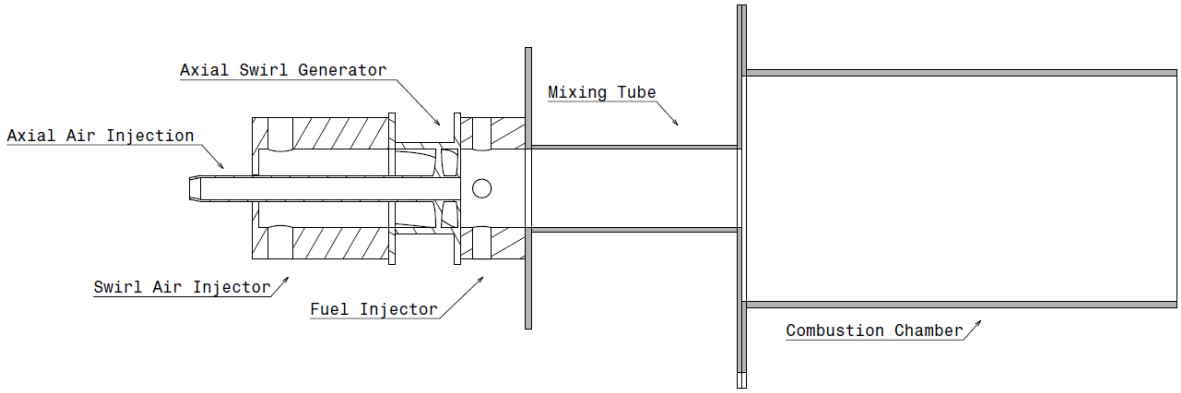

(b) Section view

Figure 3.11: Technical drawings of the axial swirler combustor model with axial air injection

experimental campaign was to vary Ψ from zero to 25% in steps of 5%. However, this range was extended and locally refined for some cases based on initial results form these experiments.

$$v_{air} = \frac{Re_{MT}\,\mu_{air}}{D_{MT}\,\rho_{air}} \tag{3.2}$$

$$\dot{m}_{air} = v_{air}\,A_{MT}\,\rho_{air} \tag{3.3}$$

Table 3.3: Air flow rates at different settings of the AAI fraction

Ψ [-]	$\dot{m}_{swirl\,air}\ [kg/s]$	$\dot{V}_{swirl\,air}\ [nlpm]$	$\dot{m}_{AAI}\ [kg/s]$	$\dot{V}_{AAI}\ [nlpm]$
0	0.0203	994	0	0
0.025	0.0198	969	0.00051	24.8
0.05	0.0193	944	0.00102	49.7
0.075	0.0188	919	0.00152	74.5
0.1	0.0183	894	0.00203	99.4
0.15	0.0173	845	0.00305	149.0
0.2	0.0162	795	0.00406	198.7
0.25	0.0152	745	0.00508	248.4
0.3	0.0142	696	0.00609	298.1
0.35	0.0132	646	0.00711	347.8
0.4	0.0122	596	0.00812	397.4

Similar to the air streams, the fluid in the fuel stream is also air at room temperature in stead of hydrogen. To keep the momentum flux ratio constant between the two scenarios, the momentum flux ratio of the hydrogen case must first be determined from the densities and velocities of the hydrogen fuel and air eq. (3.1). The hydrogen velocity eq. (3.5) is obtained through the stoichiometric air-to-fuel ratio of hydrogen using the chemical equilibrium in eq. (3.4). The velocity of the hydrogen fuel is calculated using the mass flow eq. (3.5)

in eq. (3.6), where A_{fp} represents the flow through area of the fuel ports. The product of the density and squared fuel velocity yields the momentum flux of the hydrogen fuel. The momentum flux of the cold air in this study should be equal to that momentum flux. The velocity and mass flow rate of the air injected through the fuel ports is calculated using eq. (3.7) and eq. (3.8) respectively.

$$2\,H_2 + 4.762\,(0.21\,O_2 + 0.79\,N_2) \longrightarrow 2\,H_2O + 3.762\,N_2$$
$$AFR_{stoich} = \frac{4.762\left(0.21\,Mw_{O_2} + 0.79\,Mw_{N_2}\right)}{Mw_{H_2}} \tag{3.4}$$

$$\dot{m}_{fuel,H_2} = \frac{\dot{m}_{air}}{AFR_{stoich}}\varphi \tag{3.5}$$

$$v_{fuel,H_2} = \frac{\dot{m}_{fuel,H_2}}{A_{fp}\,\rho_{H_2}} \tag{3.6}$$

$$v_{fuel,air} = \sqrt{\left(v_{fuel,H_2}\right)^2 \frac{\rho_{H_2}}{\rho_{air}}} \tag{3.7}$$

$$\dot{m}_{fuel,air} = v_{fuel,air}\,A_{fuelports}\,\rho_{air} \tag{3.8}$$

In equation eq. (3.5) φ represents the equivalence ratio, which is varied from 0 to 1. Computing these equations for that range gives the air mass flow rate through the fuel ports for different conditions. It was decided to use a fixed (effective) equivalence ratio of 0.6 for most setpoints. This represents a completely reasonable scenario for lean premixed hydrogen combustion. For several cases the fuel flow will be reduced to zero and increased to the stoichiometric condition, where $\varphi = 1$, to investigate the effect of fuel momentum on the flow field. These fuel flow setpoints are presented in table 3.4.

Table 3.4: Fuel flow rates at different settings of effective equivalence ratio

φ [-]	$\dot{m}_{fuel,air}$ $[kg/s]$	$\dot{V}_{fuel,air}$ $[nlpm]$
0	0	0
0.6	0.00136	66.3
1.0	0.00226	110.6

4

Methodology: Numerical Simulations

Numerical simulations are often a much more accessible and cheaper way to perform engineering studies compared to experimental work. In the field of fluid dynamics, computational fluid dynamics (CFD) can provide a very helpful insight into, and make prediction of, the actual flow field. These predictions can guide design decisions to improve the final design. For this study CFD, in the form of steady-state Reynolds Averaged Navier Stokes (RANS), was thus employed to check and guide the designs of the swirl generators and the feature of axial air injection. This chapter will discuss the methodology of the numerical simulations performed in the form of CFD. These simulations were carried out using different software packages from ANSYS 19.2. The first section (section 4.1) reviews the meshing of the domains. This is followed by the pre-processing in section 4.2 and the solving of the simulations in section 4.3. Finally, the post-processing is discussed in section 4.4.

4.1. Meshing

The first step in any CFD analysis is the generation of a mesh for the domain and that is to be investigated. The domain is derived from the combustor model geometry (see chapter 3). For this study it was decided to have the domain cover all the volumes where fluid would flow from all the air inlets into the combustor model (including manifolds) up to the combustor exhaust. This domain was divided up into multiple segments or subdomains: eight for the radial swirler combustor model and six for the axial swirler combustor model. A structured mesh (usually O-grid) was then created for each subdomain using ANSYS ICEM CFD. The total number of nodes that could be solved in ANSYS was limited to 512,000 for this study. The following subsections will present and briefly discuss the meshing of the most relevant subdomains.

4.1.1. Combustor Module

For both axial- and radial swirl generators the combustor module (mixing tube and combustion chamber) are identical. The geometry of this module was governed by the inner diameters of the two tubes. A hexahedral mesh was iteratively created for this subdomain with a final total number of 175,572 nodes. The iterations were made to change the number of nodes and to improve the quality of the mesh. As the full radial swirler combustor model domain is larger in volume and is more complex, this domain required more cells than the axial swirler combustor model. In fact, the mesh of the combustor module for the radial swirler had to be scaled down slightly (to 148,340 nodes) in order to stay under the 512,000 cell limit. For both the minimum spacing stayed identical with 0.1 mm at the mixing tube wall and an expansion ratio of 1.2. This small spacing was applied to properly resolve the boundary layer of the mixing tube.

CFD has issues solving if the flow at the outlet is recirculating. Therefore, to ensure no backflow occurs at the combustor exit, a course exhaust mesh was created. This mesh was equal in diameter to actual combustor, and practically extends the tube by 200 mm. Its refinement is not critical so only 7,280 nodes were used for this exhaust mesh. The combined meshes are presented in fig. 4.1. The quality and other important metrics of the meshes are given in table 4.1. From this table it is clear that the mesh quality was not harmed by scaling down slightly for the radial swirler geometry.

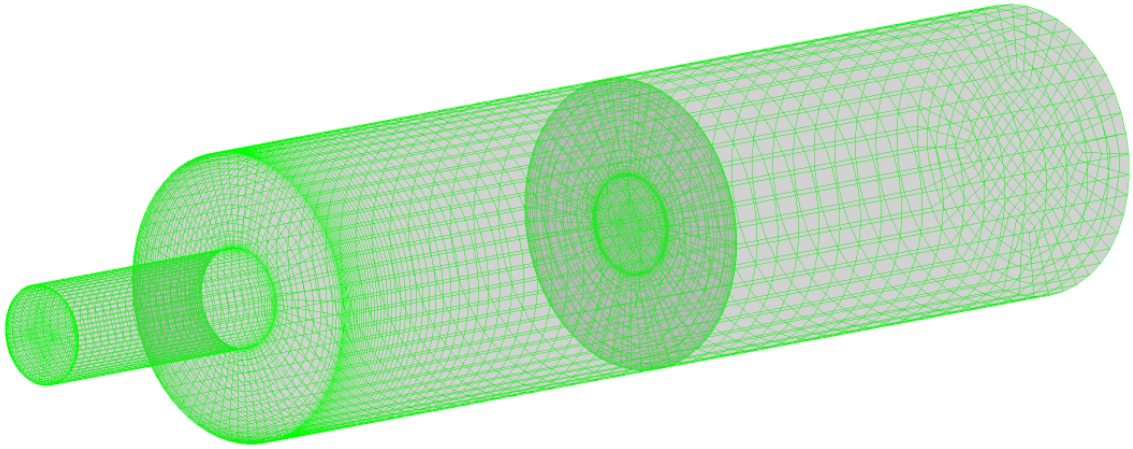

Figure 4.1: Combustor module mesh

Table 4.1: Mesh quality of combustor module subdomains

Mesh	Nodes [-]	Mean quality [-]	Min. quality [-]	Angle [deg]	AR [-]	Skewness [-]
Combustor module (R)	148,340	0.933	0.713	48.6	140	0.834
Combustor module (A)	175,572	0.938	0.718	48.4	132	0.831
Exhaust	7,280	0.883	0.635	49.7	3.02	0.879

4.1.2. Radial Swirl Generator

The radial swirl generator was divided into three subdomains: The swirling air injector, the radial/tangential vane passages, and the swirler core. The swirling air injector contains the eight air injection nozzles and is equal for all radial swirler geometries. The vane passages are of different length for each geometric Swirl number, but the six different (H-grid) meshes each have very similar quality. The core is also identical for each radial swirler geometry. This is the domain that connects to both the AAI tube and fuel ports upstream and to the mixing tube downstream. The individual mesh characteristics of the radial swirl generator are given in table 4.2. The mesh with geometric Swirl number 0.9 is illustrated in fig. 4.2.

Table 4.2: Mesh quality of the radial swirl generator subdomains

Mesh	Nodes [-]	Mean quality [-]	Min. quality [-]	Angle [deg]	AR [-]	Skewness [-]
Swirl air inj.	100,480	0.924	0.506	30.42	15.7	0.614
Swirler vanes	126,720	0.855	0.561	34.11	17.4	0.551
Swirler core	51,800	0.920	0.742	47.88	11.1	0.805

4.1.3. Radial Swirler Fuel Injector

The fuel distribution and injection happens upstream of the radial swirl generator. This fuel path was separated in two segments to simplify the meshing of the domain. The first part is the fuel injection manifold, which is an annular mesh that contains the four air injection nozzles. The centre of the manifold is not part of the domain as this is where the AAI tube is positioned. The second part of the fuel injector is the sixteen fuel ports, which run inside the structure of the radial swirl generator in axial direction. The merged mesh is shown in fig. 4.3 and the quality of the meshes is presented in table 4.3.

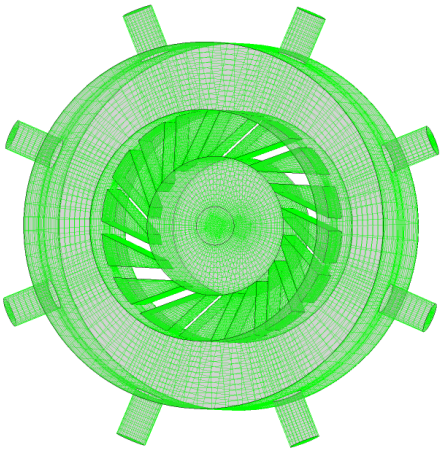

Figure 4.2: Radial swirl generator mesh

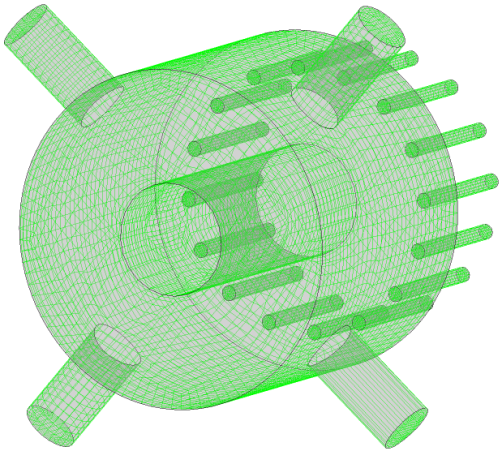

Figure 4.3: Radial swirler fuel injector mesh

Table 4.3: Mesh quality of the radial swirler fuel injector subdomains

Mesh	Nodes [-]	Mean quality [-]	Min. quality [-]	Angle [deg]	AR [-]	Skewness [-]
Fuel inj.	51,760	0.862	0.525	30.42	11	0.423
Fuel ports	17,520	0.782	0.514	53.37	8.99	0.962

4.1.4. Axial Swirl Generator

The axial swirl generator was meshed as eight curved vane passages using H-mesh topology. Although the topology is equal for all geometric swirl numbers, the geometry is quite different. The tip angle of the vanes is much larger for the $Sw = 1.5$ swirler than for the swirler with $Sw = 0.5$. This causes the cell skewness and minimum angle to be strongly affected and the overall quality to decrease for the higher Swirl number cases. The mesh qualities of the extreme axial swirl generators are presented in table 4.4. The mesh of the geometry with highest Swirl number is displayed in fig. 4.4.

Table 4.4: Mesh quality of the axial swirl generators

Mesh	Nodes [-]	Mean quality [-]	Min. quality [-]	Angle [deg]	AR [-]	Skewness [-]
A_SW15 vanes	96,000	0.855	0.458	27.3	46.5	0.465
A_SW05 vanes	96,000	0.915	0.823	55.4	32.8	0.822

4.1.5. Axial Swirl Generator Manifolds

The swirling air manifold and fuel manifold are very similar for the axial swirl generator. Both are also closely related to the radial swirler fuel manifold, especially the the axial swirling air manifold since both have the AAI tube running through the centre. Since the meshes are so similar their qualities are likewise analogous as shown in table 4.5. The axial swirler fuel injector mesh is presented in fig. 4.5.

Table 4.5: Mesh quality of the axial swirl generator manifolds

Mesh	Nodes [-]	Mean quality [-]	Min. quality [-]	Angle [deg]	AR [-]	Skewness [-]
Swirl air inj.	77,152	0.876	0.504	24.8	5.43	0.474
Fuel inj.	64,320	0.851	0.526	31.7	5.42	0.571

4.1.6. Axial Air Injection Tube

The tube that provides the axial air injection is identical for both radial- and axial swirl generator modules. It is a relatively small geometry and straightforward geometry: a long narrow tube with a slightly tapered upstream end. The mesh characteristics are listed in table 4.6. The cells with the relatively low minimum quality

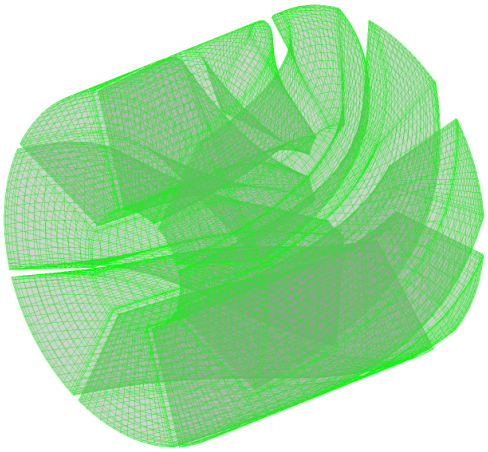

Figure 4.4: Axial swirl generator mesh (Sw=1.5)

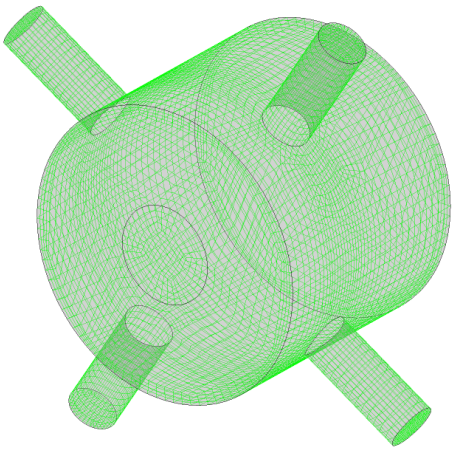

Figure 4.5: Axial swirler fuel injector mesh

are in the tapered end. The cells in the remainder of the tube, especially in the boundary layer, are of high quality.

Table 4.6: Mesh quality of the axial swirl generator manifolds

Mesh	Nodes [-]	Mean quality [-]	Min. quality [-]	Angle [deg]	AR [-]	Skewness [-]
AAI Tube	4,628	0.807	0.466	51.2	6.26	0.944

4.1.7. Combined Meshes

Adding all meshes of the subdomains together for the two swirler geometries gives an overview of the total meshes and their qualities. The full meshes of the combustor models with radial- and axial swirl generators are presented in fig. 4.6 and fig. 4.7 respectively. From table 4.7 can be observed that despite the significantly different geometries, the total mean mesh qualities are nearly identical. The mesh of the radial swirler combustor model, which stays just below 512,000 cells, has its minimum quality cells in the first millimeters of the AAI tube, far away from the region of interest. For the axial swirler these worst cells are at the tip of the swirler vanes. It is also these cells that bear the largest skewness (value closest to zero). It was already shown in section 4.1.4 that the quality of these cells is highly dependent on the geometric swirl number. For future studies the mesh of these vanes could be further refined to reduce any error. For both models, the maximum cell aspect ratio (AR) is found at the exit of the combustion chamber. The aspect ratio can typically go up to much higher values (over 10,000), especially in the boundary layer, without any solver issues [88]. So based on the mesh qualities there was no reason to expect any significant errors or issues during solving, albeit the meshes could be somewhat finer to improve accuracy.

Table 4.7: Mesh quality of the axial swirl generator manifolds

Mesh	Nodes [-]	Mean quality [-]	Min. quality [-]	Angle [deg]	AR [-]	Skewness [-]
Radial total	508,528	0.897	0.466	30.4	140	0.423
Axial total (Sw=1.5)	424,952	0.892	0.458	24.8	132	0.465

4.2. Pre-Processing

Once the geometry is specified in the form of a mesh, the next step in CFD simulations is to define the domain and the fluid inside it in pre-processing. This was achieved by establishing the boundary conditions (BCs) (see section 4.2.2) and choosing the appropriate fluid models (see section 4.2.3). However, first the subdomains must be merged using domain interfaces, which is described in section 4.2.1 All of these pre-processing operations are performed in CFX-Pre.

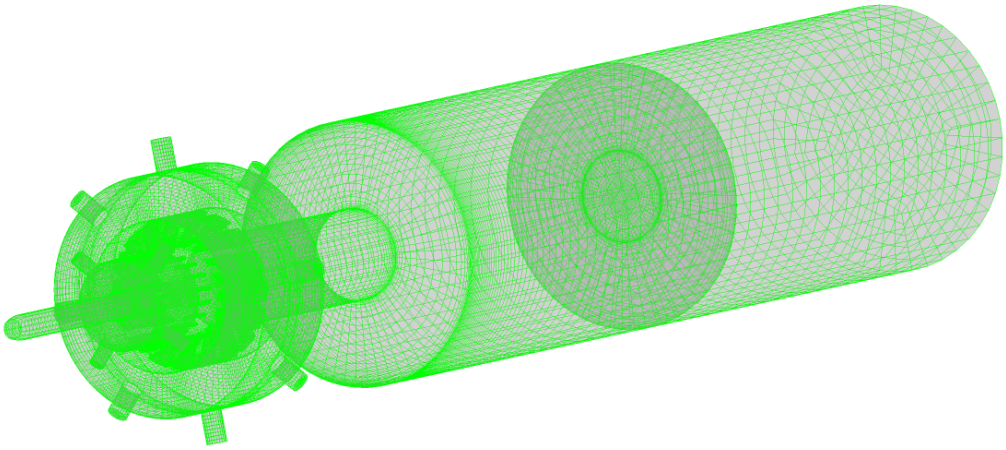

Figure 4.6: Radial swirler combustor model mesh

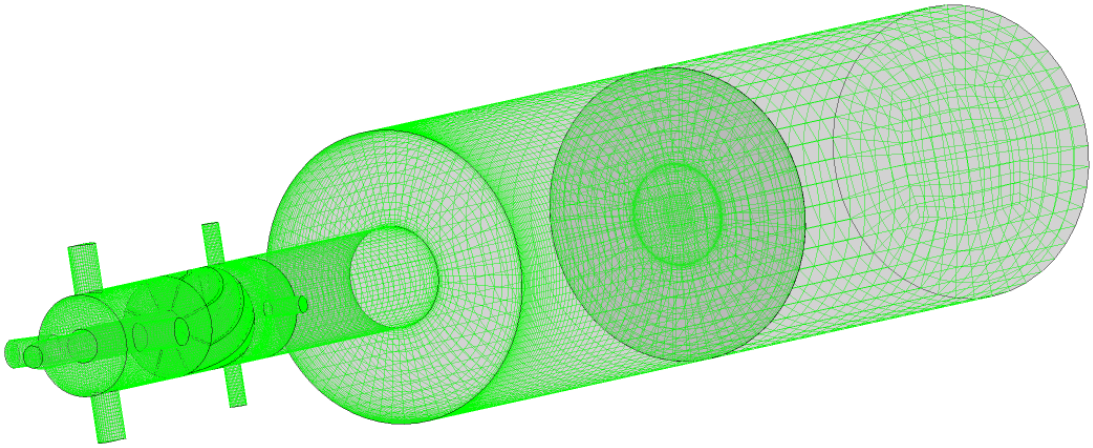

Figure 4.7: Axial swirler combustor model mesh

4.2.1. Domain Definition

The created meshes of the subdomains have to be connected properly to be able to solve the entire domain. As mentioned before the radial swirler model consists of eight subdomains whereas the axial swirler model has six. Therefore the radial models require seven domain interfaces and the axial model requires five. The areas of the interfacing surfaces generally match perfectly, with the only exceptions the upstream and downstream faces of the radial swirler fuel ports. However the location of the nodes do not match perfectly on any of the interfaces. This is not a problem as general grid interface (GGI) connections were be used. The mutually overlapping surfaces of an interface are then automatically connected using GGI connections. The conservative interface flux model is used to match the mass and momentum fluxes on each side of the interfaces. All interface types are set to general Fluid-Fluid connections. The created domain interfaces for the radial swirler combustor model and axial swirler combustor model are listed in table 4.8 and table 4.9.

4.2.2. Boundary Conditions

There are three main boundary condition types (besides domain interfaces, which could also be categorised as BCs) that must be specified to characterize the domain. These are inlet-, outlet-, and wall boundary conditions.

For the combustor model there were multiple locations where inlet boundary conditions needed to be specified. This model has three different inlets for both the radial swirler and axial swirler configuration: swirl air inlet, axial air inlet, and fuel inlet. All three inlets were specified using the mass flow rates as determined in

Table 4.8: Radial swirler model domain interfaces

Domain interface ID	Interface side 1	Interface side 2
DI_R1	AAI tube outlet	Swirler core inner inlet
DI_R2	Fuel injector outlet	Fuel ports inlet
DI_R3	Fuel ports outlet	Swirler core outer inlet
DI_R4	Swirl air injector outlet	Swirler vane passages inlet
DI_R5	Swirler vane passages outlet	Swirler core radial inlet
DI_R6	Swirler core outlet	Combustor module inlet
DI_R7	Combustor module outlet	Exhaust inlet

Table 4.9: Axial swirler model domain interfaces

Domain interface ID	Interface side 1	Interface side 2
DI_A1	Swirl air injector outlet	Swirler vane passages inlet
DI_A2	Swirler vane passages outlet	Fuel injector outer inlet
DI_A3	AAI tube outlet	Fuel injector inner inlet
DI_A4	Fuel injector outlet	Combustor module inlet
DI_A5	Combustor module outlet	Exhaust inlet

section 3.3. For both air inlets the mass flow rates for these inlet BCs were taken from table 3.3, given the setpoint to be simulated. The mass flow rate for the fuel inlet boundary condition was fixed to $1.36\text{x}10^{-3}\ kg/s$, representing an effective equivalence ratio of 0.6 for all investigated setpoints. For the two different swirler configurations all six geometric swirl numbers were considered from zero up to $\Psi = 25\%$ in steps of 5%. This resulted in a total of 2x6x6 = 72 setpoints to be investigated.

The outlet boundary condition was more straightforward as it was identical for each of the twelve full meshes. This outlet BC was obviously specified on the combustor exhaust outlet plane. The condition was specified as an average static pressure of $101,325\ Pa$ (atmospheric) over the surface.

Finally, the wall boundary condition was applied to all other domain surfaces. They were specified to be no-slip walls. This condition most accurately simulates viscous flows such as being investigated in this study. Furthermore all walls were assumed smooth. For the walls inside the plexiglass and aluminium components that assumption is likely valid. However, some error may be introduced with this assumption over the walls of the 3D printed components. On the other hand, during the pre-processing phase of the CFD investigation no parts were produced yet, making it harder to set the actual wall roughness.

4.2.3. Fluid Models

The fluid models are the final domain characteristics to be set. The entire domain was defined as containing air at room temperature and atmospheric pressure. No temperature change was expected so the heat transfer models was disabled (set to isothermal). Buoyancy also plays a negligible role and was therefore disabled.

The turbulence model defines how the unclosed Reynolds stress tensor (turbulence term) in the RANS equations is approximated [16]. The most widely used models are two-equation models that model the turbulence kinetic energy (k) and the specific turbulence dissipation rate (ω) or k and the turbulence dissipation rate (ϵ). The $k-\omega$ model works particularly well in the near wall region of viscous flows and is therefore suited for internal flows. However it tends to be sensitive to inlet free stream turbulence properties. In these free stream locations the $k-\epsilon$ model is therefore preferred. A combination of these two models is the shear stress transport (sst) model. This model uses the $k-\omega$ model in the inner boundary layer and switches to the $k-\epsilon$ model in the outer boundary layer and free stream [53]. This sst turbulence model thus uses the best of both worlds and is therefore renowned in industry [54] and was also selected for these CFD simulations.

4.3. Solving

The fully defined problems were subsequently solved using CFX-Solver Manager. The solver stop criterion was set to reduce the residuals (RMS) to 10^{-6}. This value was deliberately set lower than was expected, to not stop the simulation too soon. RMS values of up to 10^{-4} would also be accepted. For the problem to converge quickly, initial conditions play a crucial role. Poor initial conditions can cause the simulations to converge to a non-ideal location or not at all. All 72 setpoints are expected to form a range of flow fields, for which two neighboring setpoints are not too different. Therefore the initial conditions of a solver run could be set to the resulting conditions of the previously converged setpoint. This saved a huge amount of time. An example of the residuals RMS values during a full solving run is shown in fig. 4.8. From this figure it can be observed that all momentum, mass, and turbulence residuals RMS dropped below 10^{-5} within 40 iterations and seemed to have fully converged by 100 iterations. Nonetheless, the simulation was only terminated after approximately 50 further iterations as the actual errors converge somewhat slower than the residuals [37]. Sill, this was much faster than when no other initial conditions were used than automatic domain initialisation. In that case, convergence generally took in the order of 700 iterations.

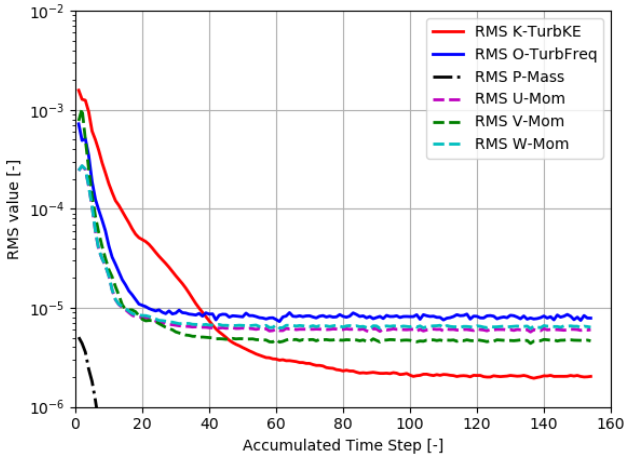

Figure 4.8: *R_SW*15_Ψ10% CFD solver residuals RMS

The timescale was another factor that could be controlled to accelerate the convergence. For every run this was initially set to automatic with a conservative length scale option. When convergence of a setpoint was steady, but relatively slow, the timescale control was adjusted mid-run to a local timescale factor of five. This increases the timescales locally in regions where the length scale is also larger.

4.4. Post-Processing

The solver results file could directly be exported to CFD-Post. Here the specific results of interest were visualised. First, a centre-plane cut out was made on which the axial velocity component was plotted with contours. This image was overlain with vectors to also be able to observe the radial velocity components as well, which allows for a intuitive comprehension of the flow with vortex breakdown and recirculation zones. An example of the centre-plane flow field is presented in fig. 4.9. From this image, the axial location of the stagnation point could easily be logged in CFD-Post.

The other parameter of interest was the effective Swirl number. This value was investigated at 2 mm downstream of the mixing tube entrance and 6 mm upstream of the dump to the combustion chamber for all cases. It was also recorded for a sweep of points along the entire mixing tube for a few cases with high geometric swirl numbers. The 3D velocity components were available for the entire domain. Therefore, the Swirl number was calculated using alternative forms of eq. (2.5), eq. (2.11). These alternative forms contain area integrals and are given in eq. (4.1) and eq. (4.2).

$$G_\theta = \int \left((v_{tan}\, r)\, \rho\, v_{ax} \right) dA \qquad (4.1) \qquad\qquad G_x = \int \left((|v_{ax}|\, r)\, \rho\, v_{ax} \right) dA \qquad (4.2)$$

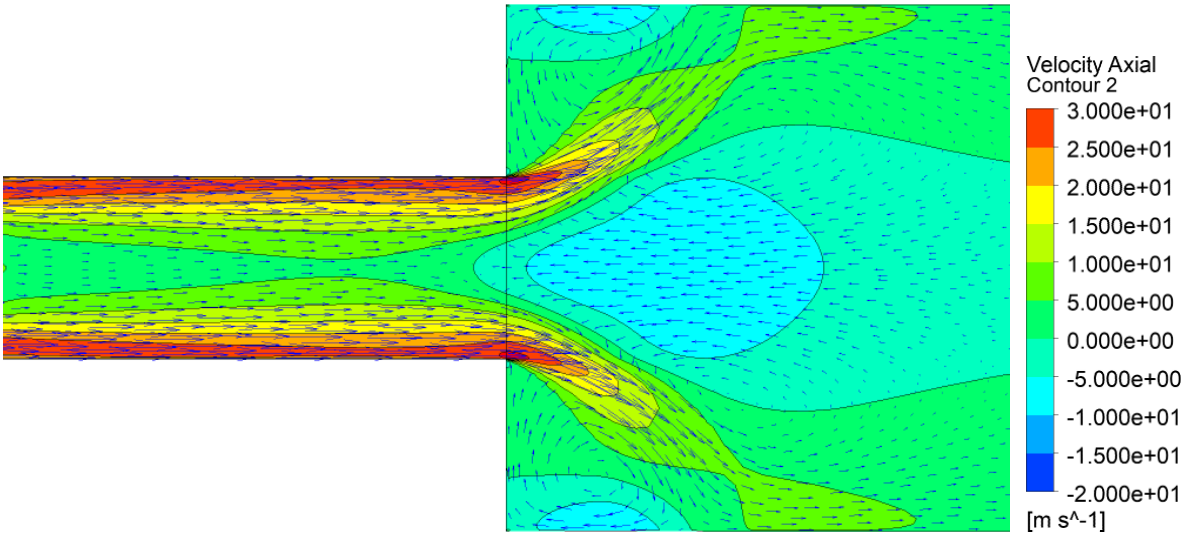

Figure 4.9: $R\_SW15\_\Psi10\%$ CFD results: centre-plane axial velocity and vectors

Note that the absolute value of v_{ax} was used for one of the terms in eq. (4.2). This was done to ensure that the Swirl number still gives a meaningful value in case there is local flow reversal. In that case v_{ax} would be negative, but its sign would be neglected when squaring the term if none of the terms were taken as the absolute value. The ratio of the two axial fluxes and the mixing tube diameter ultimately gave the Swirl number (see eq. (2.4)).

5

Methodology: Experiments

The methodology of the conducted Particle Imaging Velocimetry (PIV) experiments is presented in this chapter. In the first section (section 5.1) the experimental setup is discussed. Next, the system calibration and initialisation is treated in section 5.2. Then, section 5.3 and section 5.4 discuss the acquisition method and processing operations applied to convert raw images into vector files. Finally, the post-processing operations conducted in Python are reviewed in section 5.5.

5.1. Experimental setup

The working principles of PIV were covered before in section 2.8. This section focuses on how the PIV measurement technique was applied to the designed combustor model and what equipment was used. To obtain the Swirl number 2D PIV has to be performed twice: on the centre-plane of both mixing tube and combustor and on the cross-plane of the mixing tube.

5.1.1. Flows and Seeding Control

All three air flows to the combustor model must be independently controllable. This was achieved by using three mass flow controllers, suitable to the operating range (see fig. 5.1). The total volume flow rate of the swirl air and axial air streams combined was set to 994 $nlpm$. For the vast majority of the cases the fuel flow is set to 66.3 $nlpm$, which is just over 6% of the total volume flow. For this reason, it was decided that only the two air streams would be seeded and not the fuel stream. As the experiments will be cold flow and relatively few small particles are required, DEHS oil is best suited as seeding particles. The TU Delft high speed laboratory has this oil available along with appropriate seeding generators (or seeding pots) produced by PIVTEC (see fig. 5.2). These pots generate particles of 1.0 μm diameter when operated correctly with DEHS [63]. To get the right particle size and density, the pressure and mass flow rate through the pots must be controlled. Therefore a variable bypass system was created over the pots. A schematic diagram of this air flow and seeding system is presented in fig. 5.3.

5.1.2. Laser and Optics

A Quantel EverGreen2 Nd:YAG dual-pulse laser emitting at 532 nm was selected to illuminate the seeding particles in the flow. The pulse energy of this laser goes up to 200 mJ with a pulse width smaller than 10 ns and a repetition rate up to 15 Hz. The laser head is power and cooled by an external control unit. Therefore the laser head is relatively compact, which allows it to be easily integrated into the experimental setup. The two laser beams emitting from the laser head were measured to be approximately 9 mm in diameter approximately 2.5 metres from the head. A set of different lenses was used to change the slightly diverging beams to two thin overlapping laser sheets in the area of interest. In total five lenses were used. Their relative spacing to the upstream optic (s) and their focal lengths (f) are given in table 5.1.

From experience it was decided to install the laser head quite far from the location where the sheet must be formed. This makes it easier to acquire a thin near parallel sheet in the region of interest. The combination

Figure 5.1: Mass flow controller by Bronkhorst
Source: *Bronkhorst*[14]

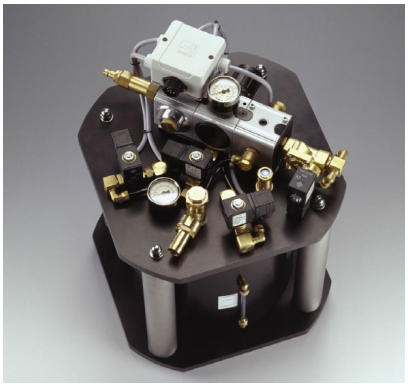

Figure 5.2: Seeding generator by PIVTEC
Source: *E. Roosenboom*[75]

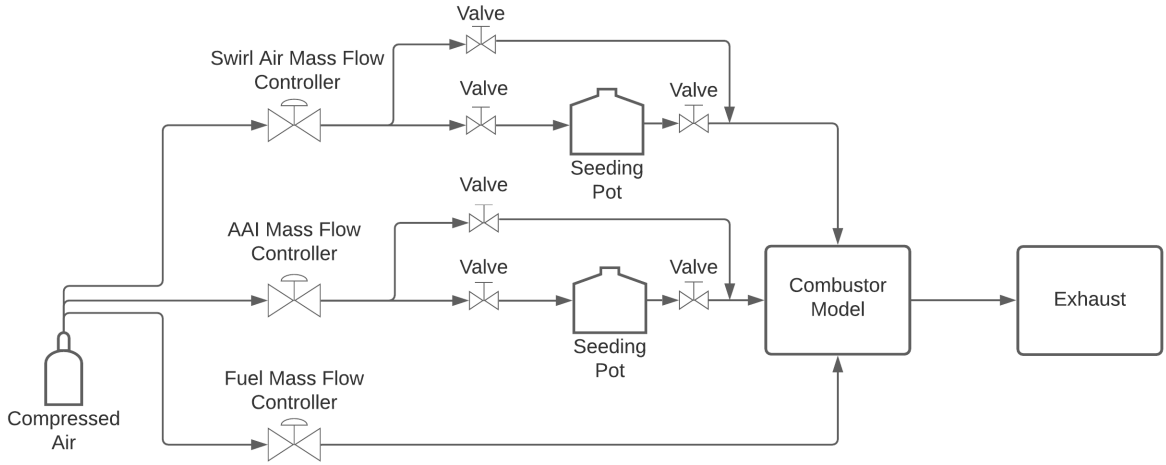

Figure 5.3: System diagram of the controllable mass flow and seeding

Table 5.1: PIV optics used to form the laser sheet

Lens ID	s [mm]	Type	f [mm]	Function
L1	33	Spherical	-75	Diverge Beam
L2	83	Spherical	+150	Converge Beam
L3	~3500	Spherical	-30	Diverge Beam/Spread Sheet
L4	31	Cylindrical	+50	Create Sheet
L5	35	Cylindrical	-30	Spread Sheet

of the first two lenses (L1 and L2) causes the beams to be nearly parallel, but slightly converging at approximately four metres away. This distance was realised with the use of the 45 degree mirrors. The first mirror reflected the beam horizontally and the second was directly below the region of interest and reflected the laser beam vertically up. Just downstream of the second mirror was the third lens (L3). This spherical lens caused the beam to diverge again in all directions. The divergence over one axis was countered by L4, which ensured a sheet is formed with a focal point in the region of interest. This focal point is the sheet minimum thickness and was measured to be 2 mm. The final lens (L5) was just downstream of L4 and spread the sheet, making it long enough to cover the entire region of interest. All lenses were mounted in square cases which could be easily aligned with each other. To switch between the centre-plane and cross-plane setup, only L4 and L5 had to be rotated by 90 degrees. This caused the sheet to spread perpendicular to the other setup.

5.1.3. Cameras and Timing Unit

To capture the scattering seeding twice over a short time time interval, a dual shutter camera was used. A LaVision Imager sCMOS CLHS was selected as it is well suited for PIV with very low noise, quick repetition rate, and a high spatial resolution of 2560x2160 pixels that are 6.5x6.5 μm in size [48]. The sCMOS camera is also quite compact and can be mounted on the frame with the combustor model and laser optics, perpendicular to the laser sheet. The imager is illustrated in fig. 5.4.

For the centre-plane measurement the area of interest spans 200 mm in axial direction. This covers the entire mixing tube and the first 100 mm of the combustion chamber. To increase the spatial resolution of this field, it was decided to utilise two cameras: one for the mixing tube and one for the combustion chamber. This allows one camera to capture 100 mm on 2560 pixels, which gives a maximum resolution of 25.6 pix/mm. The field of interest for cross-plane measurement is a circle with diameter 36 mm. This can easily be captured on a single camera while maintaining a high spatial resolution. However, to capture this plane the camera would have to be downstream in the seeded flow. To avoid blemishing the lens or damaging the camera a mirror was positioned between the combustor and lens at 45 degrees in the flow, reflecting the light 90 degrees horizontally. The mirror was 270 mm downstream of the combustor exhaust and was assumed not influence the flow in the region of interest. With this setup the camera and lens could remain out of harms way.

Finally, to control the laser and camera(s) a Programmable Timing Unit (PTU) by LaVision was used and controlled working on DaVis 8.4.0 software. When a measurement was taken the laser pulse interval and frequency were set in DaVis (see section 5.2). These settings were then controlled by the PTU, which regulates the trigger timing of the laser pulses and camera shutters so that they coincide. The PTU is shown in fig. 5.5.

Figure 5.4: LaVision Imager sCMOS CLHS
Source: *LaVision*[48]

Figure 5.5: LaVision Programmable Timing Unit
Source: *LaVision*[47]

A schematic drawing of both PIV setups including the combustor model, laser head, laser optics, laser sheet, mirrors, and camera(s) is presented in fig. 5.6 and fig. 5.7. The relative distances between the laser optics is changed to present the setups more clearly. All illustrated components were mounted on a specifically designed and produced rigid aluminum frame for the experiments.

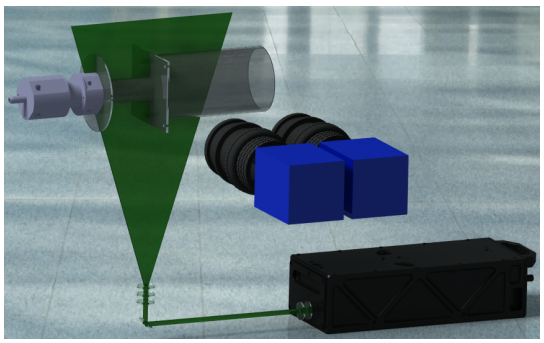

Figure 5.6: Schematic drawing of centre-plane PIV setup

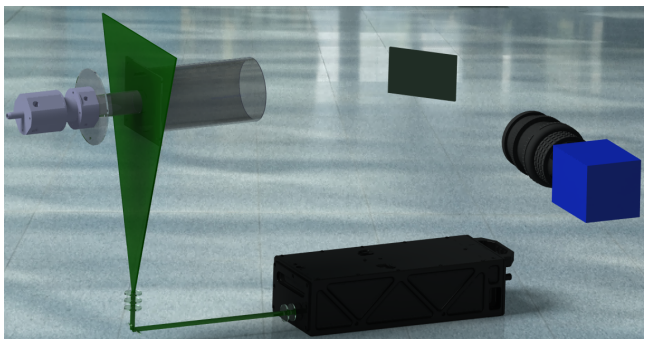

Figure 5.7: Schematic drawing of cross-plane PIV setup

5.1.4. Exhaust

A final important component of the setup was the exhaust. Because the air was seeded with DEHS it was necessary to ventilate to avoid the seeded flow fogging up the TU Delft facility. This was achieved by mounting a 400 mm diameter fan in front of an exhaust hole in the wall. The exhaust of the combustor model was mounted such that it faced directly towards this fan. To diminish any upstream swirling effect of the fan, 200 mm long honeycomb structure was mounted in front of the fan acting as a flow straightener. With a distance of 1.7 m between the combustor exhaust and the flow straighteners, it was assumed that the upstream effect of the fan would be negligible. This was later confirmed a valid assumption when the experimental data was investigated. The bare exhaust fan is shown in fig. 5.8 and the fan as used in the experiments is shown in fig. 5.9.

Figure 5.8: Exhaust fan

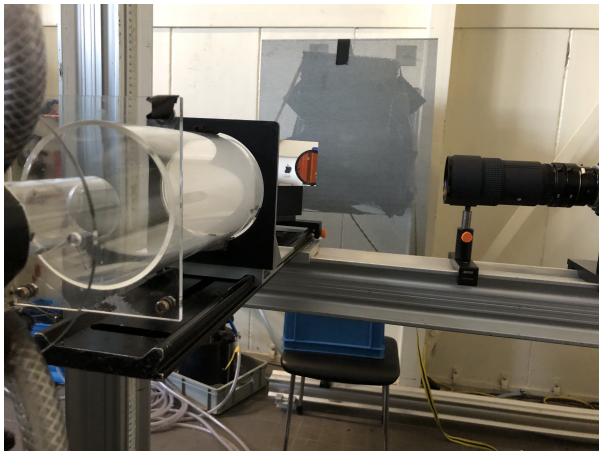

Figure 5.9: Cross-plane setup including exhaust fan

5.2. Systems Initialisation

This section will cover the steps taken to properly prepare the setup for the acquisition of the images for PIV. More specifically, the camera calibration, laser timing, flow seeding quality, and the reduction of reflections is discussed.

5.2.1. Field of View

For the centre-line setup, both sCMOS cameras were equipped with $f = 105$ mm lenses. The cameras were mounted on the frame with the camera focusing on the mixing tube slightly more forward to increase the magnification. A calibration paper was inserted in the combustor at the centre-plane to measure the field of view, and the resulting spatial resolution. The two images taken by the cameras of the calibration paper are presented in fig. 5.10. These images were used to set the origin of the reference frame and to set the scaling of the two cameras.

For the radial swirler model, the field of view of the mixing tube was found to be 97.9 mm in axial direction from 97.3 mm upstream of the dump to 0.6 mm downstream of the dump. This yields a magnification of 0.170 eq. (5.1) and a spatial resolution of 26.1 pix/mm eq. (5.2). However, the effective field of view was slightly smaller as the laser sheet was obstructed by the nut and its matt-black cover on the bottom side of the mixing tube, connecting it to the swirler module upstream. This caused the light to be blocked and thus the effective field of view to be reduced by a triangle shape on the upstream end of the mixing tube extending to approximately 89 mm upstream of the dump on the bottom of the tube. The flanges connecting the mixing tube to the combustion chamber are directly below the laser sheet, but still form and obstruction as the light cannot pass directly through them without changing direction. Therefore the bottom ends of these flanges were covered with matt black tape. This caused the effective field of view to be reduced to approximately 4.5 mm upstream of the dump. When switching to the axial swirler model, the field of view was recalibrated. The magnification was nearly identical and the field shifted slightly downstream with 0.2 mm.

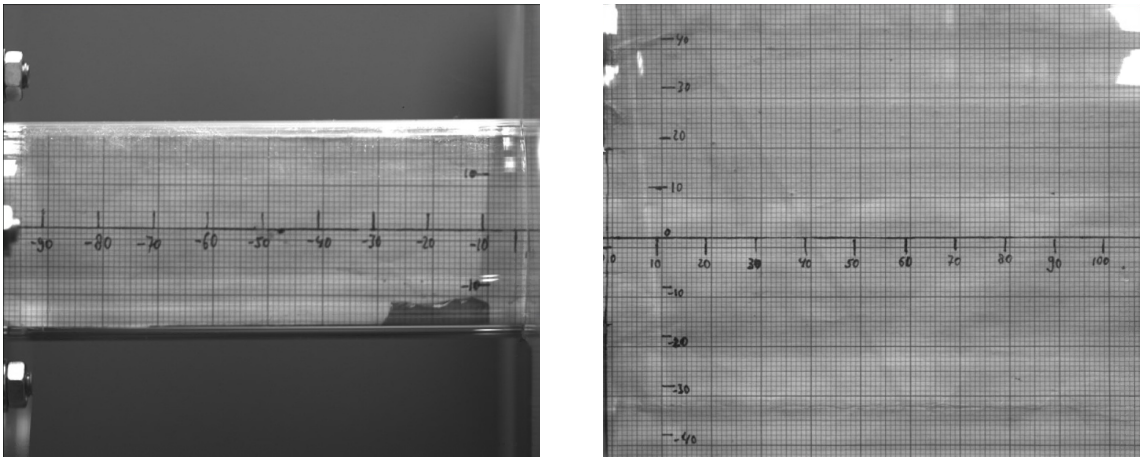

(a) Mixing tube calibration image

(b) Combustion chamber calibration image

Figure 5.10: Calibration papers captured by the two centre-plane cameras

$$M = \frac{d_{im}}{d_{obj}} \tag{5.1}$$

$$Res = \frac{N_{pix}}{d_{obj}} \tag{5.2}$$

The second camera, focusing on the combustion chamber, had a total field of view of 108.3x91.3 mm starting at 0.8 mm upstream of the dump to 107.5 mm downstream of the dump and running from 43.2 mm below the centreline to 48.1 mm above the centreline for the radial swirler model. With a inner radius of 52 mm, the combustor is thus not fully captured to the walls. This is not an issue for this experiment as the focus is on the stagnation point near the centerline. Besides, the near wall data is heavily distorted due to reflections and warping images through the curved plexiglass tube. Applying eq. (5.1) and eq. (5.2) again, yields a magnification of 0.154 and a spatial resolution of 23.6 pix/mm in the combustion chamber. Similar to the other camera, this effective field of view was also decreased slightly by the flanges. For this camera the obstruction causes the most upstream illuminated location to be at 1.2 mm downstream of the dump. This camera was also recalibrated when switching to the axial swirler setup. This resulted in a nearly identical magnification and a shift in field of view upstream by approximately 0.1 mm and down by 1.3 mm, bringing the centreline closer to the centre of the image. For both swirler models, the total centre-plane effective field of view thus runs from 89 mm upstream of the dump to 107.5 mm downstream of the dump with a gap from -4.5 mm to 1.5 mm w.r.t the dump.

For the cross-plane setup a single camera was positioned perpendicular to the combustor model with a 45 degree mirror in between the two. An $f = 180$ mm lens was used to achieve a large magnification of the area of interest. A calibration paper for the cross-plane was inserted in the mixing tube at 6 mm upstream of the dump. The entire cross-plane was in the field of view for both radial and axial swirler models. However there was a small change in scaling between the two models as the mirror had to be repositioned. The calibration images taken with the camera for both swirler models is shown in fig. 5.11. The resulting magnification and resolution of the cross-plane were 0.291 and 44.8 pix/mm for the radial swirler model and 0.281 and 43.3 pix/mm for the axial swirler model.

5.2.2. Camera Focus

The cameras were manually focused on the seeding particles in the sheet. In order to capture all particles in the sheet in focus, the depth of focus must be larger than the sheet thickness. For all scenarios the approximate sheet thickness was 2 mm. The depth of focus (DOF) is given by eq. (5.3) [32], in which λ is the light wavelength and $f_\#$ is the F-stop (a camera setting indicating how far the lens aperture opens). During focusing this F-stop was set to the minimum value of 2.8, This yields a DOF of 0.96 mm for the mixing tube, 1.14 mm for the combustion chamber, and 0.4 mm for the cross-plane. These minimum DOFs are smaller than the sheet thickness of 2 mm, which allows accurate focusing on the sheet. When acquiring data the DOF should be larger than the sheet thickness to capture all particles in the sheet in focus.

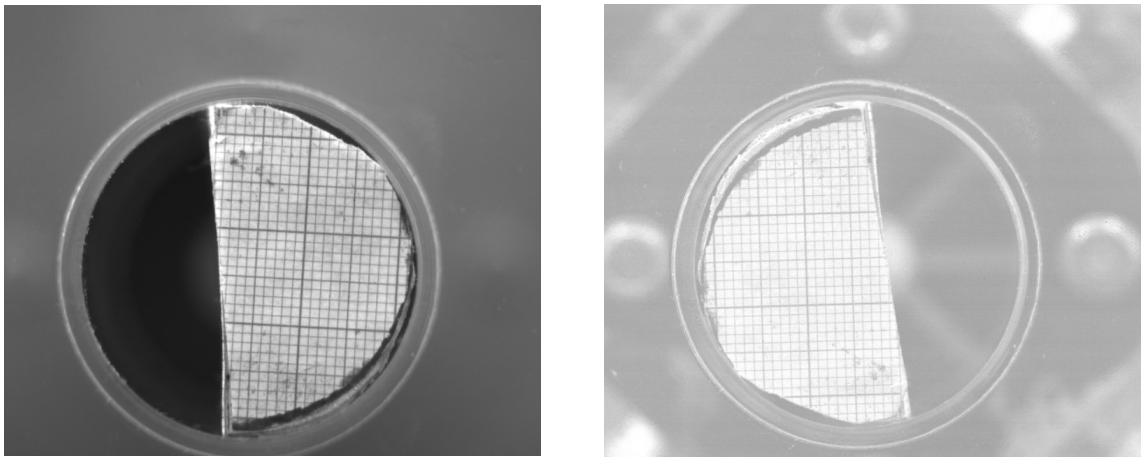

(a) Radial swirler model calibration image

(b) Axial swirler model calibration image

Figure 5.11: Calibration papers captured by the cross-plane camera

Another parameter to take into account when focusing is the apparent size of the particles on the sensor (d_τ) eq. (5.4) [32]. As a design rule this size should be larger than two pixels in order to avoid peak locking. This apparent size is a function of the actual particle size on the sensor eq. (5.5) and the diffraction size eq. (5.6), which are in turn dependent on the F-stop and the magnification. For the centre-plane cameras the F-stop was set to 11 to achieve a d_τ of over two pixels. For the cross-plane an F-stop of 8 sufficed.

$$DOF = 4.88\lambda f_\#^2 \left(\frac{M+1}{M}\right)^2 \tag{5.3}$$

$$d_\tau = \sqrt{\left(d_{geom}\right)^2 + \left(d_{diff}\right)^2} \tag{5.4}$$

$$d_{geom} = M\, d_p \tag{5.5}$$

$$d_{diff} = 2.44\lambda(1+M) f_\# \tag{5.6}$$

5.2.3. Timing

Once the camera setting were fixed, the first trial measurements could be conducted. To be able to cross-correlate the two consecutive images, the laser pulse interval (dt) must be chosen appropriately. If the dt is too long, too many illuminated particles in the first frame will not be illuminated in the second frame and vise versa. In this case, many particles will have travelled through the laser sheet because of an out of plane velocity component. This can especially be a problem for the swirling flows in this study as the out of plane velocity component is relatively high. On the other hand, decreasing dt will decrease the distance a particle can travel in-plane between two laser pulses. As a consequence the accuracy of the resulting vectors will be reduced. In traditional PIV this was a larger problem. Generally particles were designed to travel 1/4 of the interrogation window size.

However, with the more modern multi-pass cross-correlation technique the interrogation window size and location can be varied. Therefore the spatial resolution is significantly improved and reliable vectors can still be generated for particle displacement of only a few pixels [76]. As the DaVis software, that was employed for this study, is equipped with this multi-pass technique, it was possible to use a dt as low as 6 μs for the highest swirl cases. It was varied up to 15 μs for other measurements. For every newly installed swirler, the dt was varied for a few quick measurements. The correlation peaks for these measurements were compared, after which the optimum value of dt was chosen for the full measurements. It was possible to adopt a single dt value for the both mixing tube and combustion chamber in centre-plane measurements. This allowed the two cameras to capture the images simultaneously, which saved an enormous amount of time. The total number of images taken for a setpoint was set to 500. For the centre-plane measurements this comes down to 1000 images, each with 2 frames. The acquisition frequency was set to 15 Hz. The correlation peaks were continuously evaluated for completed measurements. When a problem was found, one of the parameters that could be varied to fix it, was the pulse interval.

5.2.4. Seeding Quality

Another parameter that can have a strong effect on the correlation peaks is the seeding density and distribution. For each setpoint the bypass valves of the seeding generators had to be manually adjusted to find a good distribution of the seeding between the two seeded streams. For example, when going from 5% to 10% AAI, the amount of flow through the swirl air seeding pot reduces. As a consequence its bypass valve should be slightly further closed to get similar flow and pressure through the seeding generator, and thus similar seeding density in that stream. In the same scenario the flow through the AAI seeder doubles. As a consequence the bypass valve should be further opened to reduce the flow and pressure through the seeder. An example of poorly distributed and improved seeding is presented in fig. 5.12.

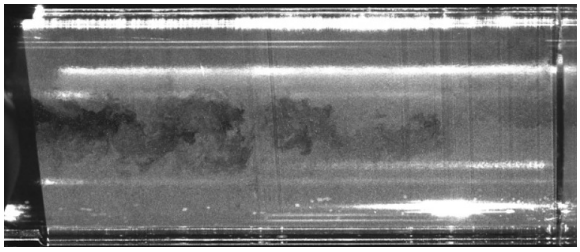

(a) Poorly seeded flow: too high on swirling air and too low on AAI

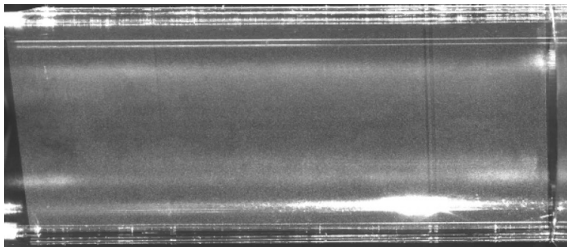

(b) Well seeded flow: well distributed seeding density

Figure 5.12: Calibration papers captured by the cross-plane camera

5.2.5. Reflections

The final major improvement that was made to the PIV setup was the reduction of reflections. Since a bright light (laser) was aimed on a curved surface that is not perfectly transparent, there were unwanted internal reflections of the laser sheet. Due to imperfect alignment of the sheet with the tubes, these reflections occur in other directions than perfectly vertical. These internal reflections could cause particles to be correlated from other locations than the original sheet. To avoid this, matt black foil was applied on the far half (from the centre-plane camera's point of view) of the wall of the mixing tube and combustion chamber. Besides internal reflections, reflections from other components or materials could also cause bright spots on the captured images. These spots make it harder or even impossible to distinguish between individual particles. In the worst case, very bright sports could over-saturate and damage the camera sensor (blooming). To avoid this, the matt black foil was also applied to the nuts and bolts of the setup that could reflect the laser light. The aluminum manifolds close to the plexiglass components were also spray painted in matt black to reduce reflections of their surface. The actual combustor model as used for the radial swirler centre-plane measurements is presented in fig. 5.13. For the cross-plane measurements the foil on the inside of the tube obviously had to be removed to be able to fully illuminate the mixing tube. An image looking upstream into the combustion chamber for this setup is presented in fig. 5.14. From this image the matt black foil on the upstream flange of the mixing tube and relevant nuts and bolts can also be observed.

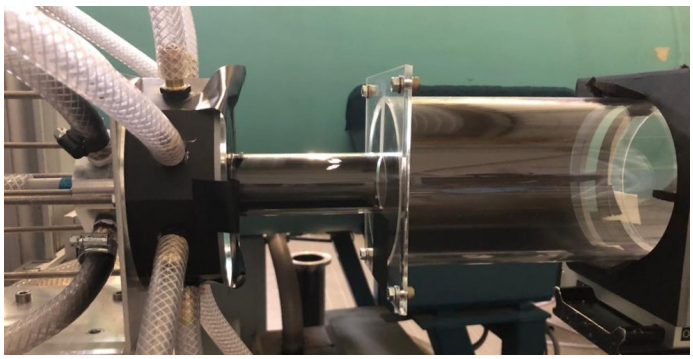

Figure 5.13: Centre-plane setup with reflection reduction

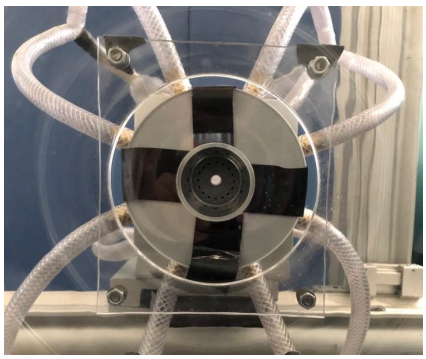

Figure 5.14: Cross-plane setup with reflection reduction

To reduce light pollution further, all experiments were conducted with dimmed ambient lighting and all cam-

eras were equipped with a green light filter. This blocks light at all wavelengths and only lets a narrow band of green light wavelengths through.

5.3. Acquisition

The original test matrix consisted of the same 72 setpoints as intended for CFD (two swirler types, each with six geometric Swirl numbers and six different settings of Ψ). However this would take too much time to experimentally investigate. Because, of all variables, switching between swirlers would take the most time, half of the swirlers were discarded. Three axial swirlers and three radial swirlers were selected, each with geometric swirl numbers 0.7, 1.1 and 1.5. On the other hand, different Ψ settings were relatively quick to implement for a new recording. Therefore, it was decided to expand the test matrix with higher Ψ setpoints until vortex breakdown was destroyed or another limit was reached.

During the entire duration of the experiments, the low fuel flow was not switched off. The two seeded flow were reduced to zero between every run. This was necessary for two reasons. First, DEHS oil droplets started forming on the mixing tube wall after approximately a minute of running the seeding flows. This had to be carefully cleaned between every run to not decrease the quality of the next acquisition. Second, switching off both air flows ensured that no hysteresis effect was present in the experiments, which is important with respect to vortex breakdown (see section 2.5.4). At the start of every run, the swirling air was introduced and stabilized first, before the axial air was introduced. Therefore, the swirl intensity was always maximum before it was decreased to the desired setpoint.

5.4. Processing

All acquired data sets from experiment went through a list of operations to be processed from a set of raw images to an averaged vector file. In this section all of these operations, that were performed in DaVis 8.4.0, will be discussed.

5.4.1. Masking

All raw data sets together formed a huge amount of data. To speed up the processing of these data sets, as a first step the size of the images was reduced by masking out the irrelevant areas in the images. Especially for the centre-plane images of the mixing tube and for the cross-plane images, this significantly reduced the size data sets for the further operations. Figure 5.15 shows examples of the masking profiles for the mixing tube and centre-plane and cross-plane images. The area outside of the blue masking profiles was discarded for the remainder of the operations. This reduced the data size to be further processed by 45% for the centre-plane measurements and 49% for the cross-plane measurements.

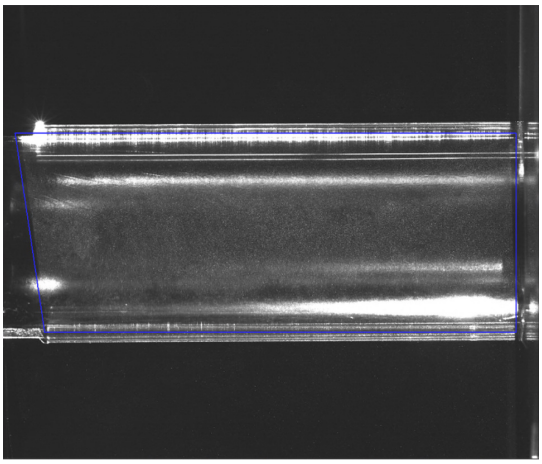

(a) Centre-plane masking of mixing tube

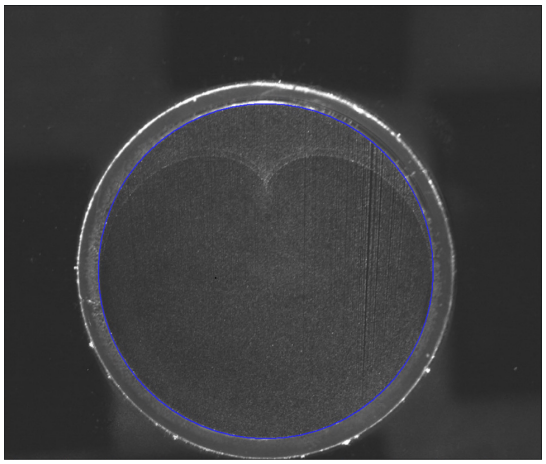

(b) Cross-plane masking of mixing tube

Figure 5.15: Masking profiles for raw images

For the centre-plane setup the masking profile was only created once and could be used for all images. However, for the centre-plane setup, a specific mask was generated for every single data set. This was necessary as between acquisition runs the any seeding deposit that stuck to the surface of the mirror was removed, which moved the mirror ever so slightly. Normally this would not be a problem if the mask were slightly larger than the object. It was however decided that the mask should perfectly enclose the relevant mixing tube cross-section without margin. This was done so that the exact cross-section centre location was recorded in pixel coordinates. This location was required for the vector decomposition as described in section 5.4.5.

5.4.2. Background Subtraction

Once the masks were created the intensity was filtered temporally by subtracting the minimum intensity of every pixel over 99 images. This time-filter of 99 images was applied symmetrically over the image range. The effect of this operation is a background intensity subtraction. This results in a set of images where background noise and reflections are removed. The time-filtered result of fig. 5.15a is presented in fig. 5.16. From this image can clearly be seen that the bright spots of the image are reduced. The bottom right bright spot is a consequence of internal reflections and is not completely removed with the background subtraction operation. This shows that the reflection in a part of this region is too strong to be removed. The variation in intensity captured from this reflection is thus higher than the intensity of the individual particles. These regions will likely not be able to find a solid cross-correlation.

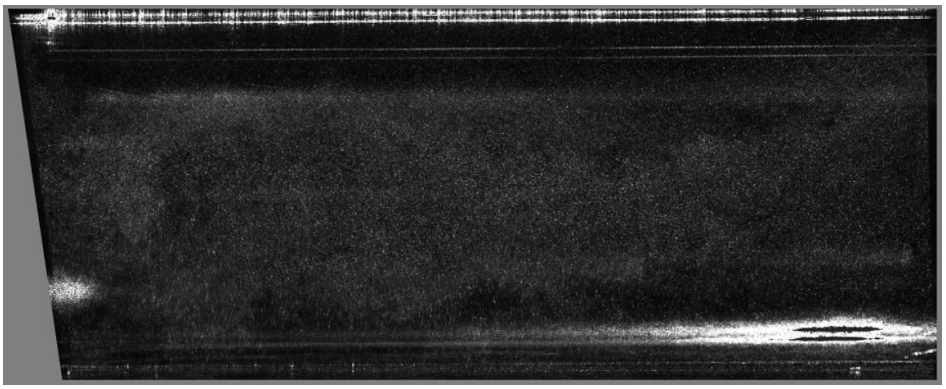

Figure 5.16: Background subtraction of the centre-plane mixing tube (time-filtered)

5.4.3. PIV Vector Calculation

As mentioned before, the PIV vector calculation uses a multi-pass cross correlation method. More specifically, a decreasing size variant is used. In this algorithm, the interrogation window (IW) is relatively large for the first passes which ensures the in plane particle displacement is not too large to be captured. For every pass the IW is shifted to find the best initial guess of the vectors in that area. These initial vector guesses are then further refined by more passes of smaller new IWs. The size of the final IWs and the overlap between them determine the final resolution of the obtained vector field. For all PIV vector calculations, three passes were first performed over square IWs of size 128x128 pixels with a 50% overlap. Then two more passes were performed over circular 32x32 pixel IWs with a 75% overlap. The final overlap of 75% on the 32 pixel IWs yields a vector resolution 8x8 pixels or approximately three vectors per mm for the centre-plane measurements and 5.5 vectors per mm for the cross-plane measurements. The resulting vector field from this operation for the mixing tube in fig. 5.16 is presented in fig. 5.17. In this image the vector density is reduced by a factor 8 for clearer distinction between the vectors.

5.4.4. Averaging

The final operation for the centre-plane measurements (and second-to-last for the cross-plane measurements) is the temporal averaging over 500 images. This operation is performed as this study focuses on the averaged flow field for a certain setpoint. There generally was locally significant variation between instantaneous frames, but investigation into this is reserved for future studies. The averaged vectors for the mixing

tube example ($R\_SW15\_\Psi 20\%$) are presented in fig. 5.18. Both images have the axial velocity component displayed as the background of the vectors. Comparing the two images, it can clearly be seen that the averaged vectors show a more axisymmetric plane with reduced maximum velocity. The regions where the reflections were strong, show a poor correlation indicated by axial velocity near zero.

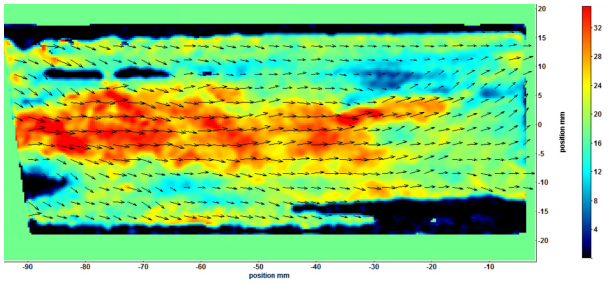

Figure 5.17: Vector field for single image

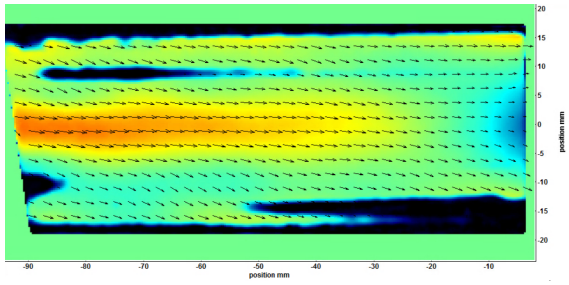

Figure 5.18: Averaged vector field from 500 images

5.4.5. Vector Decomposition

The vectors obtained from the multi-pass cross-correlation are decomposed into a format of x- and y-velocity components by default. For the centre-plane measurements this is very useful, as the axial velocity is then equal to v_x. The vector files are thus exported as v_x and v_y components for every (x, y) coordinate separated by eight pixels. However, for the cross-plane measurements the more relevant vector component is the tangential velocity component (v_{tan}). To obtain this component the vectors had to be decomposed into v_{tan} and v_r. This was done by converting the domain into polar coordinates, which required the origin location in Cartesian coordinates. This location was obtained for each cross-plane measurement from the masking operation section 5.4.1. The tangential- and radial velocity components were then obtained as two scalar fields that were ultimately exported.

5.5. Post-Processing

The averaged vector and scalar fields that were exported were further processed using a custom Python script to locate the stagnation point (section 5.5.1) and to derive the Swirl number (section 5.5.4). This section discusses these operations.

5.5.1. Stagnation Point Location

To obtain the location of the stagnation point, first the averaged centre-plane vector fields were imported and converted to a convenient data format. They were then plotted similar to the vector images shown in DaVis, with v_x on the background. Next, a contour plot was created for the contour where axial velocity equals zero. This contour plot was overlain with the vector field and showed the zero axial velocity contour in bright red. For all setpoints no flow reversal was found inside the mixing tube. The contours were thus only visible for the combustion chamber centre-plane fields. A Gaussian filter was applied over the contour to get rid of any outliers or potential small recirculation islands. The result was a relatively smooth contour of the recirculation zone. This contour plot is shown for an example case in fig. 5.19. The contour clearly indicates the central recirculation zone and also identifies part of the toroidal outer recirculation zone. The most upstream stagnation point of the inner recirculation zone is of interest for this study. The coordinates for the contour(s) were listed for a range within 20 mm of the centreline to remove the contours of the outer recirculation zone. The most upstream coordinate of this list was then recorded as the stagnation point location for this setpoint.

For a few cases the contour of the inner recirculation zone was interrupted near the upstream edge of the field of view of the combustion chamber. This indicated that the actual upstream stagnation point was located in the 'blind spot' between the mixing tube and combustion chamber. If this was the case the two contours profiles in the combustion chamber were extended upstream by extrapolation. The intersection of the two extrapolated curves then indicated the location of the upstream stagnation point. An example of this method is presented in fig. 5.20.

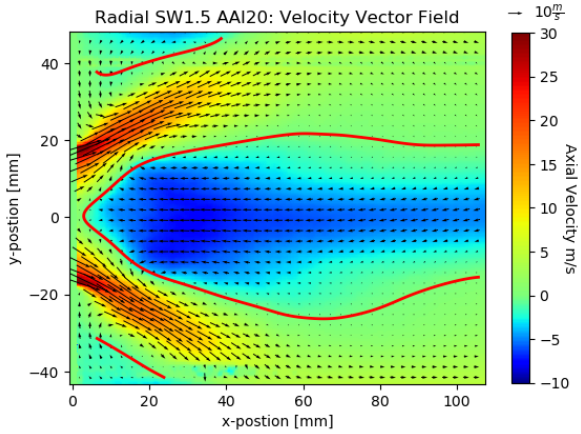

Figure 5.19: Vector field of the combustion chamber incl. contour

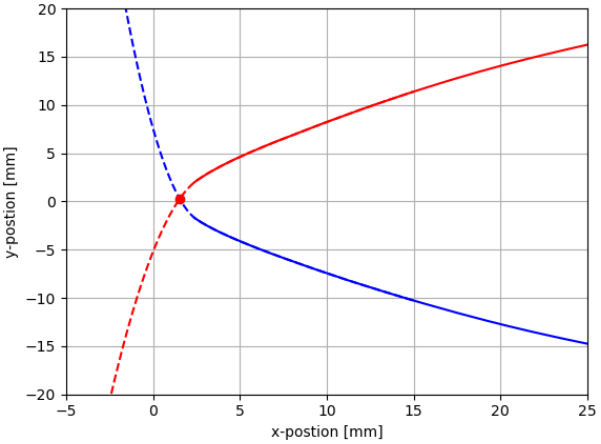

Figure 5.20: Stagnation point from contour extrapolation

5.5.2. Radial Profile of Axial Velocity

From the centre-plane of the mixing tube at any axial location, a radial profile of the axial velocity component could be obtained. The location of interest for this profile was at $x = -6\ mm$, the axial location of the cross-plane measurements. Only a single profile from centre to wall is required to obtain the Swirl number. Even though there were two profiles available for every setpoint: going up (N) or down (S), neither profile had accurate vector result in the near wall region due to warping and reflections. Therefore the wall region had to be recreated by extrapolating the existing profile from the point where data was being lost up to the wall, where velocity is assumed equal to zero due to the no-slip condition. Dependent on the two profiles this extrapolation was either performed on a single smoothed profile or on the (smoothed) average of the two profiles.

For example, the radial profiles of the radial swirler with geometric swirl number equal to 1.5 and no axial air injection ($R\_SW15\_\Psi0\%$) was nearly perfectly symmetrical over the centreline, but the lost wall region was significantly larger on the lower half than on the upper half (see fig. 5.21a). For this case the recreated wall region was appended to the 'best' profile in stead of the average of the two.The shape of this appended near-wall profile was optimized to match the mass flow rate. This was possible, because the physical mass-flow rate was measured (converted from the volume flow rate) during the experiments and the resulting axial velocity profile could be integrated using eq. (5.7) to obtain the mass flow rate as well. Obviously, these mass flow rates should match under the condition that the smoothed axial velocity profile is equal to the averaged axial velocity profile for the entire cross section. This final condition was assumed to be true as the centre-plane vector field was obtained from 500 images. The resulting smoothed axial velocity profile is presented in fig. 5.21b.

$$\dot{m}_{tot} = \int_0^R \left(2\pi\, r\, v_{ax}\, \rho_{air}\right)\, dr \tag{5.7}$$

On the other hand, the the axial velocity profile of the A_SW11_AAI0 setpoint was more asymmetric about the centreline, but does have similar sized distorted wall regions (see fig. 5.22a). These profiles were thus first averaged and then improved near the wall. The resulting smoothed profile was also shaped to match the mass flow rate and is presented in fig. 5.22b.

5.5.3. Radial Profile of Tangential Velocity

Similarly, a radial profile of the tangential velocity was also required to ultimately determine the Swirl number. The tangential velocity component was imported as a scalar field in Cartesian coordinates. The origin of the Cartesian coordinates still spawned from the initial calibration (scaling) of the cross-plane setup. The

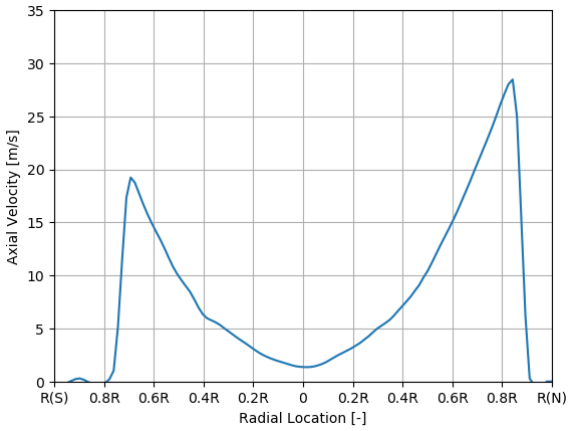

(a) Raw axial velocity profile

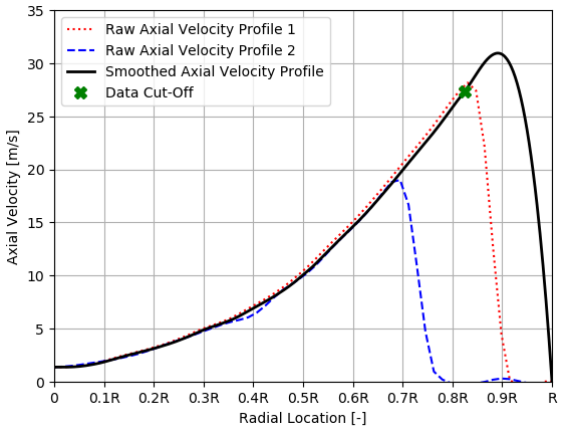

(b) Raw and smoothed profiles

Figure 5.21: *R_SW*15_*AAI*0: Radial profiles of axial velocity

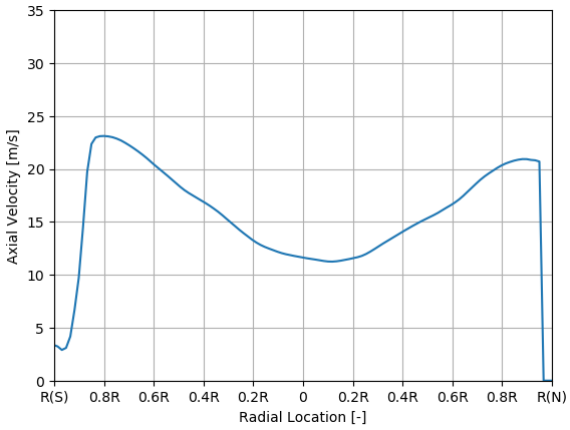

(a) Raw axial velocity profile

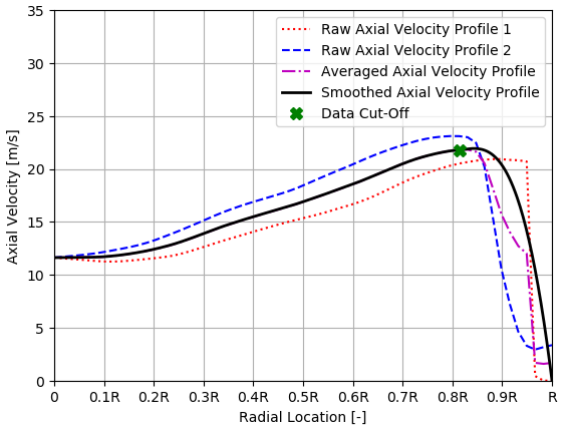

(b) Raw and smoothed profiles

Figure 5.22: *A_SW*11_*AAI*0: Radial profiles of axial velocity

location of this origin was thus corrected to the origin location as found in section 5.4.1. Next, the Cartesian coordinates were converted to polar coordinated by eq. (5.8) and eq. (5.9).

$$r = \sqrt{x^2 + y^2} \tag{5.8}$$

$$\theta = \tan^{-1}\left(\frac{y}{x}\right) \tag{5.9}$$

The scalar field of tangential velocity was then plotted in polar coordinates. The field for the previously used example *A_SW*11_Ψ0% is presented in fig. 5.23a. The positive direction for tangential velocity in this plot is in the counter-clockwise direction. This plot is derived from images taken through a mirror, looking upstream into the mixing tube. So the vector fields should be interpreted as looking downstream through the mixing tube. Finally, the cross section scalar field was reduced to a single averaged radial profile. This radial profile did not require any gaps to be filled as the image was not distorted by curved surfaces or reflections. Therefore the values were also captured with good accuracy in the near wall region. The averaged radial profile is presented in fig. 5.23b together with the smoothed axial velocity profile.

5.5.4. Experimental Swirl Number

With the radial profiles of axial- and tangential velocities known at the axial position $x = -6\,mm$, the experimental Swirl number can finally, be calculated using eq. (5.12). This was achieved through the integration of the profiles to obtain the axial flux of angular momentum eq. (5.10) and axial thrust eq. (5.11).

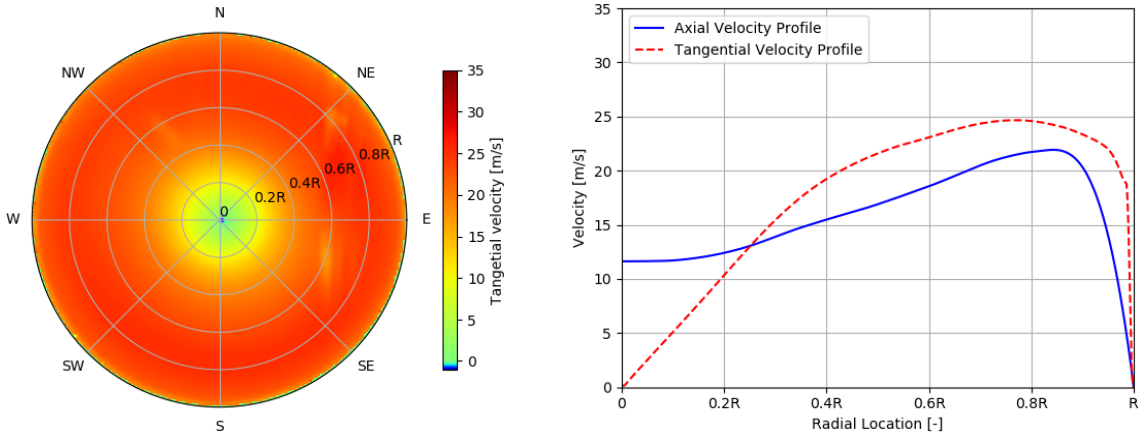

(a) Tangential velocity field

(b) Axial and tangential velocity profiles

Figure 5.23: *A_SW11_AAI0*: Tangential velocity

$$G_\theta = \int_0^R \left(v_{tan}\, r\, \rho\, v_{ax}\, 2\pi\, r\right) dr \qquad (5.10) \qquad G_x = \int_0^R \left(\rho\, v_{ax}^2\, 2\pi\, r\right) dr \qquad (5.11) \qquad Sw = \frac{G_\theta}{G_x\, R} \qquad (5.12)$$

6

Results and Analysis

This chapter will present and analyse the results from both the numerical simulations and the conducted experiments. The results from CFD simulations will first be treated in section 6.1. Next the results from the PIV experiments will be separately discussed in section 6.2. Finally, the results of the numerical and experimental campaign are compared in section 6.3.

6.1. Computational Fluid Dynamcis

The CFD results gave a first indication of the swirl generators' performances before the experimental campaign. Note that the individual results should be treated with apt skepticism as the performed CFD simulations were of relatively low fidelity and conducted using RANS. However, the results provide compelling insights on a qualitative level. The results regarding the Swirl number are first analysed in section 6.1.1 and section 6.1.2. Then, section 6.1.3 presents and discusses the CFD results regarding the flashback propensity based on the axial location of the stagnation point.

6.1.1. Effective Swirl Number

The geometric Swirl numbers were based on theory and the location at which they are met is supposed to be at the plane just downstream of the trailing edge of the swirler vanes. However, the relevant Swirl intensity for this study is the measured Swirl number from velocity components just upstream of the sudden expansion (dump) from mixing tube to combustion chamber. Therefore the geometric Swirl numbers have no other function than to identify the swirl generator of interest. All Swirl numbers for varying AAI quantity (Ψ) at 6 mm upstream of the dump extracted from the CFD simulations are presented in fig. 6.1. It should be noted that not all 72 original setpoints were simulated. Simulations were generally not solved when the previous case (with 5% less Ψ) did not show vortex breakdown. These cases without vortex breakdown were considered less relevant for this study.

From the setpoints that were solved, a number of observations can be made. First of all, for all swirl generators the effective Swirl number decreases with increasing amount of axial air injection. Looking at the equation for the Swirl number (eq. (2.4)), this decrease must be caused by a decreased ratio of axial flux of angular momentum (G_θ) to axial thrust (G_x). Interestingly, the axial thrust actually decreases slightly, while the numerator decreases drastically. For example, G_θ decreases by 45% and G_x decreases by 6.7% for R_SW15 from zero to 25% Ψ. The tangential velocity fields in the mixing tube for these two extreme cases are presented in fig. 6.2. From this figure it can clearly be seen that the tangential velocity is low for both near the centre-line and that the AAI has a significant effect of the tangential velocity component near the wall. This suggest that the non-swirling jet on the centre-line introduces a strong shearing flow that traverses throughout the entire radius of the mixing tube.

A second observation that was made from fig. 6.1 is that for equal geometrical Swirl number, the radial swirl generators have a higher effective Swirl number. Based on these results the axial swirler with geometric Swirl number 1.5 generates the same effective Swirl number as the radial swirler with geometric Swirl number 0.9. This implies that the used theoretical design rules are too conservative in predicting the swirl number. The

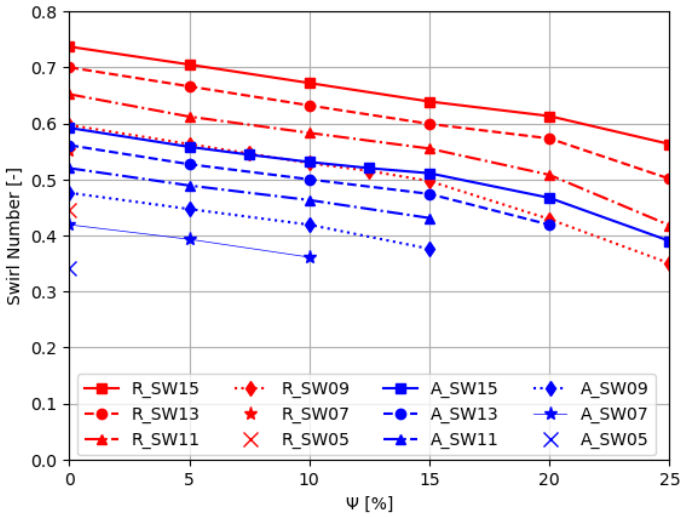

Figure 6.1: CFD: Swirl numbers at $x = -6\ mm$ vs Ψ

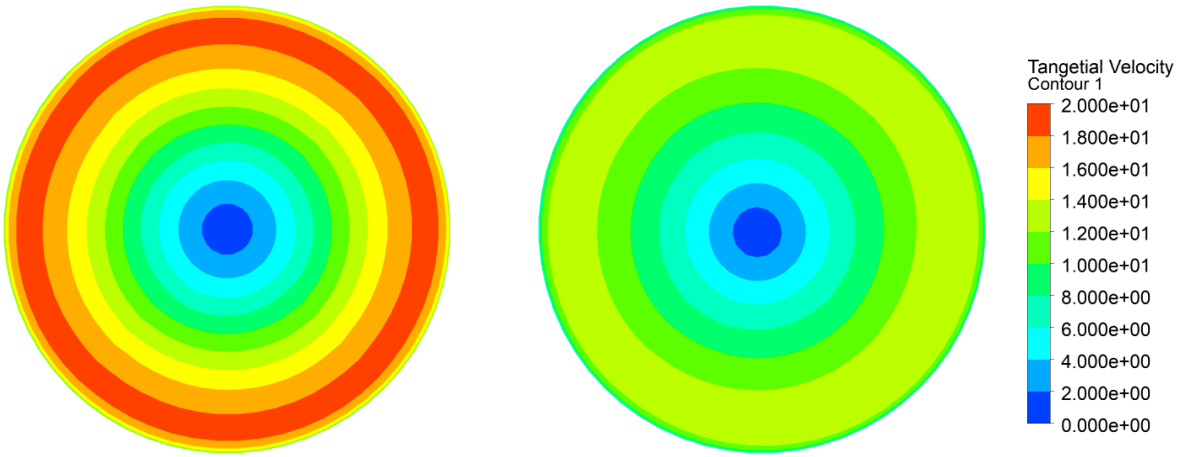

(a) $\Psi = 0\%$ (b) $\Psi = 25\%$

Figure 6.2: Tangential velocity fields of R_SW09 at $x = -6\ mm$

difference could also be associated to the errors in CFD. The averaging of the Navier Stokes equations in the RANS simulations is likely to under-predict large flow deflections that occur in the axial swirler vanes. Another factor that could contribute to this offset is the mesh quality. The structured meshes were of decent quality, but the lowest quality occurred in the axial swirler vanes. The meshes could be more refined at these locations of large flow deflection. In the mixing tube, the mesh was reasonably fine near the wall with a dimensionless wall distance (y^+) of approximately 13.

Finally, fig. 6.1 implies that radial swirler geometry is slightly more sensitive to an AAI input than an axial swirler geometry. This implication is based on the comparison between R_SW09 and A_SW15, which have nearly equal effective swirl numbers at $\Psi = 0$. For the radial swirler the gradient is slightly steeper compared to the axial swirler, especially for stronger AAI. This suggests that the AAI in the radial swirler has a larger effect on the swirling flow near the walls of the mixing tube. This could be caused by the outlet flow direction of the swirler vane passages. Contrary to the axial swirler geometry, the flow at these outlets has a strong radial component, directed towards the non-swirling jet on the centre-line. This could cause more mixing between the swirling air and the AAI, which ultimately has a larger impact on the effective Swirl number compared to axial swirlers.

6.1.2. Swirl Number Degradation

All Swirl numbers seem significantly lower than the geometric Swirl numbers, but a large part of this is due to the fact that the Swirl number decreases along the axial direction of the mixing tube. This happens due to viscous forces acting on the flow, predominantly decreasing the tangential flow component. This Swirl number degradation is shown for some cases in fig. 6.3.

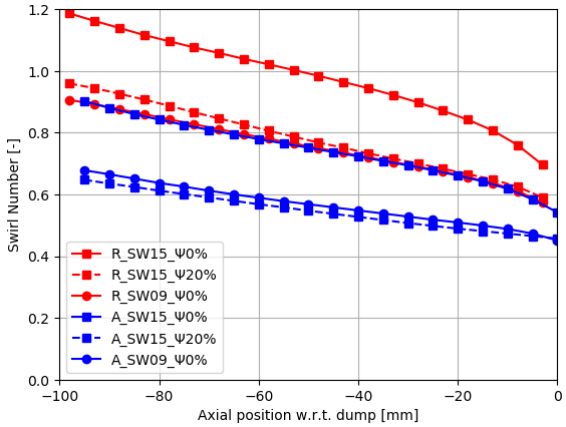

Figure 6.3: Swirl number degradation along mixing tube

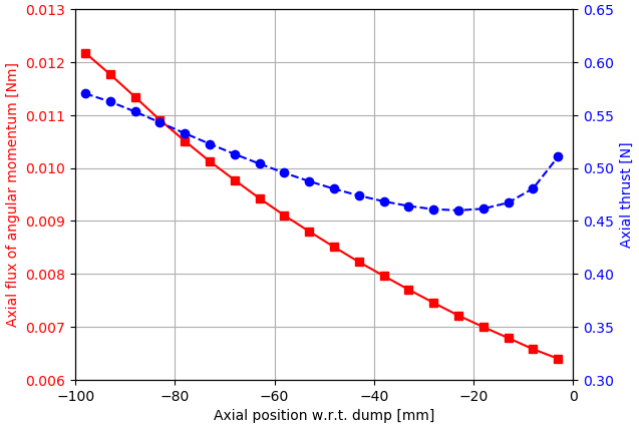

Figure 6.4: $R\_SW15\_\Psi0\%$: G_θ and G_x along mixing tube

This figure shows that the swirl degradation is significant as it decreases by over 40% for the higher geometric Swirl number cases. Even so, the effective swirl numbers at the mixing tube inlet are still well below the expected geometric swirl numbers. This could be explained by the simulation errors discussed above. As mentioned before, this quantitative offset is no reason to worry as the qualitative results are more significant.

Another interesting feature of the swirl degradation is that it appears to be nearly perfectly linear. This makes sense because the encountered viscous friction forces are nearly constant along the mixing tube. The slope also does not seem to be affected by the introduction of AAI, confirming that the Swirl degradation is governed by the wall friction in the mixing tube. The slope of the degradation does seem to become steeper in the final section of the mixing tube. This suggests that the formation of vortex breakdown has an upstream effect on the Swirl number, through the adverse pressure gradient. This drastically changes the axial velocity flow field, which changes the axial thrust (G_x). The development of G_x and G_θ along the mixing tube for $R\_SW15\_\Psi0\%$ is given in fig. 6.4.

It can clearly be observed from this image that the axial flux of angular momentum decreases continuously and gradually along the entire length of the mixing tube, this is due to viscous friction forces between the wall and the swirling flow. The axial thrust similarly degrades gradually along the mixing tube in the first three quarters of the tube. This is consequence of the changing axial velocity profile, which is due to the centre-line void of the AAI tube being filled. However, in the last quarter of the mixing tube the axial thrust increases as the upstream effect of vortex breakdown decelerates the flow on the centre-line. The rise in axial thrust causes a steeper decrease of the Swirl number as seen in fig. 6.3. This reasoning is supported by the swirl degradation of $A\_SW15\_\Psi20\%$ as this is the only case in this figure which does not experience vortex breakdown and its Sw slope remains linear throughout the entire mixing tube.

6.1.3. Flashback Propensity

The investigated metric for flashback propensity in this isothermal study is the axial location of vortex breakdown (VB). Specifically, the upstream stagnation point leading the vortex breakdown. This location was recorded for all simulated setpoints that experience VB in fig. 6.5.

Firstly, fig. 6.5a shows that an increasingly strong axial air injection shifts the stagnation point downstream for all swirler geometries. This is caused by the increase in axial velocity near the centre-line with increasing Ψ. In a reacting case this increased axial velocity will provide more resistance for the flame to travel upstream. Therefore, this trend indicates that the concept of axial air injection works to decrease flashback propensity and thus improves flashback safety.

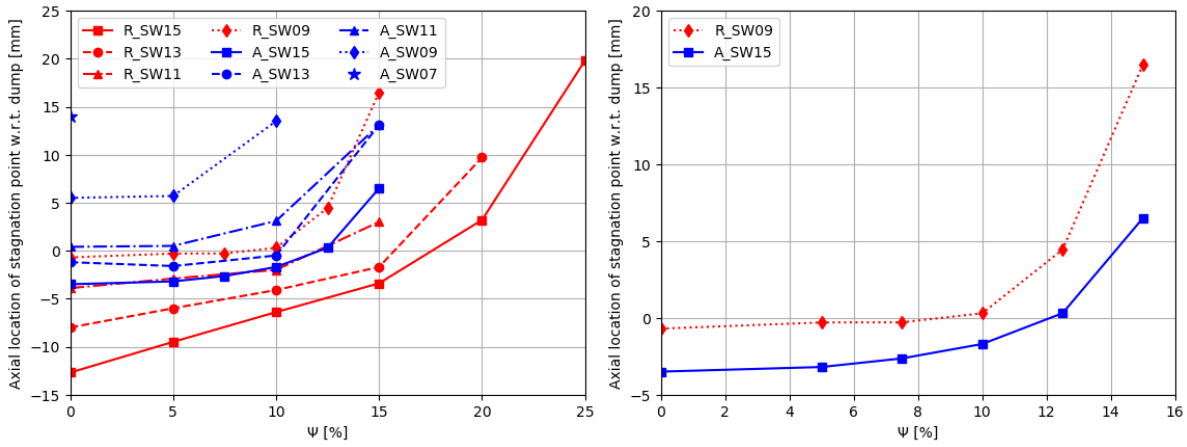

(a) All recorded stagnation points

(b) Close up of axial- and radial swirler with equal swirl intensity

Figure 6.5: CFD: Axial locations of stagnation points vs Ψ

Secondly, the same figure shows that with increasing swirl intensity, the stagnation point of VB shifts upstream. This is only logical because the axial velocity near the centre-line decreases for increasing swirl intensity as is illustrated in fig. 6.6a and fig. 6.6b. Based on this, one could say weaker swirlers are are less likely to experience flashback along the centre-line in reacting cases. This may be true, but a higher swirl intensity has two main advantages: an improved mixing quality because of larger shear forces and an increased stability of the recirculation zones and thus of the flame. This latter advantage is already visible from A_SW07 in fig. 6.6b and fig. 6.6c. The stagnation point is far downstream (indicating flashback safety), but the vortex breakdown is very weak. With only a minor amount of AAI the vortex breakdown is destroyed and no recirculation zone is present anymore. This causes a flow field very similar to a jet being dumped into a plenum, which is equally undesirable as flashback for performance.

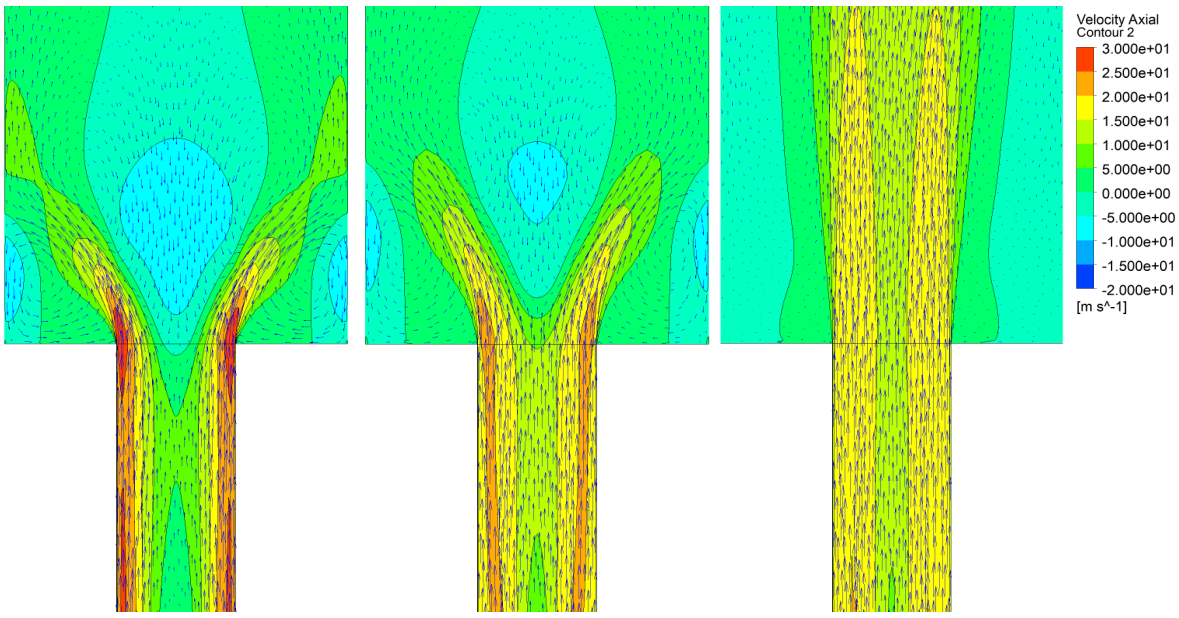

(a) $A\_SW15\_\Psi 0\%$ (b) $A\_SW07\_\Psi 0\%$ (c) $A\_SW07\_\Psi 5\%$

Figure 6.6: Axial velocity fields of mixing tube and combustion chamber at centre-plane

From fig. 6.5a one could be quick to assume axial swirl generators have a more downstream stagnation point than radial swirlers. However this would be wrong, since the legend labels are based on geometric Swirl numbers alone. From fig. 6.1 it was concluded that R_SW09 and A_SW15 have a near identical effective Swirl

number. Therefore, it makes sense to compare these two swirler geometries as shown in fig. 6.5b. From these two curves, the opposite appears true. The stagnation points of the radial swirler lie further downstream than those of the axial swirler. This suggests that the radial swirlers have a lower flashback propensity.

Furthermore, up to $\Psi = 10\%$ the curves are nearly parallel, corresponding to their equal swirl intensity. Beyond that, the stagnation point of the radial swirler shifts slightly further downstream compared to the axial swirler. This agrees with the increased sensitivity of the radial swirler geometry to Ψ shown in section 6.1.1.

6.2. Particle Image Velocimetry

In the experimental campaign the same variables were investigated. The results of that campaign are presented in this section. Specifically, the effect of AAI on swirl intensity is discussed in section 6.2.1. Next, the swirl degradation along the mixing tube is analyzed for a few swirler geometries in section 6.2.2. The, the results regarding flashback propensity based on the axial location of vortex breakdown are presented in section 6.2.3. Finally, in the experimental campaign a brief investigation was also conducted on the effect of fuel momentum on the flow field. These results are presented and analysed in section 6.2.4.

6.2.1. Effective Swirl Number

As described in section 5.5 the determination of the Swirl number required results from both the centre-plane and cross-plane. By mathematically comparing the axial velocity profiles with the tangential velocity profiles of the averaged results, the Swirl number was obtained. All Swirl numbers at 6 mm upstream of the dump are presented in fig. 6.7.

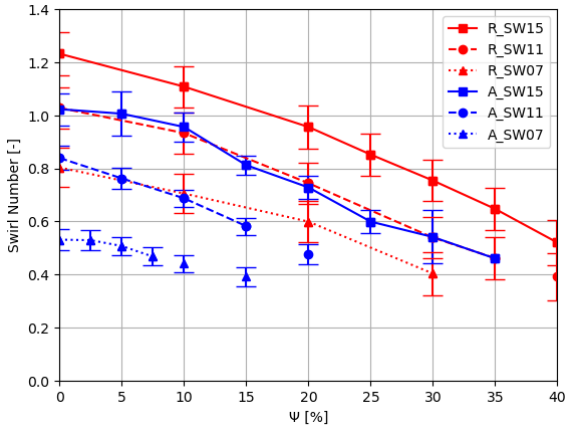

Figure 6.7: PIV: Swirl numbers at $x = -6\ mm$ vs Ψ

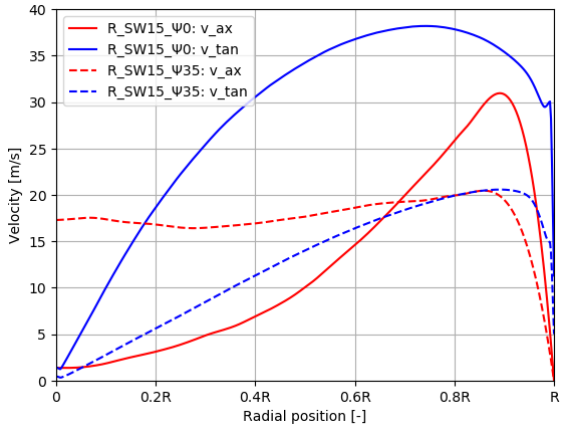

Figure 6.8: Axial- and tangential velocity profiles

Similar to the CFD results, the effective Swirl number decreases with increasing Ψ. This is the consequence of the changing axial- and tangential velocity profiles, which determine the axial fluxes of axial- and tangential momentum. For R_SW15 the two velocity profiles are presented in fig. 6.8 for zero and 35% Ψ. From this figure it can clearly be observed that the axial velocity on the centre-line is increased significantly with the introduction of AAI. To maintain the conservation of mass, the axial velocity near the walls is decreased. As a consequence the axial flux of axial momentum or axial thrust is decreased by 18%. This alone would increase the swirl intensity, but the tangential velocity is also decreased drastically over the entire radius. These tangential velocity profiles also show that the maximum tangential velocity is closer to the wall for the case with AAI. This suggests that the swirling flow is squeezed between the shear layer of the non-swirling jet and the wall. The tangential velocity is still reduced over the entire radius. So the effect of the AAI is not confined to the region near the centre-line alone, but its shearing effect is stronger here than near the wall.

It is not only this viscous effect that causes the Swirl number to decrease with increasing AAI. Another significant cause is the reduction in angular momentum when AAI is increased. For a radial vane swirl generator the angular momentum generated can be easily approximated by considering the vane passage outlets as jet nozzles with a fixed angle and a known mass flow rate through them. When 10% AAI is introduced, the tangential velocity of these jets is reduced by 10%, which reduces the angular momentum by 10% following eq. (6.1).

This same equation was used to calculate the relative angular momentum near the mixing tube outlet at $x = -6\ mm$ for a uniformly assumed density distribution. For varying Ψ the resulting angular momentum relative to the case without axial air injection is presented in fig. 6.9. From this figure it can be observed that the angular momentum reduces nearly 50% more at the outlet of the mixing tube than at the outlet of the swirler. At the outlet of the swirler no viscous effects have started to reduce the tangential velocity and only the inertial effect of reduced angular momentum decreases the Swirl number. At the mixing tube outlet the viscous effects between the AAI jet and the swirling air have further reduced the angular momentum. From this image it can thus be concluded that AAI reduces the Swirl number due to viscous forces and an inertial effect, which is twice as large as the viscous forces.

$$L = I\,\omega = m\,r^2\,\omega = m\,r^2\,\frac{v_{tan}}{r} = m\,r\,v_{tan} \propto \int_0^R (v_{tan}\,\rho\,2\pi)\,dr \tag{6.1}$$

Returning to fig. 6.7, it is also observed that the radial swirl generators have a higher effective Swirl number compared to the axial swirl generators for the same geometric Swirl number. This is in agreement with the CFD results (see section 6.1.1), but to a different extent. From PIV it appears that the effective Swirl number of A_SW15 is nearly identical to that of R_SW11. There is thus some error in the design theory or the designs themselves. This will be further explored in section 6.2.2.

Furthermore, where CFD results suggested the effective Sw of the radial swirlers was slightly more sensitive to a change in Ψ than axial swirlers, PIV results cannot confirm this. Looking at the two swirler types with nearly identical swirl intensity (A_SW15 and R_SW11), no clear distinction can be made in gradients. The effective Swirl numbers are nearly identical for these two swirlers for any value of Ψ. When comparing A_SW11 and R_SW07, which also have similar swirl intensity at $x = -6\ mm$, the opposite implication could be made. From these two curves, the axial swirler model appears to be somewhat more sensitive to AAI than the radial swirler. However, based on all results this difference in sensitivity is determined inconclusive.

A final thing to note from fig. 6.7 is that irrespective of Ψ no vortex breakdown was generated below an effective Swirl number of approximately 0.5 near the dump. From the available result this limit is also independent of the swirler type. Note that not all setpoints in this figure experienced vortex breakdown. Only the data point connected with a line represent a condition where VB was observed. The separate points (for example the points beyond $\Psi = 7.5\%$ for A_SW07) do not generate recirculation zones.

The error bars shown in fig. 6.7 are based on the standard error on velocity caused by averaging 500 images (see eq. (6.2)) and a particle displacement uncertainty of 0.1 pixel since no peak locking was present (see eq. (6.3)) [61]. The Swirl number is calculated using four velocity components so the error increases and becomes more significant. However, the total magnitude is small enough to distinguish between curves. It should be noted that there are more known errors that cannot be quantified like the misalignment of the jet with the centre-line and the data in locations of high reflection.

$$SE_{avg,U} = \frac{\sigma_U}{\sqrt{500}} \tag{6.2}$$

$$SE_{displacement} = \frac{{}^{0.1}/_{Res}}{dt} \tag{6.3}$$

6.2.2. Swirl Number Degradation

The Swirl number degradation was briefly investigated using PIV to get an idea of the effect of a different mixing tube length on the swirl intensity. This required translating the cross-plane laser sheet through the mixing tube to record the tangential velocities. This was done for two different swirler geometries (A_SW15 and R_SW15) with either zero or 20% Ψ. The additional axial locations that were investigated were 86, 66, 46 and 26 mm upstream of the mixing tube dump, besides the standard 6 mm. The results are presented in fig. 6.10.

Note that for the axial swirler case the point at $-86\ mm$ was deleted as the data for the axial velocity was corrupted at this location. Nevertheless, the three cases still show a clear trend. Similar to the CFD results, the swirl degradation is very linear up to the final section of the mixing tube, where the upstream effect of vortex breakdown influences the axial thrust significantly.

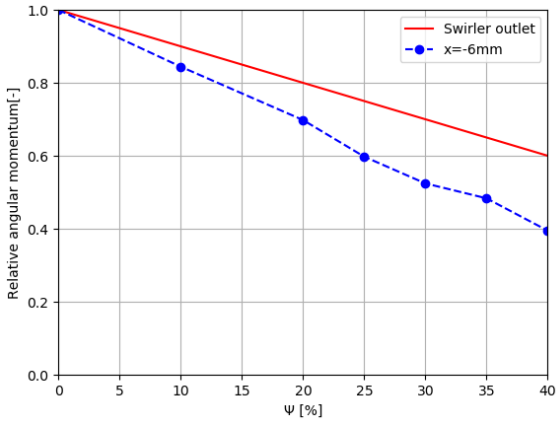

Figure 6.9: PIV: Relative angular momentum at the swirler outlet and at the mixing tube outlet($x = -6\ mm$) for R_SW15

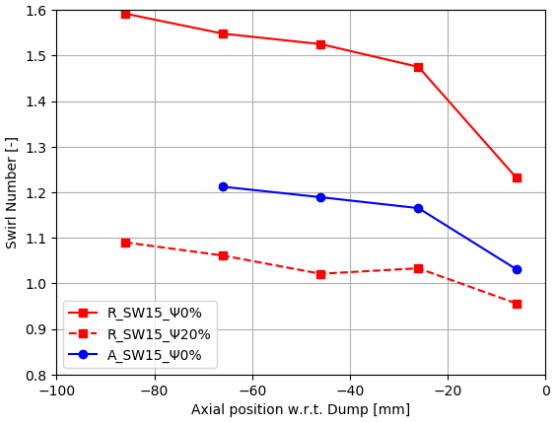

Figure 6.10: PIV: Swirl number degradation along the length of the mixing tube

The magnitude of effective Swirl number close to the swirler exit gives some insight into the accuracy of the theoretical models used for the swirler design. Following the linear degradation further upstream, shows that the radial swirlers actually generate more swirl than they were designed to do. The geometric Swirl number is likely over 1.6 at the swirler outlet plane. On the other hand, the axial swirler generates significantly less swirl than it was designed for. Following the trend, the Swirl number would still likely remain under 1.3 at the mixing tube entrance. This could be the consequence of a few factors. First, between the swirler outlet and mixing tube entrance, a 30 mm long fuel injector is positioned. Even without injecting fuel, this would already degrade the swirl intensity over its length. Although, taking into account the gradient, the Swirl number would not reduce much over the 30 mm (approximately 0.035). Second, the fuel injection itself for the axial swirler acts as four radially impinging jets, which cause a shearing effect and decreases the axial flux of angular momentum and thus the Swirl number. This will be further discussed in section 6.2.4. The final reason for the offset in effective- and geometric Swirl number for axial swirlers is that the tangential velocity component from the outlet plane of the vanes is somewhat smaller than the trailing edge vane angle itself. This is true because the vane passages are not infinitely thin. Especially towards the tip the vanes have relatively large spacing.

6.2.3. Flashback Propensity

The purpose of AAI was to decrease the flashback propensity along the centre-line. The performed experiments in this study were cold flow so flashback itself was not recorded. The metric to evaluate the flashback propensity from cold flow fields was suggested in previous literature: the axial location of the upstream stagnation point of vortex breakdown.

Axial location of stagnation point

The axial location of vortex breakdown was thus recorded for all investigated setpoints. The obtained results from the PIV experiments are presented in fig. 6.11.

The first thing to note from this figure is that generally for increasing Ψ the stagnation point of vortex breakdown shifts downstream, as was expected. However, there are a few exceptions to this trend. The stagnation point of the radial swirler with geometric Swirl number 1.5 shifts downstream slightly when increasing Ψ from zero to 20%. Increasing Ψ further to 25 and 30% appears to break the trend as the stagnation point moves slightly upstream. With even more AAI (Ψ > 30%) the stagnation point shifts significantly further downstream. After investigation it was concluded that the two irregular data points were caused by jet misalignment. This can be seen from the mixing tube centre-plane vector fields in fig. 6.12. The misalignment itself is likely the cause of an unintended channel blockage or reflections in the mixing tube.

The effect of axial air injection on the centre-line axial velocity is evident from the difference between fig. 6.12a and fig. 6.12b. The deficit from the case without AAI is removed for the first 70% of the mixing tube length when 20% AAI is introduced. The axial velocity is increased, but the effect of the AAI barely reaches to the

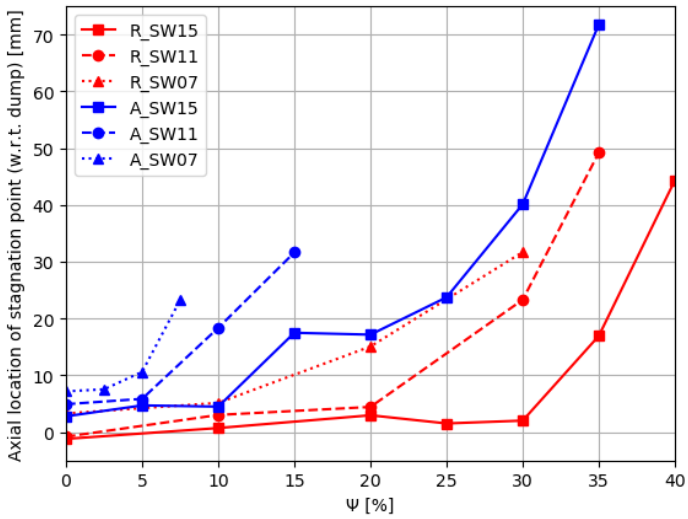

Figure 6.11: PIV: Axial locations of stagnation points vs Ψ

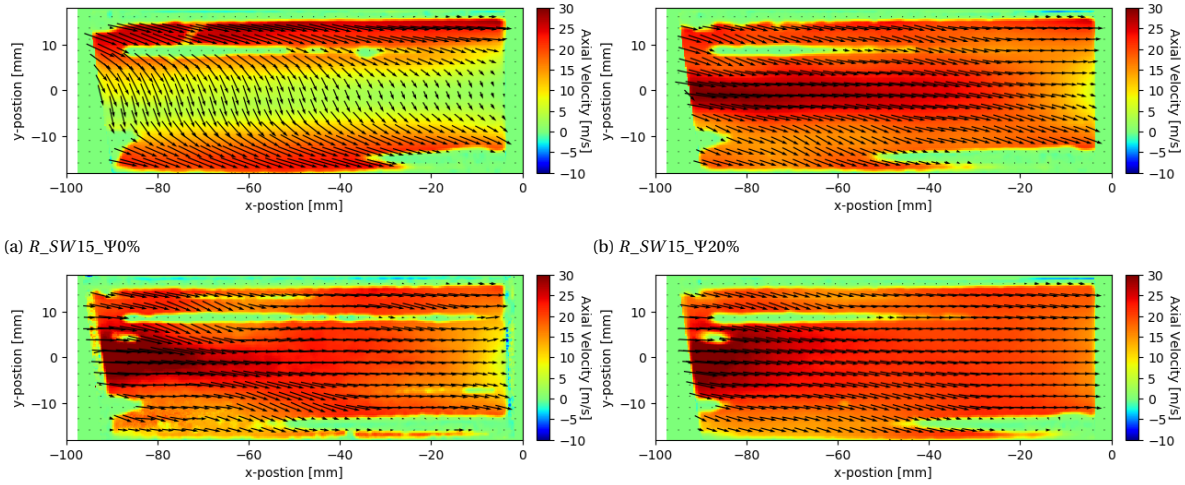

(a) $R\_SW15\_\Psi0\%$ (b) $R\_SW15\_\Psi20\%$

(c) $R\_SW15\_\Psi30\%$ (d) $R\_SW15\_\Psi35\%$

Figure 6.12: Mixing tube centre-plane vector fields

aft part of the mixing tube and thus only slightly affects the location of the stagnation point. The 30% jet (fig. 6.12c) does not have the same effect because it is misaligned and impinging on the bottom wall. As a consequence, the axial velocity profile is quite asymmetrical and the stagnation point is found further upstream than expected. The same is true for the case of $\Psi = 25\%$. It should also be noted that the unexpected upstream movement could also be affected by poor extrapolation of the contour as explained in section 5.5.1. This method was necessary for these data points because the stagnation point lies in the blind spot near the dump. Fortunately, the jet misalignment is virtually removed for higher Ψ. At 35% (fig. 6.12d) the axial velocity deficit is completely removed and the stagnation point shifts significantly downstream. This change in axial velocity profile was already shown in fig. 6.8.

Another anomaly in fig. 6.11 is the stagnation points of A_SW15 at medium AAI strength. At these setpoints the vortex breakdown has a different shape than most other cases. The cross-plane vector fields of the combustion chamber for a few cases are presented in fig. 6.13 for comparison.

In the $\Psi = 10\%$ case (fig. 6.13a) the vortex breakdown causes a central recirculation zone with a most upstream stagnation point very close to the centre-line. This is the flow field that occurred in nearly all of the setpoints with vortex breakdown. However, for the A_SW15 case (andA_SW11 to a lesser extent) the flow

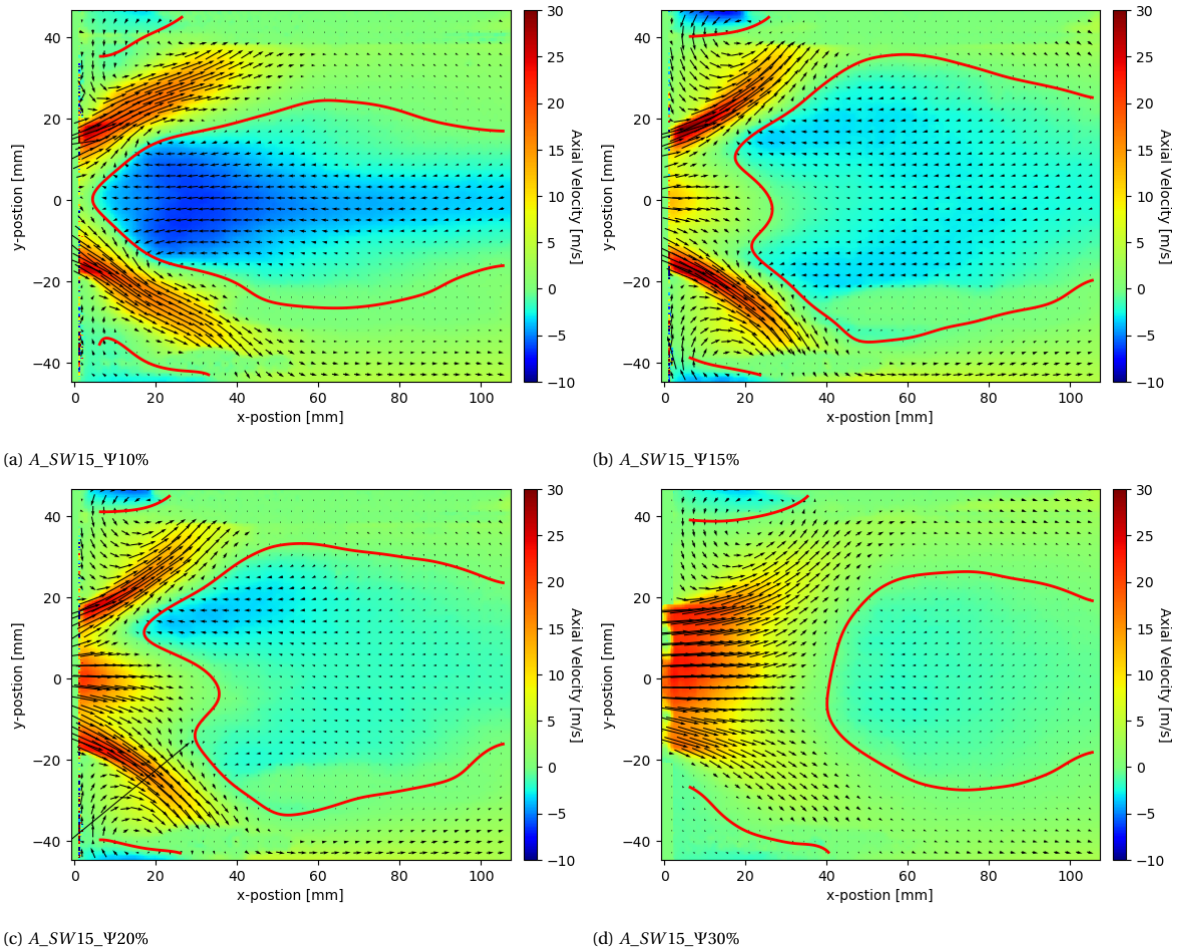

(a) $A\_SW15\_\Psi10\%$

(b) $A\_SW15\_\Psi15\%$

(c) $A\_SW15\_\Psi20\%$

(d) $A\_SW15\_\Psi30\%$

Figure 6.13: Combustion chamber centre-plane vector fields

field developed differently when increasing Ψ further. At $\Psi = 15\%$ (fig. 6.13b) a trident-shaped flow field arises, in which the most upstream stagnation point lies away from the centre-line. It appears that the non-swirling jet does not mix as much with the swirling air as in other cases. This leads to a clearer distinction between the jet and swirling air when the dump is reached. The jet then stays on the centre-line while the swirling air expands and develops into vortex breakdown. For $\Psi = 20\%$ (fig. 6.13c) the flow field is similar but less symmetric. This explains why the stagnation point is found relatively far upstream compared to its neighboring setpoints. The trident profile changes back to the regular bubble vortex breakdown at higher Ψ (fig. 6.13d), before eventually destroying VB all together. As of yet there is no explanations for this reduced mixing interaction between the jet and swirling air for these cases with a trident-shaped velocity profile. The explanation cannot be found in the swirler type geometry because in this study these profiles were only found for some axial swirlers, while T. Reichel found a similar profile for a radial type swirler [70].

In section 6.2.1 it was found that the swirl generators R_SW11 and A_SW15 have nearly identical Swirl numbers for any amount of axial air injection. To compare the difference in effect of Ψ on the stagnation point location between the radial and axial swirlers, these two swirl generators are thus selected. From fig. 6.11 it is observed that the two swirlers are equally sensitive to a change in Ψ, bar the trident-profile anomaly discussed above. Even though, the curves are nearly parallel over the entire range of Ψ there is an offset. This offset is thus unrelated to the value of Ψ, but must be related to the swirler geometry itself. The flow field in the mixing tube for the cases without AAI are presented in fig. 6.14.

A major difference between the two flow fields is clearly visible in this figure. The radial swirler has a significantly lower axial velocity component near the centre-line than the axial swirler. Along the entire mixing tube the axial velocity on the centre-line does not rise above 7 m/s. On the contrary, the axial velocity on the

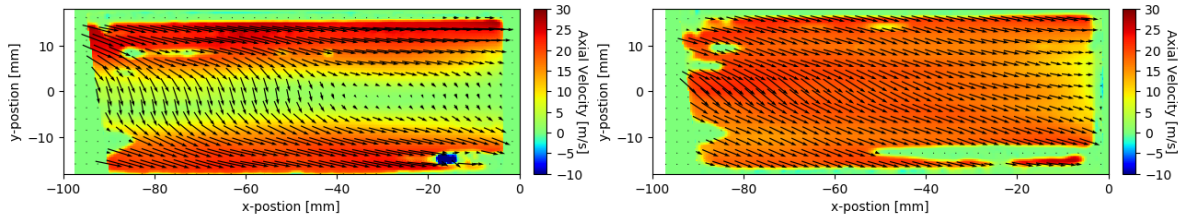

(a) $R\_SW11\_\Psi0$ (b) $A\_SW15\_\Psi0$

Figure 6.14: Mixing tube centre-plane vector fields: axial vs radial swirler

centre-line does not fall below 16 m/s for the majority of the mixing tube of the axial swirler model. In fact, there is hardly any axial velocity deficit on the centre-line. Along nearly the entire length of the mixing tube the axial velocity profile is virtually uniform. Close to the dump, upstream effects start to play a role and the axial velocity profile becomes more pronounced as shown in fig. 6.15.

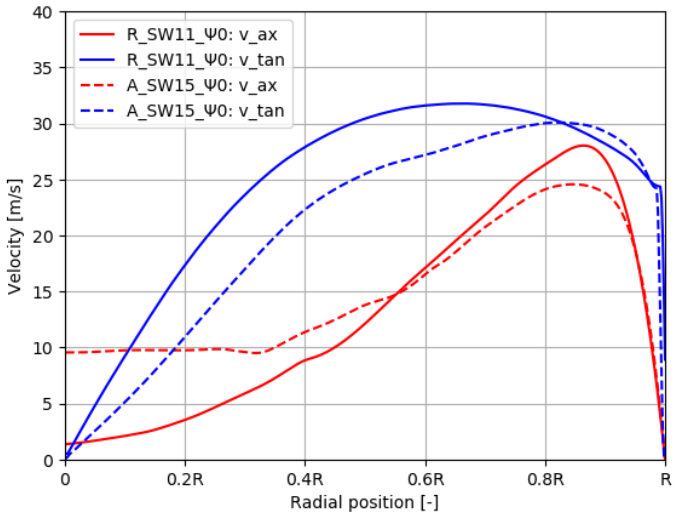

Figure 6.15: Axial- and tangential velocity profiles: axial vs radial swirler

The tangential velocity profiles of the two swirlers are not too different. Both logically have zero tangential velocity at the axis of rotation, but the radial swirler has a larger gradient towards the wall than the axial swirler. Furthermore, the radial swirler has its maximum axial velocity closer farther from the wall, while it is also slightly larger than that of the axial swirler.

The main difference in axial velocity is the value on the centre-line. It is considerably higher for the axial swirler with nearly 10 m/s compared to 1.4 m/s for the radial swirler. The likely cause for this difference is that the outlets of the radial swirler vane passages are located at $r = R$. There is a radial inwards velocity component at this outlet, but it is not strong enough to significantly penetrate to the centre-line. On the other hand, the axial swirler vane passages run from $r = \frac{R}{3}$ to $r = R$. Therefore, a large axial velocity component is also introduced relatively close to the centre-line. The difference in centre-line velocity between the two swirler types translates to a stagnation point location approximately 3.5 mm further downstream. Based on the metric of axial location of stagnation point, the flashback propensity is thus only slightly lower for the axial swirler compared to the radial swirler. However, this metric suggests that the R_SW07 and A_SW15 are nearly equally resistant to flashback. Therefore, the mixing tube centre-plane is presented for this setpoint in fig. 6.16.

The differences between this axial velocity and that of R_SW11 are very minor. On the centre-line the axial velocity is relatively very low. Even at $x = -6\ mm$ the axial velocity is only 1.7 m/s, which is barely higher than that of the radial swirler with a higher geometric Swirl number and much lower than the axial swirler. In a

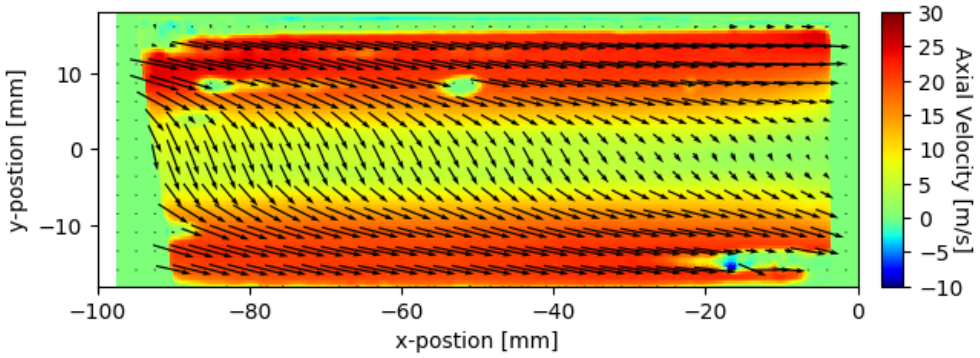

Figure 6.16: *R_SW07_Ψ0%*: mixing tube centre-plane velocity field

reacting case, such a low velocity on the centre-line will probably provide very little resistance to flashback, especially in the case a fast burning fuel like hydrogen is used. Therefore it is decided that the metric of axial location of stagnation point cannot solely be used to compare the flashback propensity of all swirlers, especially not between different swirler types.

Axial velocity at mixing tube outlet

A new metric of flashback propensity is proposed to evaluate the cold flow performance of swirl-stabilised combustors: the axial velocity on the centre-line at the outlet plane of the mixing tube. This metric will also be more stable when switching between non-reacting and reacting flow, than the axial location of vortex breakdown since the conservation of mass- and momentum must be satisfied. For all investigated cases that experienced vortex breakdown this proposed metric was recorded at $x = -6\ mm$ (the most downstream available location in the mixing tube). These results are presented in fig. 6.17. The errorbars on the data points are based on the 0.1 pixel displacement uncertainty and the error introduced by averaging 500 images. The total standard error is given by eq. (6.4).

$$SE_{tot} = \sqrt{SE_{avg,U}{}^2 + SE_{displacement}{}^2} \tag{6.4}$$

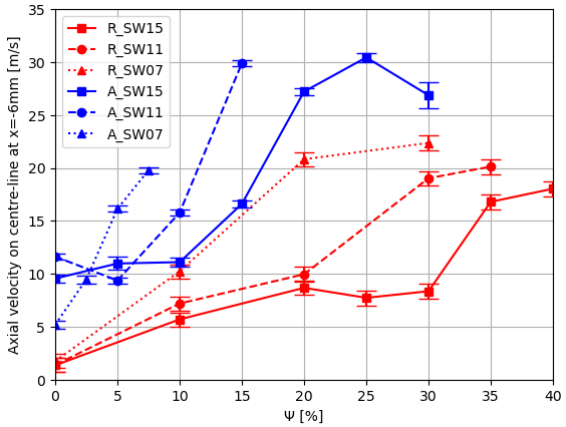

Figure 6.17: Axial velocity on centre-line at $x = -6\ mm$

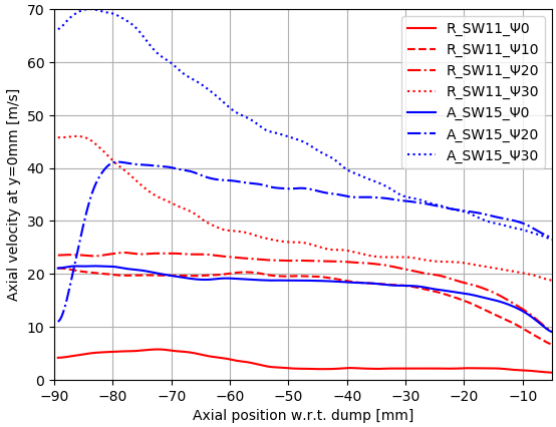

Figure 6.18: Axial velocity profile on centre-line

Based on this new metric, an increased amount of axial air injection still yields a lower flashback propensity. This is no surprise because the axial velocity on the centre-line obviously increases with increasing Ψ. A few exceptions are visible that can be explained by the same reasons as provided for the original metric. The most important difference between the original and new metric is that based on this new metric the axial swirl generators are considerably more resistant to flashback for an equal geometric Swirl number. This is true for the entire range of Ψ. The radial swirlers can reach higher levels of Ψ and still achieve stable vortex breakdown,

but axial swirlers do not require such a strong AAI to reach an equal level of flashback propensity in the first place. Looking at R_SW11 and A_SW15, the axial swirler requires approximately half the level of Ψ to reach the same level of flashback propensity. To further highlight the difference between the axial and radial swirl generators the axial velocity profile on the centre-line is presented in fig. 6.18 for the two swirler types with equal effective Swirl number.

From these axial velocity profiles it is evident that for the same level of Ψ axial swirlers have significantly higher axial velocity on the centre-line. In fact, the axial velocity profile of the axial swirler without AAI is nearly identical to that of the radial swirler with $\Psi = 10\%$. For these setpoints the axial velocity on the centre-line is near 20 m/s for the majority of the mixing tube length. Considering a hydrogen turbulent flame speed in the order of 2 m/s (highly dependent on equivalence ratios and pressure [69],[43]), the potential of AAI to avoid flashback is shown to be great. Note that in fig. 6.18 $A\_SW15\_\Psi10\%$ was excluded as the data in the majority of mixing tube was corrupted. Finally, the initial rise in velocity in $A\_SW15\_\Psi20\%$ is also due to distorted data at the mixing tube entrance. This region does thus not represent reality.

Besides a more realistic differentiation between the flashback propensity of axial and radial swirlers the new metric in fig. 6.17 also shows that even a small amount of axial air injection has a beneficial effect on the flashback safety. Even a relatively weak AAI will increase the axial velocity on the centre-line, while the axial location of vortex breakdown may not change. This is especially evident from the comparison for R_SW15 between fig. 6.11 and fig. 6.17. Following the original metric flashback propensity does not reduce before $\Psi = 35\%$, but based on the new metric the flashback propensity is immediately reduced with a very weak AAI. It is expected that any AAI will help to prevent flashback in reacting environments. Therefore it is advised to adopt the proposed metric as the primary one to determine flashback propensity.

Another conclusion that could be drawn from fig. 6.17 is that higher geometric swirl numbers are more prone to flashback. This also makes sense as the axial velocity deficit on the centre-line is larger for higher swirl intensity. Nevertheless, one should take into account that higher swirl intensity also provides more stable vortex breakdown. So a trade-off has to be made between combustion stability (regarding recirculation zones) and flashback resistance. When designing a swirl-stabilised combustor this cannot be overlooked. For such a combustor design it is advised to minimize Ψ as this degrades the swirl intensity the least. As a consequence, this allows for a swirler design with the lowest possible geometric Swirl number, which generates the least pressure drop.

6.2.4. Effect of Fuel Momentum

A brief investigation was performed into the effect of fuel momentum on the flow field. For radial swirl generators fuel is injected axially at the same plane as the AAI tube outlet. For axial swirlers the fuel is injected radially, 10 mm downstream of the swirler (and AAI tube) outlet. This section will explore the effect of the fuel momentum on the swirl intensity and flashback propensity.

Swirl number

It was expected that the fuel injection in both swirler geometries caused the swirl intensity to decrease since the fuel does not have a tangential component. In fact the fuel jets have a shearing effect that degrades the Swirl number as shown in fig. 6.19.

The decrease in Swirl is thus nearly linear for the radial type swirler and not insignificant. The effective Swirl number at $x = -6\ mm$ decreases by approximately 15% when introducing stoichiometric fuel flow rate compared to no fuel. Unfortunately, there was no data obtained on the centre-plane of axial swirlers. However, the tangential velocity profiles are recorded at $x = -86mm$ and presented in fig. 6.20. The effect of the radial fuel jets is clearly visible as the location of maximum velocity shifts towards the centre-line with increasing fuel momentum. Furthermore, the maximum tangential velocity decreases for all cases. In fact, for the case with axial air injection, the tangential velocity decreases over the entire profile. As a consequence the circulation (area integral of angular velocity [35]) at this location decreases by 11% for the $\Psi = 20\%$ case compared to only 1% for the case without AAI. This can be explained by the fact that swirling flow is squeezed between the AAI and fuel jets. It experiences a large amount of shear force and decelerates as a consequence.

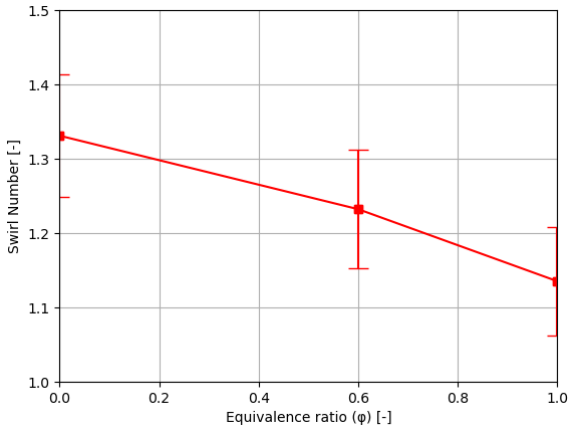

Figure 6.19: $R\_SW15\_\Psi0\%$: effect of ϕ on Sw at $x = -6\ mm$

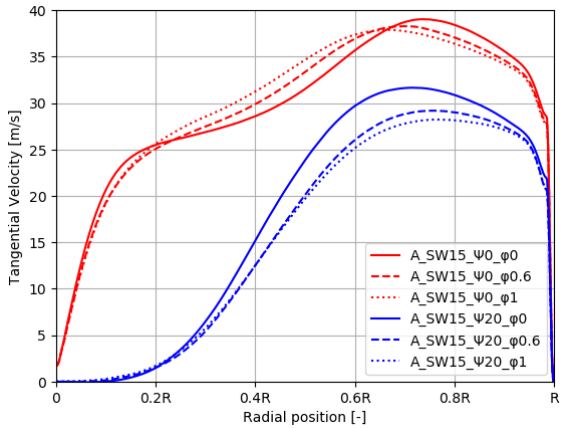

Figure 6.20: A_SW15: tangential velocity profiles for varying ϕ

Flashback propensity

Regarding flashback propensity, it was expected that the fuel injection in radial swirlers caused the low axial velocity on the centre-line since the distributed fuel jets form a shear layer separating the outside swirling air with the inside AAI (or void in case $\Psi = 0\%$). The axial velocity fields in the mixing tube are presented in fig. 6.21 for $R\_SW07\_\Psi0\%$ for varying fuel momentum.

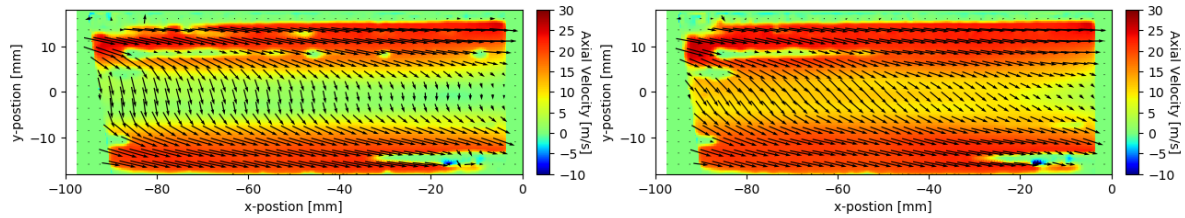

(a) No fuel ($\phi = 0$)

(b) Stoichiometric fuel ($\phi = 1$)

Figure 6.21: $R\_SW07\_\Psi0$: Mixing tube centre-plane vector fields: effect of fuel momentum

Figure 6.21a shows that the axial fuel injection does not cause the void near the centre-line since the axial velocity is even lower near the centre-line when no fuel is injected. In fact, the fuel jets appear to fill the void when no axial air is present, which suggests that increased fuel momentum decreases the flashback propensity. This was confirmed by fig. 6.22 and fig. 6.23, which present the effect of fuel momentum on the original and new metrics for flashback propensity.

Both metrics suggest that fuel momentum helps to reduce flashback propensity. For both metrics the effect is slightly larger when the effective Swirl number is lower, but significantly larger for cases where AAI is introduced. Similar results were also observed by Reichel et al. in Berlin [71]. This larger sensitivity in the $R\_SW07\_\Psi20\%$ case implies that the fuel jets do form a shielding layer between the axial air and swirling air as was expected. This layer causes the axial air jet to be disrupted less, which leads to a higher axial velocity at the mixing tube exit and ultimately to a reduced flashback propensity. However, another important effect of increased fuel momentum should be taken into account: the increased flame speed for equivalence ratios closer to unity. Even though the axial velocity on the centre-line may increase this positive effect on flashback resistance may be overcome when the hydrogen flame speed increases more. Therefore the turbulent flame speed of hydrogen for varying equivalence ratio as found by Morones [58] is overlain with the axial velocities on the centre-line as found by PIV. These results are presented in fig. 6.24.

From this figure it can be observed that the increase in turbulent flame speed is of similar magnitude as the increase in axial velocity of the flow. For higher Swirl numbers, increased equivalence ratio (and thus fuel momentum) causes barely any net effect on the flashback propensity. For lower Swirl numbers, the increased

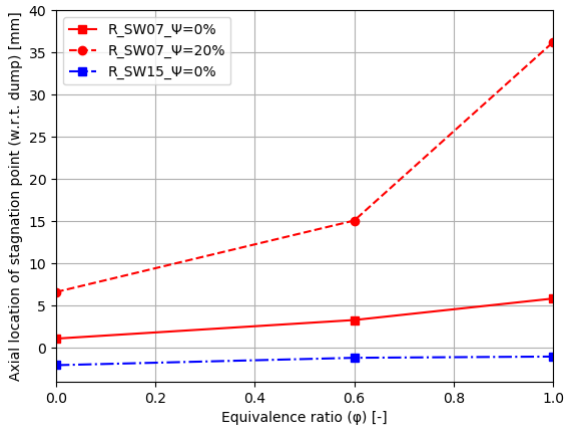

Figure 6.22: Effect of ϕ on axial location of stagnation point

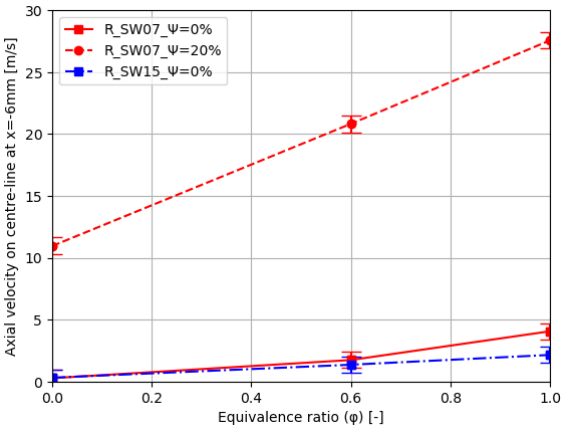

Figure 6.23: Effect of ϕ on axial velocity on centre-line at $x = -6\ mm$

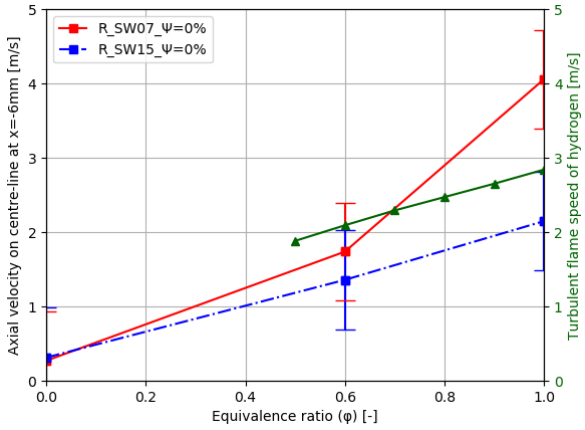

Figure 6.24: Effect of equivalence ratio on axial velocity on the centre-line at $x = -6\ mm$ and on the turbulent flame speed of hydrogen

axial velocity appears to outweigh the increase in flame speed, yielding a positive net effect on the flashback resistance. It should be noted that the turbulent flame speed of hydrogen is highly dependent on the flow characteristics, among which the level of turbulence. The increase in flame speed with equivalence ratio could thus be different for this combustor model in reacting conditions than is projected in fig. 6.24. Nevertheless, this data provides a ballpark figure and shows the increased flame speed cannot be ignored.

Based on the explanation that the axial velocity on the centre-line increases with increased fuel flow because of the shielding effect of the fuel layer, axial swirlers could be negatively influenced by increased fuel momentum with respect to flashback propensity. For these swirler geometries the radial fuel jets will probably cause more interaction between swirling air and axial air, disturbing the non-swirling jet on the centre-line. The increased flame speed then likely dominates and further contributes to an increased flashback propensity.

6.3. Comparison: PIV vs CFD

In this section the similarities and differences between the numerical and experimental results are highlighted. The effective Swirl numbers for varying Ψ from both PIV and CFD results are presented in fig. 6.25. The major difference between the PIV and CFD results is a significant offset in magnitude. With no axial air the R_SW15 swirler has a 67% higher effective swirl number than was expected by the CFD simulations. For its axial counterpart this offset is even larger with 74%. For lower geometric Swirl numbers the offset is less extreme but still very significant: 45% and 27% for the R_SW07 and A_SW07 respectively. This considerable offset is likely caused by averaging errors and approximations in the solving of RANS equations. Other factors like the mesh quality could also play a significant role as mentioned in section 6.1.

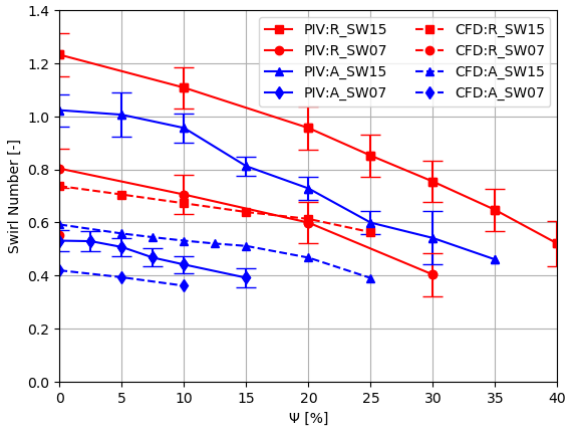

Figure 6.25: Effect of Ψ on Sw for PIV and CFD

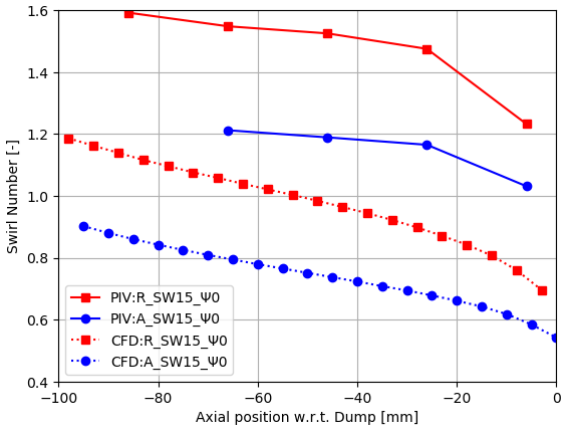

Figure 6.26: Swirl number degradation for PIV and CFD

On the other hand, the gradients are quite similar in the sense that they are all nearly linear irrespective of the swirler type. However, there is a small variation in the actual slope between CFD and PIV. The effect of Ψ on the Swirl number is slightly larger in reality than was expected from CFD. This slight under-prediction in sensitivity is likely caused by the same averaging errors as mentioned before.

Another similarity between CFD and PIV can be found in the swirl degradation along the mixing tube as presented in fig. 6.26. From this figure can be observed that the offset in effective Swirl number already originates before entering the mixing tube. The relative offsets between CFD and PIV hardly change along the mixing tube length. This implies that the viscous forces that decelerate the tangential velocities are properly solved in the CFD simulations.

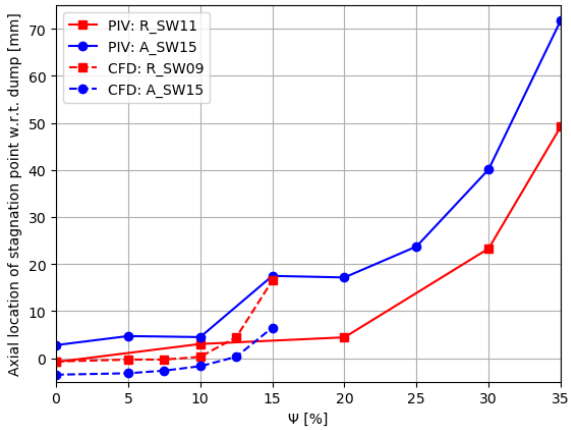

Figure 6.27: Effect of Ψ on axial location of stagnation point for PIV and CFD

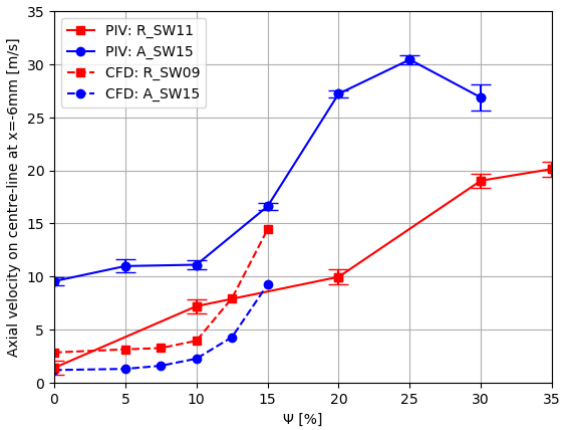

Figure 6.28: Effect of Ψ on axial velocity on centre-line at $x = -6$ for PIV and CFD

The significant offset in effective Swirl number magnitude translates to a similar difference in flashback propensity. The flashback propensity based on the original and new metric is presented fig. 6.27 and fig. 6.28 respectively. Figure 6.27 shows that the effect of AAI on the axial location of stagnation point is over-predicted considerably by CFD. Vortex breakdown is not sustained above Ψ = 15% for either axial or radial swirler, while PIV showed VB was sustained up to Ψ = 35%. This is likely a result of the under-prediction in effective Swirl number by CFD. It is interesting to note that CFD did not predict a flow with vortex breakdown with a stagnation point further downstream than 17 mm or a centre-line axial velocity above 15 m/s near the mixing tube outlet, while PIV showed VB with stagnation points up to 71 mm downstream of the dump or double the axial velocity on the centre-line. This difference can be similarly attributed to the Swirl number predictions.

A difference independent of the Swirl number prediction is the offset between axial and radial swirlers. Interestingly CFD results suggested that for the same effective Swirl number (R_SW09 and A_SW15) the radial swirler has a more downstream stagnation point as well as a higher axial velocity on the centre-line at $x = -6$ than the axial swirler. This implied radial swirlers had a lower flashback propensity. This is the opposite of what the PIV results showed. From those results, it was concluded that axial swirlers are less prone to flashback for equal effective Swirl numbers (R_SW11 and A_SW15). This disagreement is likely a consequence of the prediction of axial velocity near the centre-line. From fig. 6.6a it can be observed that the axial velocity for the axial swirler is simulated to be much lower than was found with PIV. For the PIV case, which even had a considerably higher effective Swirl number, there was hardly any centre-line velocity deficit observed, while this void clearly is predicted by CFD.

Ultimately, the experimental results should be considered leading. So conclusions with respect to the flow field, will be drawn based on the PIV data.

7

Conclusions

The aerospace industry is looking for propulsion- and power alternatives to traditional gas turbine aero-engines that burn kerosene. This research is driven by emission regulations that become ever stricter in order to reduce global warming. Breakthroughs in this field of research could have a major impact as civil aviation is a significant contributor to greenhouse gas emissions. A potential alternative fuel that completely eradicates CO2 emissions is hydrogen. Hydrogen combustion does still emit NOx, but these gasses can be significantly reduced by thoroughly mixing the fuel with the oxidant before combustion (lean-premixed combustion). A concept that can achieve this is the swirl-stabilised combustor. In this concept a swirling air flow is used to mix with the fuel in a mixing tube before the flow expands in a larger combustion chamber, forming recirculation zones. These recirculation zones are crucial for the combustion stability and performance. The primary weakness of this combustor concept is that the flow has a low axial velocity near the centre-line of the mixing tube. This feature makes the concept prone to the upstream propagation of the flame or 'flashback', which can be damaging to the upstream components.

To prevent flashback in the swirl-stabilised combustor the axial air injection (AAI) concept was introduced recently [70]. In this concept a third flow is added next to the fuel and swirling air (generated by a radial vane swirler). The additional flow is inserted as a non-swirling jet of air on the centre-line of the mixing tube. This jet increases the axial velocity component of the flow on the central axis in an attempt to prevent the flame from propagating upstream. The flashback propensity in non-reacting tests was measured by the axial location of stagnation point leading the central recirculation zone. The initial results of the axial air injection concept were encouraging. Therefore this study wishes to complement to the research into AAI. In this study the effects of axial air injection and swirl intensity on the flashback propensity were investigated by means of a CFD analysis and an experimental campaign in the form of PIV.

In order to conduct the experiments a combustor model, suited for cold flow, was designed and produced with variable AAI quantity. The design was also kept modular so that different types and different intensity swirl generators could be interchanged. The completed models were also converted into meshed CFD domains for a number of steady-state RANS simulations.

The results from the CFD campaign showed that effective swirl intensity is significantly reduced by the axial air injection. This is a consequence of the strong shearing effect between the AAI and the swirling air. The results also showed that the effective Swirl number produced by the radial swirl generator was slightly more sensitive to a change in AAI. On the other hand the swirl degradation through the mixing tube was nearly identical between swirler types and also appeared independent of AAI. On the other hand, a large difference between the two swirler types was seen in their location of the stagnation point. The axial swirler type showed a consistently further downstream stagnation point than the radial swirler for all investigated fractions of applied AAI. From the CFD results it can thus be concluded that AAI does have a positive effect on the prevention of flashback. Furthermore, this effect is similar for both axial and radial swirlers, but axial swirlers already have a considerably further downstream stagnation point when no AAI is applied. This makes axial swirlers less prone to flashback than radial swirlers, irrespective of the amount of applied AAI.

The PIV results showed a very similar behaviour regarding the effect of AAI on the swirl intensity. Contrary to CFD, from the PIV results no difference in sensitivity was observed between the two swirler types. Another conclusion to be drawn from the effective Swirl numbers is that vortex breakdown does not occur for a Swirl number lower than 0.5 at the mixing tube exit. This statistic is independent of AAI and swirler type. On the other hand, the axial velocity on the centre-line was found to be highly dependent on the AAI, as was expected. This lead to a downstream shift of the stagnation point with increasing AAI, in agreement with the CFD results. The sensitivity similarity between axial and radial swirlers was also very analogous to the CFD results. However, different to CFD was the axial location of the stagnation point for higher Swirl number cases, which hardly changed. From PIV results the effect of axial air injection only appeared to have a significant effect on the axial location of the stagnation point for a large fraction of AAI. Based on this metric it was concluded that the flashback propensity is hardly affected for cases with high Swirl numbers and that the flashback propensity of axial swirlers was lightly lower than for radial swirlers. However, the centre-plane velocity fields of radial and axial swirlers were found to be vastly different with a much higher axial velocity on the centre-line for axial swirlers. Therefore a new metric for the flashback propensity was proposed: *"the axial velocity on the centre-line at the mixing tube exit"*.

This new metric was also presented for all investigated cases. Based on this metric it was shown that even a small amount of AAI does contribute to the flashback safety and that there is a significant difference between the axial- and radial swirler flashback propensity.

Furthermore, the effect of fuel momentum on the swirl number and flashback was also investigated from which it was concluded that increased fuel flow decreases the effective Swirl number due to increased shear and that increased fuel flow decreases the flashback propensity as the axial velocity on the centre-line is increased and the stagnation point is further downstream.

To summarise the conclusions, the research questions formulated in section 2.11 are answered below.

- **What is the effect of the axial air injection on the flashback propensity?**
  Axial air injection increases the axial velocity near the centre-line over the entire mixing tube. Even a small amount of axial air injection causes an increase in axial velocity on the centre-line at the mixing tube exit. For example a velocity of 1.3 m/s there was increased to 6.7 m/s by applying 10% AAI. Any gained velocity at this location provides more resistance to a flame propagating upstream. Therefore AAI decreases flashback propensity.

- **What is the effect of the Swirl number on the flashback propensity?**
  An increased swirl intensity inherently has a lower axial velocity on the centre-line. As a result more AAI has to be applied to achieve similar axial velocity. Therefore a higher Swirl number increases the flashback propensity. However a higher Swirl number also provides higher combustion stability, which is crucial.

- **What is the difference in flashback propensity between axial vane swirl generators and radial vane swirl generators?**
  Axial swirl generators have a considerably higher axial velocity near the centre-line for any AAI compared to radial swirl generators. For example a radial swirler with 20% AAI has nearly equal axial velocity on the centre-line at the mixing tube outlet as an axial swirler with no AAI. Therefore the axial swirler has significantly lower flashback propensity.

- **How much does the Swirl number decrease along the mixing tube?**
  In PIV the 100 mm long mixing tube used in this study lead to a decrease in Swirl number from approximately 1.6 to 1.2, a 25% decrease for the radial swirler with highest geometric swirl number. In CFD this same swirler had it Swirl number reduced from by nearly 40% (from 1.2 to 0.7).

- **What is the difference between the geometric Swirl number and the effective Swirl number for axial- and radial swirlers?**
  In PIV the radial Swirl number was measured to be 1.6 at the mixing tube inlet whereas its geometric Swirl number was calculated at 1.5, an under-prediction of 0.1. For the axial swirler with geometric Swirl number 1.5 the most upstream location where the Swirl number was obtained is at 34 mm downstream

of the mixing tube inlet, which is another 30 mm downstream of the swirler exit. Here it was measured to be just above 1.2. This may have been close to 1.3 at the swirler outlet, which would still be 0.2 less than the geometric Swirl number. Note that the uncertainty of this last statement is relatively large.

- **What is the effect of fuel momentum on the Swirl number?**
  Additional fuel momentum degrades the tangential velocity, which translates to a reduced axial flux of angular momentum and thus a reduced Swirl number. For radial swirlers this effect caused a decrease in Swirl number from 1.33 to 1.14 (−15%) for an increase from no fuel to effectively stoichiometric fuel.

- **What is the effect of fuel momentum on the flashback propensity?**
  Additional fuel momentum increases the axial velocity on the centre-line and thus decreases flashback propensity. For radial swirlers the effect is amplified with increasing AAI, because the fuel jets form a separating layer between the non-swirling jet on the centreline and the swirling air coming in from the vane passage outlets at the wall. This causes the AAI jet to degrade less over the length of the mixing tube, improving flashback safety.

8

Recommendations

In this chapter the research is reflected upon and points are highlighted that could improve this study if it were to be repeated. Additionally, advice for future research that could complement this study is provided. This advice is aimed towards developing this swirl-stabilised combustor concept into an actual aircraft propulsion- and power unit.

8.1. Research Reflection and Improvement

- **CFD mesh**
  The mesh quality for the domains in this study was decent but could be further improved. A first step would be to refine the mesh at areas of major flow deflections. A more refined mesh inside the swirler vane passages for instance would more accurately capture the flow deflections created by the swirl generators. Furthermore, a more refined wall region would more accurately capture the viscous effects in the boundary layer. This would lead to a smaller y-plus than 13 which was currently obtained over the mixing tube walls.

- **Axial air injection tube**
  The AAI tube that was used was 3D printed and integrated in the swirl generators. It was 10 diameters long, which makes it valid to assume a fully developed flow at the exit of the tube. However, any error there could be reduced by simply elongating the tube. Furthermore the tube could also be improved by making it more rigid. During the experimental campaign it was observed that the flow field was quite sensitive to any tube deformation. If the tube was bent in any direction, the exiting jet would have an offset angle w.r.t. the centre-line, which had a significant impact on the velocity field.

- **Axial swirler fuel injector**
  The fuel injection of the radial swirler was designed for a specific momentum flux ratio from which the mass flow rate of the fuel stream was derived. This mass flow rate was also used for the axial swirler fuel injector. However this fuel flow was distributed over four larger holes in stead of 16 smaller holes. Therefore the momentum flux ratio of the fuel between the radial and axial swirler was not conserved. To conserve this properly, the axial fuel injection should be similarly well distributed over 16 holes of equal diameter as was designed for the radial swirler.

- **Axial swirler effect of fuel momentum**
  Related to the fuel injector is the effect the fuel momentum has on the flow field. This was not properly investigated for the axial swirl generators as no centre-plane measurements were taken for varying fuel due to limited time available for the experiments. It would be interesting to investigate this fuel momentum effect on the axial velocity profile, especially to see if it is the radial velocity component of the fuel injection which fills the mixing tube centre-line void seen in radial swirlers.

- **Boundary layer thickness inside mixing tube**
  For the axial velocity component the boundary layer region of the mixing tube was not accurately captured. The profile of the velocity here was unknown, but currently generated to comply with the conser-

vation of mass. This profile shape could be improved if a second requirement was added. For example, the boundary layer thickness could be estimated using empirical relations. This could change the velocity profile to a more realistic shape and therefore improve the accuracy of the calculations based on the velocity profile.

- **Effect of Hysteresis**
  Vortex breakdown is a process with a strong hysteresis effect (see section 2.5.4). In this study the mass flow rates of the AAI and swirl air were increased in the same order for all setpoints. Therefore the effect of hysteresis is excluded, but not investigated itself. Reaching the setpoints again by switching the order of the air mass flow streams around would likely yield a slightly different velocity field. The difference between the two velocity fields would define the hysteresis effect. Understanding the magnitude of this hysteresis effect could have a significant impact on the operability of the combustor.

- **Uncertainty Quantification**
  The uncertainty in the PIV experiments was currently quantified for velocity based results from the standard error caused by pixel displacement uncertainty and the standard error caused by averaging 500 images. This uncertainty could be expanded by the standard error caused by camera noise and image scaling. Furthermore the uncertainty on position based results could also be quantified based on similar factors.

8.2. Recommendations for Future Research

- **Variable axial air injection diameter to control velocity**
  For the current study a fixed diameter AAI tube was applied. The AAI magnitude was varied by changing the mass flow rate. This obviously increased the axial velocity component on the centre-line. However, this velocity could also be adjusted by maintaining a constant mass flow through the AAI and changing its diameter via a variable orifice for instance. This could generate even higher axial velocity components on the centre-line with less mass flow through the AAI tube. Consequently, the variable diameter AAI could potentially lead to less degradation of swirl intensity by the AAI for the same reduced flashback propensity.

- **Reacting flow CFD simulations**
  So far the flow field has only been investigated for isothermal flow. Designing and producing a combustor suitable for the high temperatures realised in combustion is significantly more costly than the isothermal combustor model used for this study. Therefore it is highly recommended to first conduct reacting flow CFD to get an idea of how the isothermal flow field would translate to a reacting flow field and what magnitude of thermal gradients can be expected.

- **Reacting flow field experiments**
  Before conducting the reacting flow experiments with the intended hydrogen, it is advised to first conduct experiments with methane (CH4). This gas is more readily available for experiments and is easier to control and predict than hydrogen. Once a level of confidence is reached on the behaviour of the reacting flow field, hydrogen can be used as the fuel.

- **Mixing quality investigation with hydrogen**
  Another important part of the swirl-stabilised hydrogen burner is the mixing quality. The better this mixing quality is, the lower are the NOx emissions. The mixing quality could be determined from reading the NOx emissions of the reacting flow combustor. However it is recommended to conduct an isothermal mixing quality investigation as well to exclude any other variables influencing the NOx emissions.

- **Mixing tube length variation**
  Also related to the mixing quality is the length of the mixing tube. Its length could be varied to investigate the effect on the mixing quality, but also on the AAI effectiveness and swirl degradation. A shorter mixing tube will ensure less swirl degradation and will have a higher axial velocity on the centre-line, but will have lower mixing quality. Furthermore, the mixing tube should not be too long to avoid autoignition. There will probably be an optimal mixing tube length that gives the desired mixing quality and optimizes the effect of AAI.

- **Dilution holes implementation (to prevent boundary layer flashback)**
  The flashback propensity investigated so far is the vortex breakdown induced flashback on the centreline. However, the flow velocity in the boundary layer is also very low locally. At certain conditions this could result in boundary layer flashback. To avoid this boundary layer dilution holes, which blow air along the boundary layer, could be introduced in the mixing tube walls to lean out the boundary layer.

- **Combustor geometry optimisation**
  Once all combustor parameters are sufficiently understood, the geometry of the combustor can be optimised. Parameters like the combustion chamber diameter to mixing tube diameter can be optimised as well as the actual shape of the expansion zone. Furthermore, swirl generator vanes could also be aerodynamically optimised to produce the desired swirl intensity for minimum pressure drop.

A

Technical Drawings

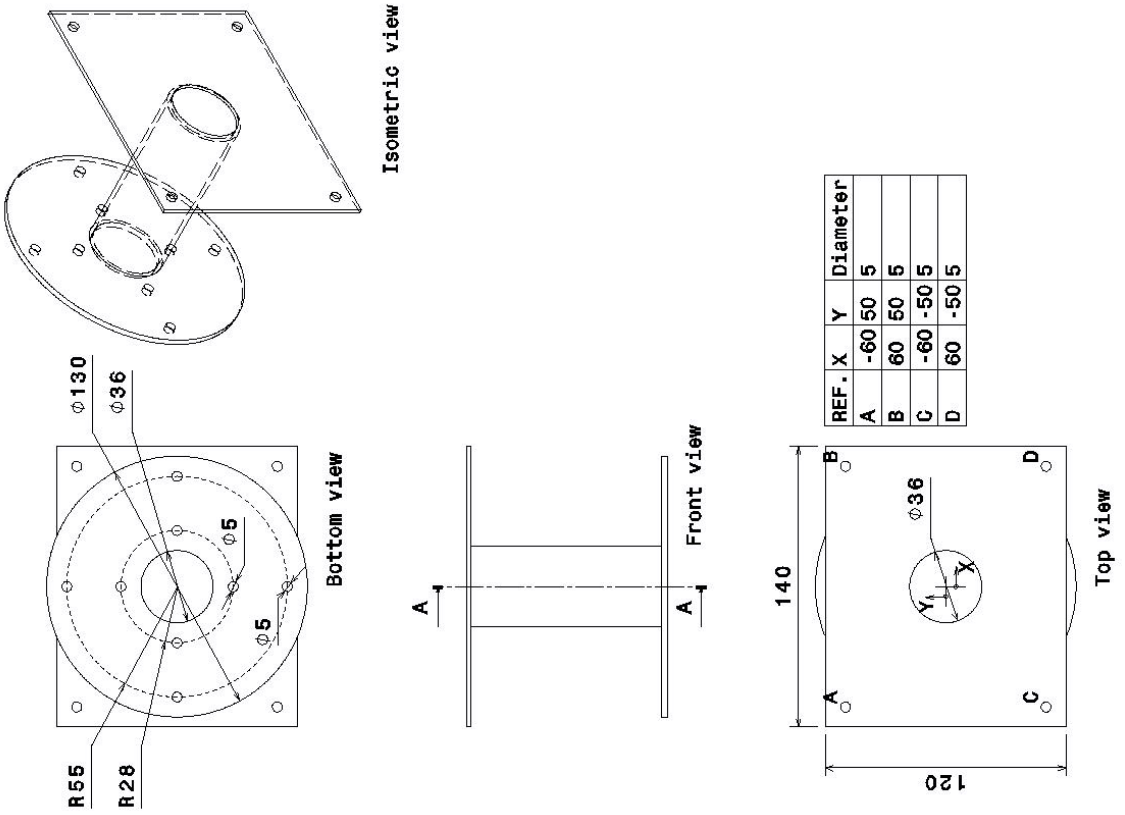
Isometric view
Bottom view
Front view
Top view
Section view A-A
Mixing Tube
ϕ130
ϕ36
ϕ5
R55
R28
140
120
100
95
130
40
36
2
5
3
REF. X Y Diameter
A -60 50 5
B 60 50 5
C -60 -50 5
D 60 -50 5

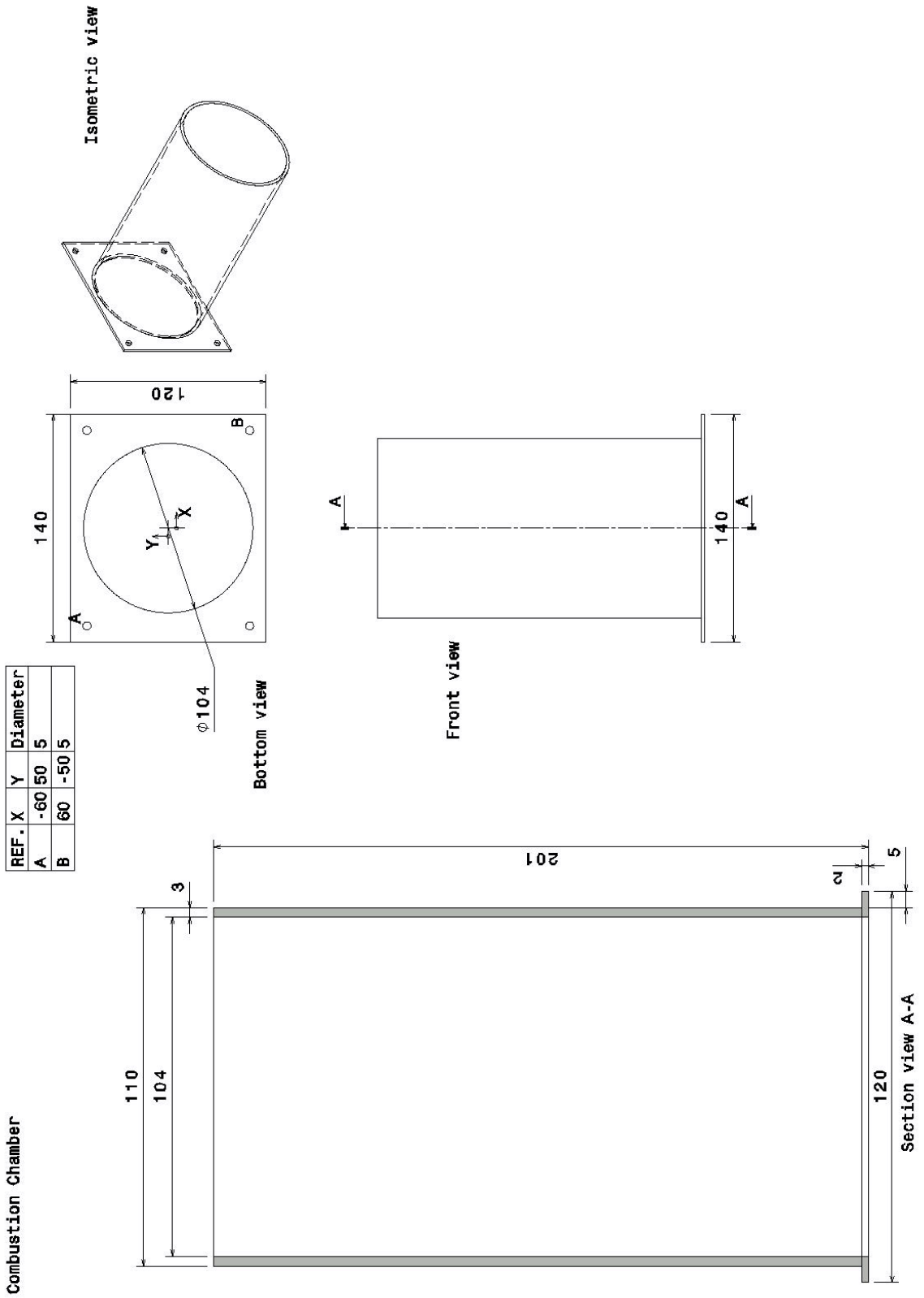
Isometric view
120
140
A
B
X
Y
ϕ104
Bottom view
A
A
140
Front view
REF. X Y Diameter
A -60 50 5
B 60 -50 5
201
2
5
3
110
104
120
Section view A-A
Combustion Chamber

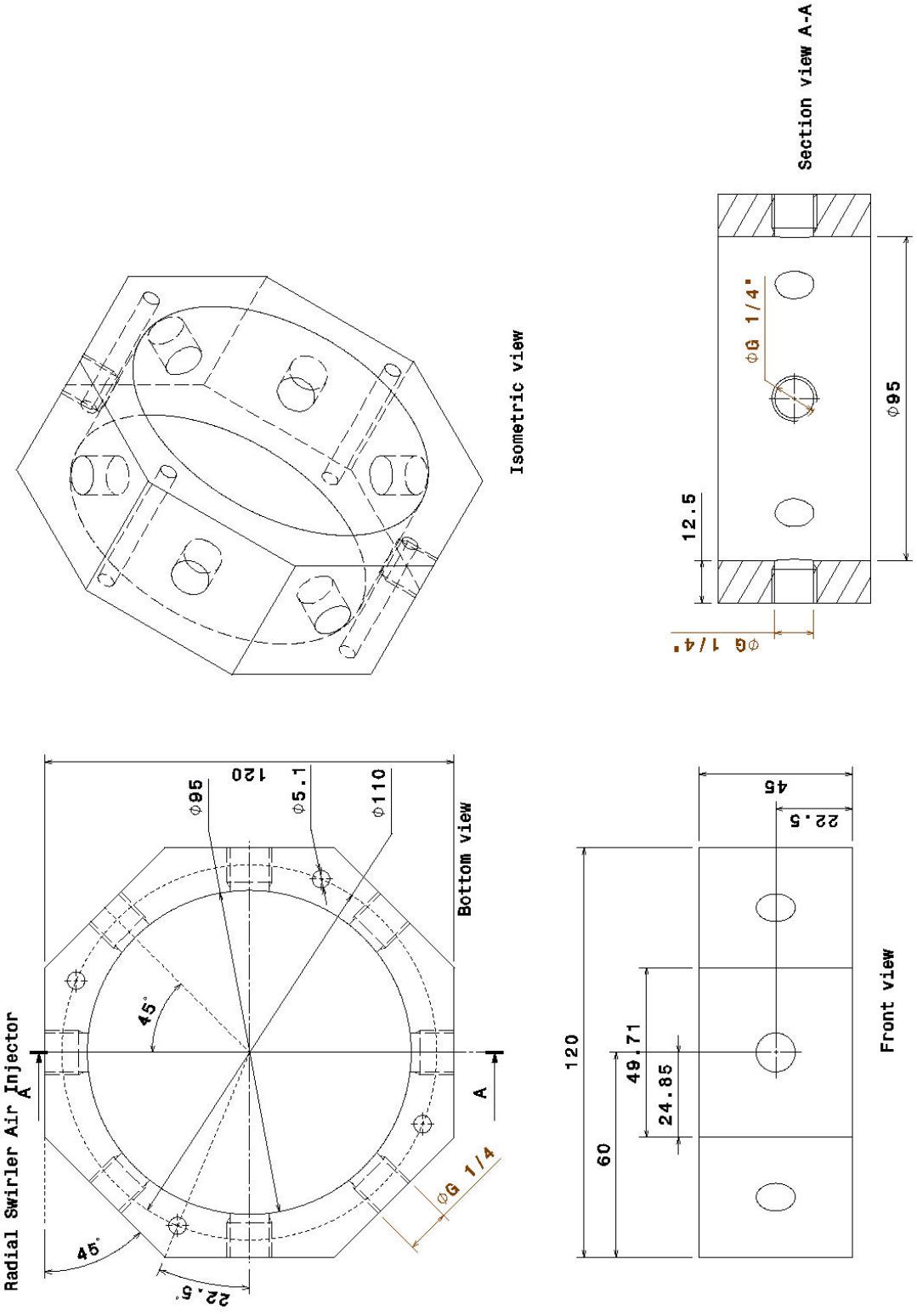
Section view A-A
ΦG 1/4"
Φ95
12.5
ΦG 1/4"
Isometric view
Bottom view
Φ95
120
Φ5.1
Φ110
45°
A
A
ΦG 1/4
45°
22.5°
Radial Swirler Air Injector
Front view
45
22.5
120
60
49.71
24.85

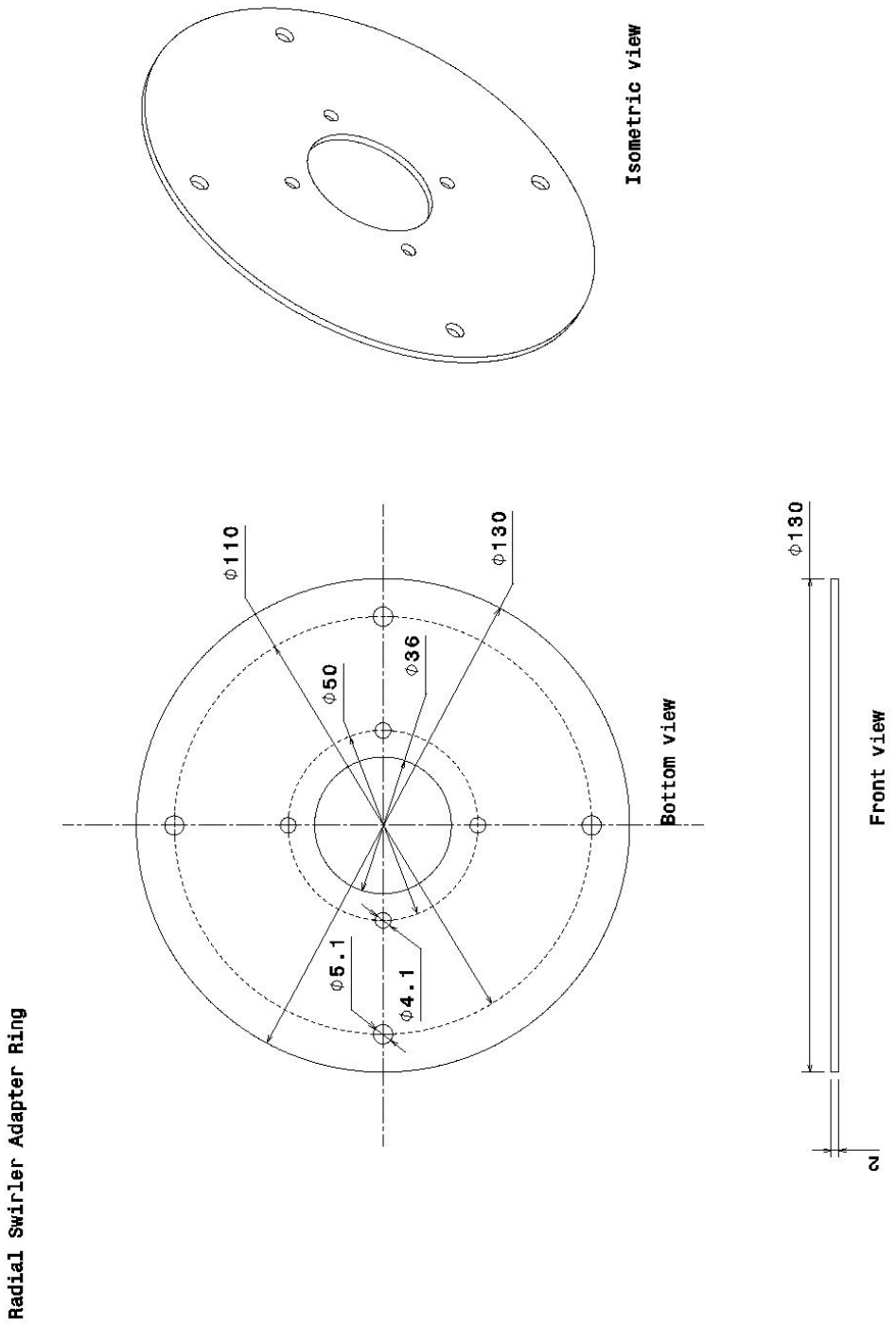
Radial Swirler Adapter Ring
Isometric view
Bottom view
Front view
ϕ110
ϕ130
ϕ50
ϕ36
ϕ5.1
ϕ4.1
ϕ130
2

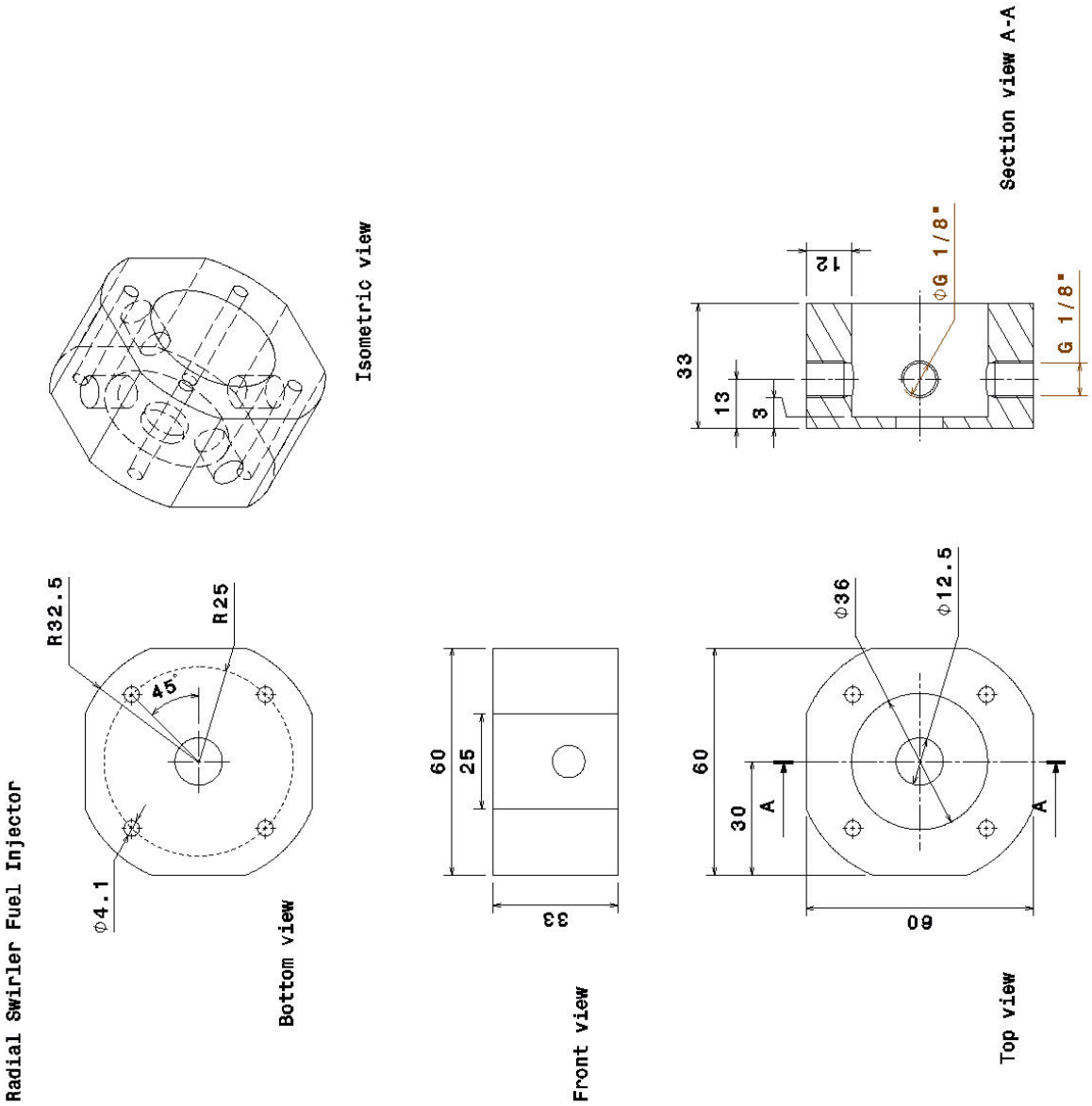
Radial Swirler Fuel Injector
R32.5
R25
45°
Φ4.1
Bottom view
Isometric view
60
25
33
Front view
Φ36
Φ12.5
60
30
A
A
60
Top view
12
Φ G 1/8"
33
13
3
G 1/8"
Section view A-A

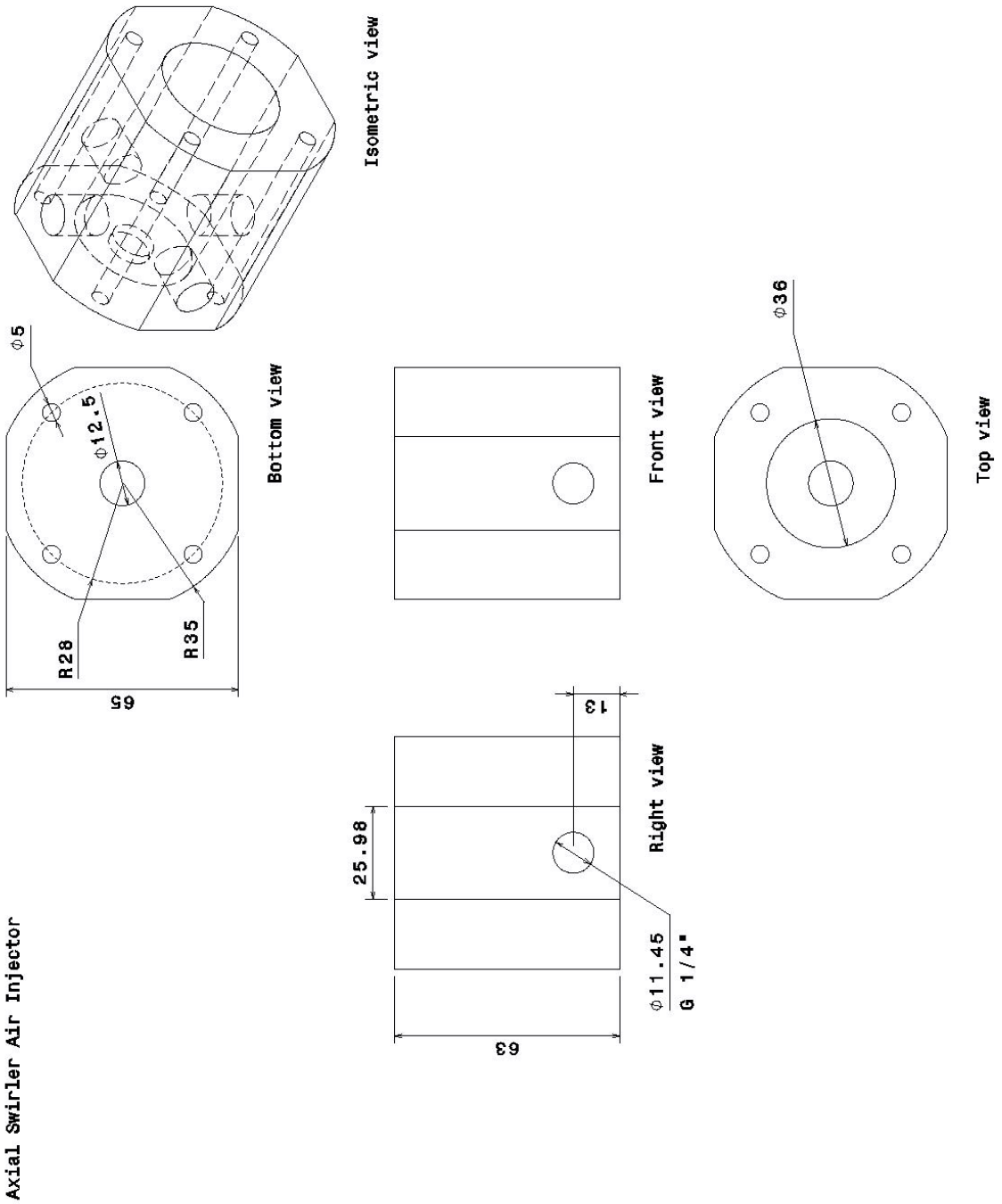
Axial Swirler Air Injector
Isometric view
Bottom view
Front view
Top view
Right view
ϕ5
ϕ12.5
R28
R35
65
ϕ36
13
25.98
63
ϕ11.45
G 1/4"

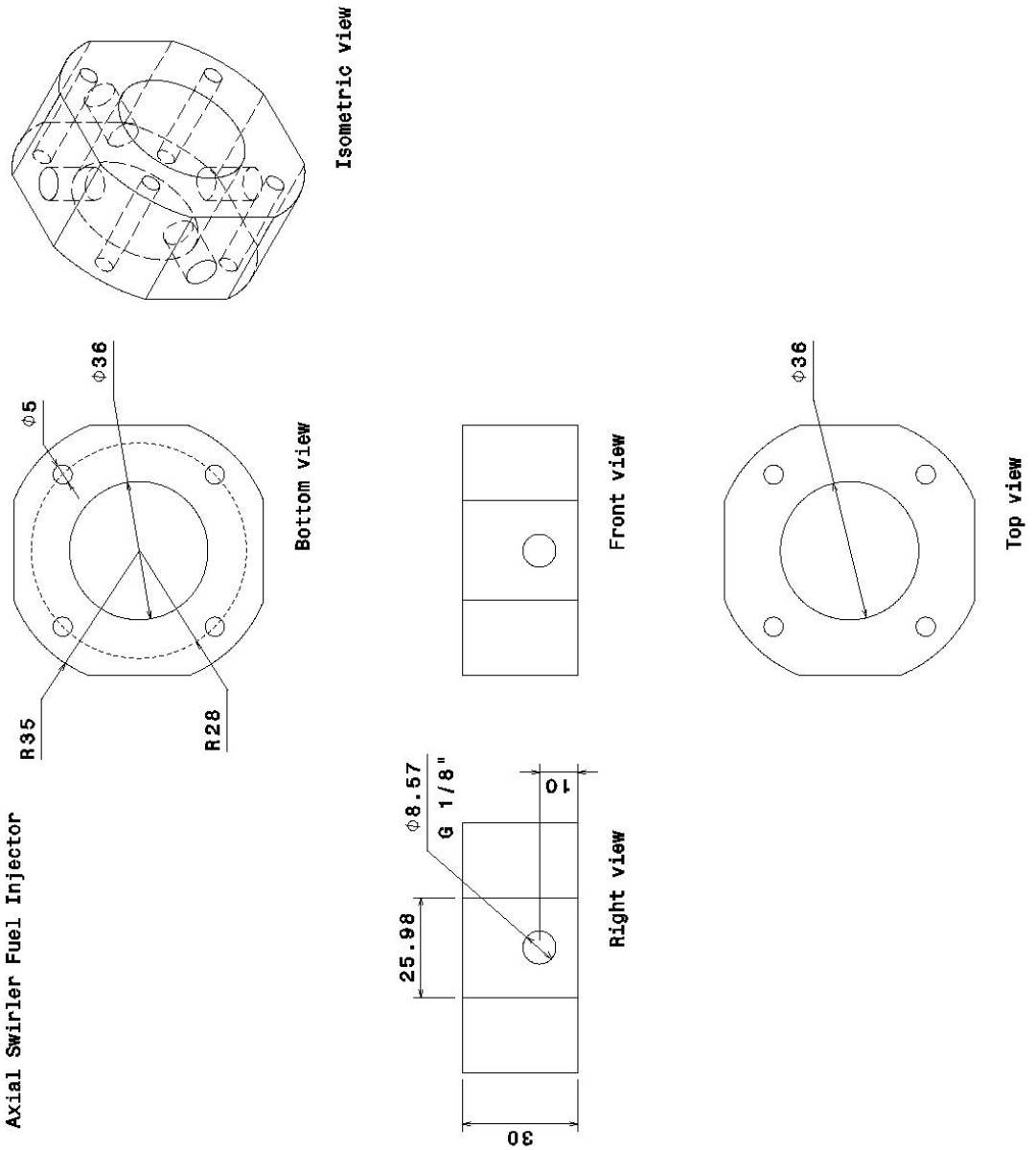
Axial Swirler Fuel Injector
Isometric view
Bottom view
Front view
Top view
Right view
Φ36
Φ5
R35
R28
Φ8.57
G 1/8"
25.98
10
30

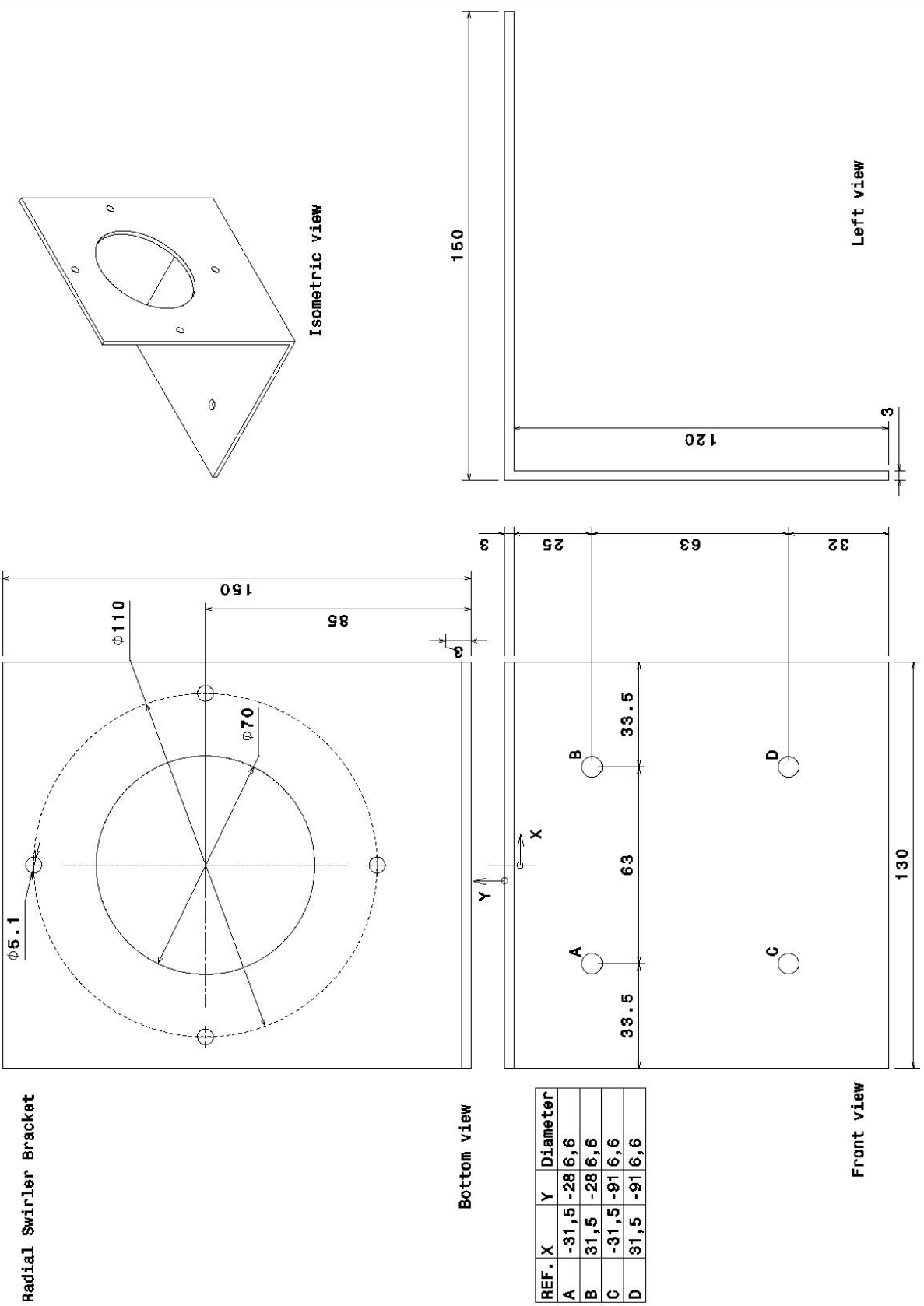

REF.	X	Y	Diameter
A	-31,5	-28	6,6
B	31,5	-28	6,6
C	-31,5	-91	6,6
D	31,5	-91	6,6

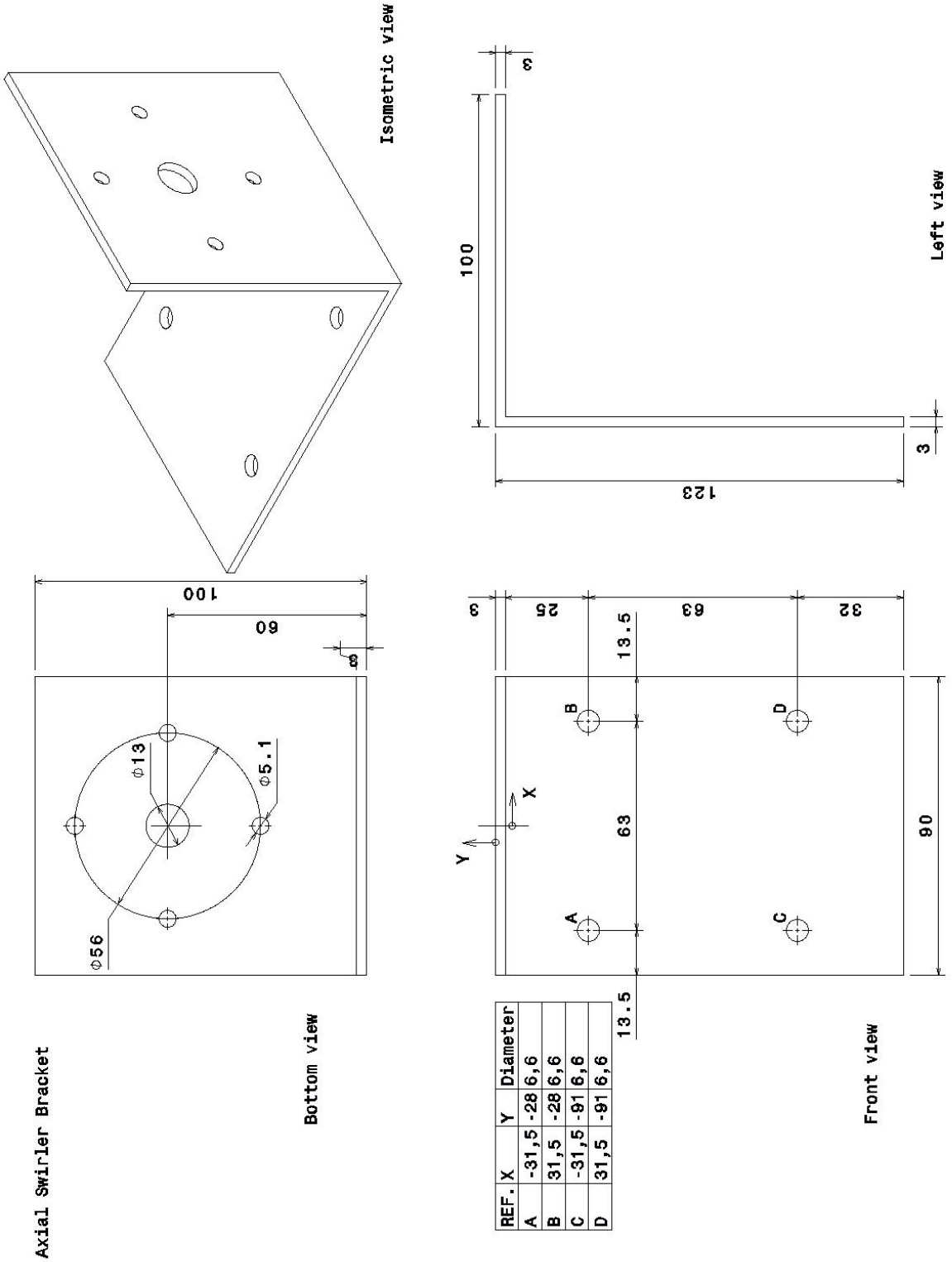
Axial Swirler Bracket
Isometric view
Bottom view
Left view
Front view
100
60
ø3
ø13
ø5.1
ø56
3
25
63
32
13.5
63
90
123
X
Y
A
B
C
D
REF. X Y Diameter
A -31,5 -28 6,6
B 31,5 -28 6,6
C -31,5 -91 6,6
D 31,5 -91 6,6

Bibliography

[1] A. Kharina and D. Rutherford. Fuel efficiency trends fornew commercial jet aircraft: 1960 to 2014. Technical report, International Council of Clean Transportation, 2015.

[2] A. Lacarelle et al. "effect of fuel/air mixing on nox emissions and stability in a gas premixed combustion system". In *45th AIAA Aerospace Sciences Meeting and Exhibit*. American Institute of Aeronautics and Astronautics, 01 2007.

[3] A. Vedantham and M. Oppenheimer. Long-term scenarios for aviation: demand and emissions of co2 and nox, 1998.

[4] Advisory Council for Aviation Research and innovation in Europe. What is acare & what does it do? `https://www.acare4europe.org/about-acare/faq`, 2020.

[5] AHEAD. Ahead project description. `http://www.ahead-euproject.eu/project-description/`, 2012.

[6] H. S. Alkabie, G. E. Andrews, and N. T. Ahmad. Lean low NOx primary zones using radial swirlers. In *Volume 3: Coal, Biomass and Alternative Fuels; Combustion and Fuels; Oil and Gas Applications; Cycle Innovations*. American Society of Mechanical Engineers, June 1988. doi: 10.1115/88-gt-245. URL `https://doi.org/10.1115/88-gt-245`.

[7] K. P. Angele and B. Muhammad-Klingmann. A simple model for the effect of peak-locking on the accuracy of boundary layer turbulence statistics in digital PIV. *Experiments in Fluids*, 38(3):341–347, February 2005. doi: 10.1007/s00348-004-0908-x. URL `https://doi.org/10.1007/s00348-004-0908-x`.

[8] J.M. Beér and N.A. Chigier. *Combustion Aerodynamics [by] J.M. Beér and N.A. Chigier*. Fuel and energy science series. Applied Science Publishers Limited, 1972. URL `https://books.google.nl/books?id=LQ3JtAEACAAJ`.

[9] D. J. Beerer and V. G. McDonell. Autoignition of hydrogen and air inside a continuous flow reactor with application to lean premixed combustion. *Journal of Engineering for Gas Turbines and Power*, 130(5), June 2008. doi: 10.1115/1.2939007. URL `https://doi.org/10.1115/1.2939007`.

[10] P.S. Beran and F.E.C. Culick. The role of non-uniqueness in the development of vortex breakdown in tubes. *Journal of Fluid Mechanics*, 242:491–527, 1992.

[11] PAUL BILLANT, JEAN-MARC CHOMAZ, and PATRICK HUERRE. Experimental study of vortex breakdown in swirling jets. *Journal of Fluid Mechanics*, 376:183–219, 1998. doi: 10.1017/S0022112098002870.

[12] A. V. Bilsky, O. A. Gobyzov, and D. M. Markovich. Evolution and recent trends of particle image velocimetry for an aerodynamic experiment (review). *Thermophysics and Aeromechanics*, 27(1):1–22, 2020. ISSN 15318699. doi: 10.1134/S0869864320010011.

[13] Joseph Brand, Sam Sampath, Frank Shum, Robert Bayt, and Jeffrey Cohen. Potential use of hydrogen in air propulsion. In *AIAA International Air and Space Symposium and Exposition: The Next 100 Years*. American Institute of Aeronautics and Astronautics, July 2003. doi: 10.2514/6.2003-2879. URL `https://doi.org/10.2514/6.2003-2879`.

[14] *EL-FLOW Select Digital Thermal Mass Flow Meters and Controllers for Gases*. Bronkhorst High-Tech B.V., Nijverheidsstraat 1a NL-7261 AK Ruurlo The Netherlands, 2021.

[15] Stephan Burmberger and Thomas Sattelmayer. Optimization of the aerodynamic flame stabilization for fuel flexible gas turbine premix burners. *Journal of Engineering for Gas Turbines and Power*, 133, 10 2011. doi: 10.1115/1.4003164.

[16] T. Cebeci. *Turbulence Models*, pages 81–94. Springer Berlin Heidelberg, Berlin, Heidelberg, 2005. ISBN 978-3-540-27717-0. doi: 10.1007/3-540-27717-X_3. URL https://doi.org/10.1007/3-540-27717-X_3.

[17] Y.A. Çengel and J.M. Cimbala. *Fluid Mechanics: Fundamentals and Applications*. College Ie Overruns. McGraw-Hill Education, 2018. ISBN 9781259921902. URL https://books.google.nl/books?id=DqFJvgAACAAJ.

[18] Cospheric. Hollow glass microspheres. https://www.cospheric.com/hollow_glass_microspheres_beads_powders.htm, 2020.

[19] Edward L. Cussler. *Diffusion Mass Transfer in Fluid Systems*. Cambridge University Press, third edition, 2009. ISBN 9780521871211.

[20] D. Dewanji. Flow characteristics in lean direct injection combustors. Master's thesis, TU Delft, 2012.

[21] P V Danckwerts. The definition and measurement of some characteristics of mixtures. *Applied Scientific Research*, 3:279–296, 1952. doi: https://doi.org/10.1007/BF03184936.

[22] Directorate-General for Mobility and Transport. Flightpath 2050, 2011.

[23] Dr. A. Bohlin and Dr. A. G. Rao and Prof. D. Roekaerts. Lecture 13: Emissions from combustion, 2018.

[24] T. D. Dudderar and P. G. Simpkins. Laser speckle photography in a fluid medium. *Nature*, 270(5632): 45–47, November 1977. doi: 10.1038/270045a0. URL https://doi.org/10.1038/270045a0.

[25] Dominik Ebi and Noel T. Clemens. Experimental investigation of upstream flame propagation during boundary layer flashback of swirl flames. *Combustion and Flame*, 168:39–52, June 2016. doi: 10.1016/j.combustflame.2016.03.027. URL https://doi.org/10.1016/j.combustflame.2016.03.027.

[26] European Commission. Reducing emissions from aviation. https://ec.europa.eu/clima/policies/transport, 2020.

[27] F. Veiga López. Numerical simulation of a lean premixed hydrogen combustor for aero engines. Master's thesis, Delft University of Technology, 2016.

[28] Science Facts. Diverging lens. https://www.sciencefacts.net/diverging-lens.html, December 2019.

[29] J. H. Faler and S. Leibovich. An experimental map of the internal structure of a vortex breakdown. *Journal of Fluid Mechanics*, 86(2):313–335, 1978. doi: 10.1017/S0022112078001159.

[30] T. F. Fric. Effects of fuel-air unmixedness on nox emissions. *Journal of Propulsion and Power*, 9, 1993.

[31] Zhenbo Fu, Yuzhen Lin, Lin Li, and Chi Zhang. Experimental and numerical studies of a lean-burn internally-staged combustor. *Chinese Journal of Aeronautics*, 27(3):488 – 496, 2014. ISSN 1000-9361. doi: https://doi.org/10.1016/j.cja.2013.12.017.

[32] Fulvio Scarano. Experimental aerodynamics. Technical report, TU Delft Aerospace Engineering Department, 2013.

[33] H H Funke, S Boerner, J Keinz, K Kusterer, D Kroniger, J Kitajima, M Kazari, and A Horikawa. Numerical and Experimental Characterization of Low NOx Micromix Combustion Principle for Industrial Hydrogen Gas Turbine Applications. *ASME Turbo Expo*, pages 1–11, 2012.

[34] Harald H W Funke and Jan Keinz. Experimental and Numerical Study on Optimizing the Dry Low NO x Micromix Hydrogen Combustion Principle for Industrial Gas Turbine Applications. *Journal of Thermal Science and Engineering Applications*, 9(June):1–10, 2017. doi: 10.1115/1.4034849.

[35] E.M. Greitzer, C.S. Tan, and M.B. Graf. *Internal Flow: Concepts and Applications*. Cambridge Engine Technology Series. Cambridge University Press, 2007. ISBN 9781139451116. URL https://books.google.nl/books?id=z7z22pmYRjIC.

[36] Fude Guo, Bin Chen, Liejin Guo, and Ximin Zhang. Investigation of turbulent mixing layer flow in a vertical water channel by particle image velocimetry (PIV). *The Canadian Journal of Chemical Engineering*, 88(6):919–928, November 2010. doi: 10.1002/cjce.20355. URL https://doi.org/10.1002/cjce.20355.

[37] Stefan Hickel. Cfd for aerospace engineers, 2018. Delft University of Technology.

[38] V Hoferichter. *Boundary Layer Flashback in Premixed Combustion Systems*. PhD thesis, Technische Universität München, 2017. URL https://mediatum.ub.tum.de/1336042.

[39] Manfred Holz, Stefan R. Heil, and Antonio Sacco. Temperature-dependent self-diffusion coefficients of water and six selected molecular liquids for calibration in accurate 1h nmrpfg measurements. *Physical Chemistry Chemical Physics*, 2:4740–4742, 2000. doi: 10.1039/B005319H.

[40] Ying Huang and Vigor Yang. Dynamics and stability of lean-premixed swirl-stabilized combustion. *Progress in Energy and Combustion Science*, 35(4):293–364, 2009. ISSN 03601285. doi: 10.1016/j.pecs.2009.01.002.

[41] ICAO. Long-term traffic forecasts. https://www.icao.int/sustainability/documents/ltf_charts-results_2018edition.pdf, 04 2018.

[42] Tjarke Jindelt, Jan Burg, Edwin Weide, and H. Hoeijmakers. Numerical investigation of vortex breakdown. In *34th AIAA Applied Aerodynamics Conference*, 06 2016. doi: 10.2514/6.2016-4174.

[43] T KITAGAWA, T NAKAHARA, K MARUYAMA, K KADO, A HAYAKAWA, and S KOBAYASHI. Turbulent burning velocity of hydrogen–air premixed propagating flames at elevated pressures. *International Journal of Hydrogen Energy*, 33(20):5842–5849, October 2008. doi: 10.1016/j.ijhydene.2008.06.013. URL https://doi.org/10.1016/j.ijhydene.2008.06.013.

[44] Arnaud Lacarelle. *Modeling, Control, and Optimization of Fuel/Air Mixing in a Lean Premixed Swirl Combustor Using Fuel Staging To Reduce Pressure Pulsations and NOx Emissions*. PhD thesis, TU Berlin, 2011.

[45] LaVision. Seeding particles. https://www.lavision.de/en/applications/fluid-mechanics/piv-system-components/seeding-particles/, 2010.

[46] LaVision. Flowmaster advanced piv / ptv systems for quantitative flow field analysis, 2018.

[47] *DaVis Software for Intelligent Imaging*. LaVision GmbH, Anna-Vandenhoeck-Ring 19 D-37081 Göttingen Germany, 2016.

[48] *LaVision Imager sCMOS CLHS*. LaVision GmbH, Anna-Vandenhoeck-Ring 19 D-37081 Göttingen Germany, August 2020.

[49] Qian Liao, Harvey A. Bootsma, Jianen Xiao, J. Val Klump, Andrew Hume, Matthew H. Long, and Peter Berg. Development of an in situ underwater particle image velocimetry (UWPIV) system. *Limnology and Oceanography: Methods*, 7(2):169–184, February 2009. doi: 10.4319/lom.2009.7.169. URL https://doi.org/10.4319/lom.2009.7.169.

[50] Tim Lieuwen, Vincent Mcdonell, Domenic Santavicca, and Thomas Sattelmayer. Burner development and operability issues associated with steady flowing syngas fired combustors. *Combustion Science and Technology - COMBUST SCI TECHNOL*, 180:1169–1192, 05 2008. doi: 10.1080/00102200801963375.

[51] M. Zajemska and A. Poskart and D. Musial. The kinetics of nitrogen oxides formation in the flame gas. Technical report, Czestochowa University of Technology, 2007.

[52] Cyrus Meher-Homji, Antonio Pelagotti, and Hans Weyermann. Gas turbines and turbocompressors for lng service. *Proceedings of the Thirty-sixth Turbomachinery Symposium*, 01 2007.

[53] F. Menter. Zonal two equation k-w turbulence models for aerodynamic flows. In *23rd Fluid Dynamics, Plasmadynamics, and Lasers Conference*. American Institute of Aeronautics and Astronautics, July 1993. doi: 10.2514/6.1993-2906. URL https://doi.org/10.2514/6.1993-2906.

[54] Florian Menter, M. Kuntz, and RB Langtry. Ten years of industrial experience with the sst turbulence model. *Heat and Mass Transfer*, 4, 01 2003.

[55] Paul Lewis Miller. *Mixing in High Schmidt Number Turbulent Jets*. PhD thesis, California Institute of Technology, 1991.

[56] D. Mira, O. Lehmkuhl, A. Both, P. Stathopoulos, T. Tanneberger, T. G. Reichel, C. O. Paschereit, M. Vázquez, and G. Houzeaux. Numerical characterization of a premixed hydrogen flame under conditions close to flashback. *Flow, Turbulence and Combustion*, 104(2-3):479–507, January 2020. doi: 10.1007/s10494-019-00106-z. URL https://doi.org/10.1007/s10494-019-00106-z.

[57] M.J. Prather and R. Sausen. Aviation and the global atmosphere, 1999.

[58] Anibal Morones Ruelas, S Ravi, D Plichta, Eric Petersen, Nicola Donohoe, Alexander Heufer, H.J. Curran, Felix Güthe, and T Wind. Laminar and turbulent flame speeds for natural gas/hydrogen blends. In *ASME Turbo Expo 2014: Turbine Technical Conference and Exposition*, 06 2014. doi: 10.1115/GT2014-26742.

[59] F. Novak and T. Sarpkaya. Turbulent vortex breakdown at high reynolds numbers. *AIAA Journal*, 38(5): 825–834, 2000. doi: 10.2514/2.1036.

[60] Kilian Oberleithner, Steffen Terhaar, Lothar Rukes, and Christian Oliver Paschereit. Why nonuniform density suppresses the precessing vortex core. *Journal of Engineering for Gas Turbines and Power*, 135 (12), September 2013. doi: 10.1115/1.4025130. URL https://doi.org/10.1115/1.4025130.

[61] E. Overmars, N. Warncke, C. Poelma, and J. Westerweel. Bias errors in piv : the pixel locking effect revisited. In *15th Int Symp on Applications of Laser Techniques to Fluid Mechanics*, 2010.

[62] T. O'Doherty and O Lucca-Negro. Vortex breakdown: A review. *Progress in Energy and Combustion Science*, 12 2001. doi: 10.1016/S0360-1285(00)00022-8.

[63] *User Manual Aerosol Generator PivPart45-M series*. PIVTEC GmbH, Stauffenbergring 21 D-37075 Göttingen Germany, 2021.

[64] Prof. V. Grewe. Climate impact of aviation co2 and non-co2 effects and examples for mitigation options, 2018.

[65] *Gas turbine combustion*, 1 1983. Purdue University, West Lafayette, IN. URL https://www.osti.gov/biblio/5027407.

[66] Ming Qian, Jun Liu, Ming-Sheng Yan, Zhong-Hua Shen, Jian Lu, Xiao-Wu Ni, Qiang Li, and Yi-Min Xuan. Investigation on utilizing laser speckle velocimetry to measure the velocities of nanoparticles in nanofluids. *Optics Express*, 14(17):7559, 2006. doi: 10.1364/oe.14.007559. URL https://doi.org/10.1364/oe.14.007559.

[67] Quantel. Evergreen specification sheet. https://www.photonicsolutions.co.uk/upfiles/EverGreen_Specs_EN_072015.pdf, 2015.

[68] Markus Raffel, Christian E. Willert, Fulvio Scarano, Christian J. Kähler, Steve T. Wereley, and Jürgen Kompenhans. *Particle Image Velocimetry*. Springer International Publishing, 2018. doi: 10.1007/978-3-319-68852-7. URL https://doi.org/10.1007/978-3-319-68852-7.

[69] S. Ravi. *MEASUREMENT OF TURBULENT FLAME SPEEDS OF HYDROGEN AND NATURAL GAS BLENDS (C1-C5 ALKANES) USING A NEWLY DEVELOPED FAN-STIRRED VESSEL*. PhD thesis, Texas A&M University, 2014.

[70] Thoralf Reichel. *Flashback Prevention in Lean-Premixed Hydrogen Combustion*. PhD thesis, TU Berlin, 2017.

[71] Thoralf G. Reichel and Christian Oliver Paschereit. Interaction mechanisms of fuel momentum with flashback limits in lean-premixed combustion of hydrogen. *International Journal of Hydrogen Energy*, 42(7):4518 – 4529, 2017. ISSN 0360-3199. doi: https://doi.org/10.1016/j.ijhydene.2016.11.018.

[72] Thoralf G. Reichel, Katharina Goeckeler, and Oliver Paschereit. Investigation of Lean Premixed Swirl-Stabilized Hydrogen Burner With Axial Air Injection Using OH-PLIF Imaging. *Journal of Engineering for Gas Turbines and Power*, 137(11), 09 2015. ISSN 0742-4795. doi: 10.1115/1.4031181. 111513.

[73] Thoralf G. Reichel, Steffen Terhaar, and Oliver Paschereit. Increasing Flashback Resistance in Lean Premixed Swirl-Stabilized Hydrogen Combustion by Axial Air Injection. *Journal of Engineering for Gas Turbines and Power*, 137(7), 07 2015. ISSN 0742-4795. doi: 10.1115/1.4029119. 071503.

[74] Thoralf G. Reichel, Steffen Terhaar, and Christian Oliver Paschereit. Flashback resistance and fuel–air mixing in lean premixed hydrogen combustion. *Journal of Propulsion and Power*, 34(3):690–701, 2018. doi: 10.2514/1.B36646.

[75] E. Roosenboom. *Image based measurement techniques for aircraft propeller flow diagnostics: Propeller slipstream investigations at high-lift conditions and thrust reverse*. PhD thesis, Delft University of Technology, 2011.

[76] Luca Sarno, Yih-Chin Tai, Armando Carravetta, Riccardo Martino, Maria Nicolina Papa, and Chih-Yu Kuo. Challenges and improvements in applying a particle image velocimetry (PIV) approach to granular flows. *Journal of Physics: Conference Series*, 1249:012011, May 2019. doi: 10.1088/1742-6596/1249/1/012011. URL https://doi.org/10.1088/1742-6596/1249/1/012011.

[77] Fulvio Scarano. Tomographic PIV: principles and practice. *Measurement Science and Technology*, 24(1): 012001, 10 2012. doi: 10.1088/0957-0233/24/1/012001.

[78] P. Schmittel, B. Günther, B. Lenze, W. Leuckel, and H. Bockhorn. Turbulent swirling flames: Experimental investigation of the flow field and formation of nitrogen oxide. *Proceedings of the Combustion Institute*, 28(1):303 – 309, 2000. ISSN 1540-7489. doi: https://doi.org/10.1016/S0082-0784(00)80224-6.

[79] Horn Jiunn Sheen, W. J. Chen, S. Y. Jeng, and T. L. Huang. Correlation of Swirl Number for a Radial-Type Swirl Generator. *Experimental Thermal and Fluid Science*, 12(4):444–451, 1996. ISSN 08941777. doi: 10.1016/0894-1777(95)00135-2.

[80] C. H. Sohn, G. S. Yang, G. N. Kim, S. Y. Moon, and C. W. Lee. Investigations of three-dimensional flow characteristics in a liquid ramjet combustor using the PIV method. *Journal of Visualization*, 5(1):59–65, March 2002. doi: 10.1007/bf03182604. URL https://doi.org/10.1007/bf03182604.

[81] Ze Sun, Haiou Ni, Hang Chen, Suzhen Li, Guimin Lu, and Jianguo Yu. Designing and optimizing a stirring system for a cold model of a lithium electrolysis cell based on CFD simulations and optical experiments. *RSC Advances*, 5(103):84503–84516, 2015. doi: 10.1039/c5ra13856f. URL https://doi.org/10.1039/c5ra13856f.

[82] S. Taamallah, Y. Dagan, N. Chakroun, S. J. Shanbhogue, K. Vogiatzaki, and A. F. Ghoniem. Helical vortex core dynamics and flame interaction in turbulent premixed swirl combustion: A combined experimental and large eddy simulation investigation. *Physics of Fluids*, 31(2):025108, February 2019. doi: 10.1063/1.5065508. URL https://doi.org/10.1063/1.5065508.

[83] Steffen Terhaar, Thoralf Reichel, Christina Schrödinger, Lothar Rukes, Kilian Oberleithner, and Christian Paschereit. Vortex breakdown types and global modes in swirling combustor flows with axial injection. *Journal of Propulsion and Power*, 31:219–229, 01 2015. doi: 10.2514/1.B35217.

[84] V. M. van Essen. Fundamental limits of no formation in fuel-rich premixed methane-air flames. Master's thesis, University of Groningen, 2007.

[85] William R. Bender. GT Handbook Lean Pre-Mixed Combustion. https://netl.doe.gov/sites/default/files/gas-turbine-handbook/3-2-1-2.pdf, 2020.

[86] Jong-Hwan Yoon and Sang-Joon Lee. Stereoscopic PIV measurements of flow behind an isolated low-speed axial-fan. *Experimental Thermal and Fluid Science*, 28(8):791–802, October 2004. doi: 10.1016/j.expthermflusci.2003.10.004. URL https://doi.org/10.1016/j.expthermflusci.2003.10.004.

[87] Y.B. Zeldovich. The oxidation of nitrogen in combustion and explosions. *Acta Physicochimica URSS*, 11: 577–628, 1946.

[88] Laith Zori. What is the best value of maximum aspect ratio in ansys fluent?, 01 2015.